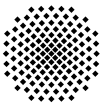

University of Stuttgart
Germany

Large-Area Plasmonics and Sensors

Fabrication of plasmonic nanostructures by laser interference lithography and femtosecond direct laser writing

Von der Fakultät Mathematik und Physik der Universität Stuttgart
zur Erlangung der Würde eines Doktors der
Naturwissenschaften (Dr. rer. nat.) genehmigte Abhandlung

vorgelegt von

Shahin Bagheri
aus Kermanshah, Iran

Hauptberichter: Prof. Dr. Harald Giessen
Mitberichter: Prof. Dr. Clemens Bechinger
Vorsitzender: Prof. Dr. Hans Peter Büchler

Tag der mündlichen Prüfung: 25.04.2017

4. Physikalisches Institut der Universität Stuttgart

April 2017

DECLARATION

I hereby certify that this dissertation is entirely my own work except where otherwise indicated. Passages and ideas from other sources have been clearly indicated.

Stuttgart, April 2017
Shahin Bagheri

ABSTRACT

The interaction of light with various types of metallic nanostructures reveals unique optical properties originating from the excitation of the localized surface plasmon resonances, which can be used for a wide range of spectroscopic and sensing applications. While, precisely defined and tailored nanostructures are essential building blocks for realizing such schemes, the commonly used electron-beam lithography is a cost-intensive and time-consuming method to create well-defined nanostructures over small areas. However, a low-cost and high-throughput fabrication method over large areas is crucial to advance plasmonic devices towards life science and technological applications.

Building on these concepts, this thesis demonstrates the use of versatile large-area fabrication methods such Laser Interference Lithography (LIL) and Direct Laser Writing (DLW) for the fabrication of different plasmonic devices such as perfect absorber sensors and surface enhanced infrared absorption substrates. Both lithographic techniques allow for fast and homogeneous preparation of various nanoantenna geometries.

Utilizing different plasmonic geometries, this work pursues laser interference lithography for large-area fabrication of plasmonic perfect absorber chemical sensors to reliably detect very small amounts of hydrogen. Furthermore, both laser interference lithography and direct laser writing allow for the preparation of large-area plasmonics nanoantenna arrays for surface-enhanced infrared spectroscopy, enabling the detection of small amounts of vibrationally active molecules.

Additionally, both techniques combined with subsequent etching processes are employed for nanostructuring of so-called alternative plasmonic materials namely titanium nitride. Titanium nitride, known as a refractory plasmonic material, provides plasmonic properties comparable with gold and can sustain at high temperatures as investigated in the thesis.

ZUSAMMENFASSUNG

Die Wechselwirkung von Licht mit verschiedenen metallischen Nanostrukturen zeigt einzigartige optische Eigenschaften, welche auf der Anregung lokalisierter Oberflächenplasmonen beruhen. Diese Eigenschaften können in vielen Anwendungsbereichen in der Spektroskopie und der Sensortechnologie eingesetzt werden. Während präzise definierte und mit hoher Genauigkeit hergestellte Nanostrukturen für die Realisierung solcher Konzepte entscheidend sind, ist die häufig dafür eingesetzte Elektronenstrahllitographie eine sehr zeit- und kostenintensive Methode zur Herstellung solcher Nanostrukturen auf kleinen Flächen. Es ist jedoch eine kostengünstige Methode, die einen hohen Durchsatz über große Flächen bietet notwendig, um die Anwendung plasmonischer Nanostrukturen in den Lebenswissenschaften und der Technologie voranzutreiben.
Auf diesen Konzepten aufbauend werden in dieser Thesis zwei Herstellungsmethoden, die Laserinterferenzlithographie (LIL) und das Direct Laser Writing (DLW), vorgestellt. Diese Methoden bieten die Möglichkeit zur großflächigen Herstellung von plasmonischen Strukturen wie den sogenannten Perfekten Absorbern und Substraten für die Surface Enhanced Infrared Absorption (SEIRA). Beide Methoden erlauben eine schnelle und homogene Herstellung von komplexen Geometrien auf der Nanometerskala. Mit Hilfe verschiedener Geometrien zeigt diese Arbeit die Anwendung von Laserinterferenzlithographie zur Herstellung chemischer Sensoren für die Detektion sehr kleiner Wasserstoffgasvolumina mittels plasmonischer perfekter Absorber.

Weiterhin wurden sowohl mittels Laserinterferenzlithographie als auch DLW großflächige Raster aus plasmonischen Nanoantennen für die oberflächenverstärkte Infrarotspektroskopie hergestellt, welche die Detektion kleiner Mengen vibrationsaktiver Moleküle ermöglichen.
Weiterhin werden beide Techniken in Kombination mit Ätzprozessen für die Nanostrukturierung von sogenannten alternativen plasmonischen Materialien, insbesondere Titannitrid (TiN) eingesetzt. Titannitrid, welches auch als feuerfestes plasmonisches Material bekannt ist, bietet ähnliche plasmonische Eigenschaften wie Gold und behält diese auch bei hohen Temperaturen, wie in dieser Arbeit untersucht wird, bei.

PUBLICATIONS

Parts of this thesis have already been published in the scientific journals:

1. S. Bagheri, H. Giessen, and F. Neubrech
   "**Large-Area Antenna-Assisted SEIRA Substrates by Laser Interference Lithography**"
   Advanced Optical Materials 2(11), 1050-1056 (2014).
   The article has been chosen as **VIP article** in the volume 2, issue 11 of *Advanced Optical Materials*. Additionally this article appeared on the **frontispiece of the November 2014 issue** of *Advanced Optical Materials*.

2. S. Bagheri, K. Weber, T. Gissibl, T. Weiss, F. Neubrech, and H. Giessen
   "**Fabrication of Square-Centimeter Plasmonic Nanoantenna Arrays by Femtosecond Direct Laser Writing Lithography: Effects of Collective Excitations on SEIRA Enhancement**"
   ACS Photonics 2(6), 779-786 (2015).

3. S. Bagheri, C. M. Zgrabik, T. Gissibl, A. Tittl, F. Sterl, R. Walter, S. De Zuani, A. Berrier, T. Stauden, G. Richter, E. L. Hu, and H. Giessen
   "**Large-Area Fabrication of TiN Nanoantenna Arrays for Refractory Plasmonics in the Mid-Infrared by Femtosecond Direct Laser Writing and Interference Lithography**"
   Optical Materials Express 5(11), 2625-2633 (2015).
   This paper has been highlighted in the OSA **Spotlight on Optics**. (November 2015). Additionally, this paper was one of the **most downloaded articles** in Optical Materials Express in November 2015, January 2016 and the second most downloaded article in December 2015.

4. S. Bagheri, N. Strohfeldt, F. Sterl, A. Berrier, A. Tittl, and H. Giessen
"**Large-Area Low-Cost Plasmonic Perfect Absorber Chemical Sensor Fabricated by Laser Interference Lithography**"
ACS Sensors 1(9), 1148–1154 (2016).
This article appeared on the **cover of the September 2016 issue** of *ASC Sensors*.

5. S. Bagheri, N. Strohfeldt, A. Berrier, G. Richter, and H. Giessen
"**Niobium as Alternative Material for Refractory Plasmonics and Hydrogen Sensing**"
In preparation.

Other scientific contributions which are not part of this thesis:

6. M. Hentschel, T. Weiss, S. Bagheri, and H. Giessen
"**Babinet to the Half: Coupling of Solid and Inverse Plasmonic Structures**"
Nano Letters 13(9), 4428–4433 (2013).

7. L. Gui, S. Bagheri, N. Strohfeldt, M. Hentschel, C. M. Zgrabik, B. Metzger, H. Linnenbank, E. L. Hu, and H. Giessen
"**Nonlinear Refractory Plasmonics with TiN Nanoantennas**"
Nano Letters 16(9), 5708–5713 (2016).

Parts of this thesis have been also presented at the international conferences:

Talks:

8. S. Bagheri, H. Giessen, and F. Neubrech
"**Large-Area Low-Cost Resonant Nano-Antenna Enhanced SEIRA Substrate Using Interference Lithography**"
Spring Meeting of the German Physical Society (DPG), Dresden, Germany (2014).

9. S. Bagheri, H. Giessen, and F. Neubrech
"**Large-area Low-cost Substrates for Antenna-assisted Surface enhanced Infrared Spectroscopy by Interference Lithography**"
5^{th} *International Conference on Metamaterials, Photonic Crystals and Plasmonics*, Singapore, (2014)

10. F. Neubrech, S. Bagheri, K. Weber, T. Gissibl, and H. Giessen
"**Fabrication of Plasmonic Nanoantennas by Femtosecond Direct Laser Writing Lithography - Effects of Near Field Coupling on SEIRA Enhancement**"
Spring Meeting of the German Physical Society (DPG), Berlin, Germany (2015).

11. S. Bagheri, N. Strohfeldt, A. Tittl, and H. Giessen
"**Large-Area Spectrally Selective Plasmonic Perfect Absorber Sensor Fabricated by Laser Interference Lithography**"
Spring Meeting of the German Physical Society (DPG), Berlin, Germany (2015).

12. H. Giessen, F. Neubrech, S. Bagheri, and K. Weber
"**Fabrication of Plasmonic Nanoantennas by Femtosecond Direct Laser Writing Lithography- Effects of Near Field Coupling on SEIRA Enhancement**"
Radio Science Conference (URSI AT-RASC), 1^{st} URSI Atlantic, Gran Canaria, Spain (2015).

13. S. Bagheri, N. Strohfeldt, A. Tittl, and H. Giessen
"**Large-Area Low-Cost Plasmonic Perfect Absorber Sensor Fabricated by Laser Interference Lithography**"
SPIE Optics and Photonics, San Diego, USA (2015), **Invited talk**.

14. S. Bagheri, C. M. Zgrabik, T. Gissibl, A. Tittl, F. Sterl, R. Walter, S. De Zuani, A. Berrier, T. Stauden, G. Richter, E. L. Hu, and H. Giessen
"**Refractory Plasmonics**"
Kompetenznetz Funktionelle Nanostrukturen (KFN), Research Network Functional Nanostructures, Bad Herrenalb, Germany (2015).

15. S. Bagheri, C. M. Zgrabik, T. Gissibl, A. Tittl, F. Sterl, R. Walter, S. De Zuani, A. Berrier, T. Stauden, G. Richter, E. L. Hu, and H. Giessen
"**Large-Area Fabrication of TiN Nanoantenna Arrays for Refractory Plasmonics in the Mid-Infrared**"
Spring Meeting of the German Physical Society(DPG), Regensburg, Germany (2016).

16. S. Bagheri, C. M. Zgrabik, T. Gissibl, A. Tittl, F. Sterl, R. Walter, S. De Zuani, A. Berrier, T. Stauden, G. Richter, E. L. Hu, and H. Giessen
"**Large-Area Fabrication of TiN Nanoantenna Arrays for Refractory Plasmonics in the Mid-Infrared**"
SPIE Photonics West, OPTO, the Optoelectronics and Photonics Conference, San Francisco, USA (2016).

Posters:

17. F. Neubrech, S. Bagheri, K. Weber, T. Gissibl, and H. Giessen
"**Fabrication of Plasmonic Nanoantennas by Femtosecond Direct Laser Writing Lithography - Effects of Plasmonic Coupling on SEIRA Enhancement**"
5^{th} *International Topical Meeting on Nanophotonics and Metamaterials*, Seefeld (Tirol), Austria (2015).

18. S. Bagheri, K. Weber, T. Gissibl, T. Weiss, F. Neubrech, and H. Giessen
"**Fabrication of Plasmonic Nanoantennas by Femtosecond Direct Laser Writing Lithography for Surface-Enhanced Infrared Absorption**"
META'15, the 6th International Conference on Metamaterials, Photonic Crystals and Plasmonics, New York, USA (2015).

19. S. Bagheri, C. M. Zgrabik, T. Gissibl, A. Tittl, F. Sterl, R. Walter, S. De Zuani, A. Berrier, T. Stauden, G. Richter, E. L. Hu, and H. Giessen
"**Large-Area Fabrication of TiN Nanoantenna Arrays for refractory Plasmonics in the Mid-Infrared**"
Kompetenznetz Funktionelle Nanostrukturen (KFN), Research Network Functional Nanostructure, Bad Herrenalb, Germany (2015).

20. S. Bagheri, K. Weber, T. Gissibl, T. Weiss, F. Neubrech, and H. Giessen
"**Fabrication of cm² Plasmonic Nanoantenna Arrays by Femtosecond Two-Photon Lithography**"
WE-Heraeus-Seminar "Merging Micro- and Nano-Optics: 3D Printing for Advanced and Functional Optics, Bad Honnef, Germany (2017).

Scientific contributions presented at the international conferences which are not part of this thesis:

21. M. Hentschel, T. Weiss, S. Bagheri, and H. Giessen
"**Babinet to the Half: Coupling of Solid and Inverse Plasmonic Structures**"
Spring Meeting of the German Physical Society (DPG), Berlin, Germany (2015).

22. L. Gui, B. Metzger, S. Bagheri, C. M. Zgrabik, N. Strohfeldt, E. L. Hu, and H. Giessen
"**Nonlinear Refractory Plasmonics with TiN Nanoantennas**"
Topical Meeting on Nonlinear Plasmonics and its Applications, Rome, Italy (2016).

23. L. Gui, H. Linnenbank, S. Bagheri, N. Strohfeldt, C. Zgrabik, B. Metzger, M. Hentschel, E. Hu, and H. Giessen
"**Nonlinear Refractory Plasmonics with TiN Nanoantennas**"
CLEO, San Jose, California, USA (2016).

Also, the main results of the thesis have been presented with the title of Large-Area Plasmonics and Sensors in the group of **Prof. Nader Engheta, SEAS-University of Pennsylvania** and **Prof. Evelyn Hu, University of Harvard**.

CONTENTS

TITLE i

DECLARATION iii

ABSTRACT v

ZUSAMMENFASSUNG vii

PUBLICATIONS ix

1 INTRODUCTION 1

2 PLASMONIC THEORY FOR SENSING 5

2.1 Plasmonics for Nanooptics 5

2.2 The Experimental Revolutions 7

2.3 Plasmonic surfaces for sensing and Spectroscopy 8

2.3.1 Plasmonic Nanoantenna as a Platform for Nanophotonics 8

2.3.2 Localized Plasmons and Optical Antennas 10

2.3.3 Surface Plasmon Polaritons Versus Localized Surface Plasmon Polaritons 10

2.3.4 Metallic Nanoparticle As a Simple Optical Nanoantenna 13

2.3.5 Influence of Particle Shape in Plasmon Response 16

2.3.6 Field Enhancement by Plasmon Coupling 19

2.4 Practical application of plasmonics 22

2.4.1 Plasmonics Perfect Absorbers 22

2.4.2 Surface-Enhanced Infrared Spectroscopy . 24
2.4.3 Refractory Plasmonics 27
2.5 Nanofabrication Techniques for Plasmonics Applications 31
2.5.1 Lithography: Evolution and Resolution . . 31
2.5.2 Electron-Beam Lithography 33
2.6 Alternative Lithographic Techniques 35
2.6.1 Laser Interference Lithography 35
2.6.2 Direct Laser Writing 36

3 LARGE-AREA PLASMONIC PERFECT ABSORBER CHEMICAL SENSOR 39
3.1 Basic Principles 41
3.2 Palladium-Based Plasmonics Perfect Absorbers . 44
3.3 Polarization Independent Perfect Absorbers . . . 46
3.4 Hydrogen Sensing 50

4 LARGE-AREA ANTENNA-ASSISTED SEIRA SUBSTRATES BY LIL 59
4.1 Basic Principles 61
4.2 Laser Interference Lithography 64
4.3 Measurement Over Large-Area 69
4.4 Tunability of the Plasmonic Response 71
4.5 Antenna-Assisted SEIRA 73
4.6 In-situ Monitoring of Polymer UV Degradation . 80

5 LARGE-AREA ANTENNA-ASSISTED SEIRA SUBSTRATES BY DLW 83
5.1 Basic Principles 85
5.2 Direct Laser Writing Lithography 86
5.3 Plasmonic Response of Large-Area Antenna Arrays 90
5.3.1 Large-Area Fabrication 90

5.3.2 Measurement Over Large-Area 92
5.3.3 Controlling the Feature Size 94
5.4 Antenna-Assisted SEIRA 95
5.5 Plasmonic Coupling Excitation 98
5.6 Nanoantennas on Single Crystalline Gold Plates . 104

6 REFRACTORY PLASMONICS 109
6.1 Basic Principles 110
6.2 TiN Nanoantennas Fabrication 112
6.3 Optical Properties of TiN Nanoantennas 114
6.4 Thermal Stability of TiN Nanoantennas 117
6.5 Large-Area Fabrication 121

7 CONCLUSION 123

ACRONYMS 127

BIBLIOGRAPHY 131

ACKNOWLEDGMENTS 163

CURRICULUM VITAE 167

1

INTRODUCTION

The interaction of light with metals, known as plasmonics host of potential applications in nano-optics and nano-photonics. A major driving force in surface plasmon application is manipulation and confinement of light at the sub-wavelength or nano-scale beyond the diffraction limit of light, getting more interesting when it goes to the nano-particle regime, where optical properties can be tailored and engineered.

Many plasmonic devices consist metallic nanostructures that always interact with each other and the external light field. To practically fulfill the feasible applications of plasmonics, such nanostructures need to be designed and fabricated precisely to enable the best performance for plasmonic devices. Electron beam lithography [1] is the most common used method enabling well-defined and precise nanostructures. Such nanostructures, however, are achievable only over small areas ($100 \times 100\ \mu m^2$) and suffer from high-cost and time consuming, which limits plasmonics only for scientific applications.

To bring nano-featured surfaces in a high-throughput manner for technological and life science applications, a large-area and low-cost fabrication method with good control on geometrical parameters is required. Ideally, one would like to have low-cost and cm^2 sized chips, which provide plasmonic resonance over the whole area and can be simply put into standard infrared spectrometers, serving as smart substrates for the detection and identification of biological or chemical substances.

In recent years, the ability of many nanofabrication techniques to achieve plasmonics nanostructures have been proved. For example self-assembly [2], chemical synthesis [3], metal nanoparticle deposition [4, 5] metal island films [6, 7] and also metal antennas prepared by bottom-up approaches, such as nanosphere lithography [8–10], enable such large-area fabrication, but suffer from inhomogeneity on large scales. On the other hand, colloidal hole mask lithography [11, 12] and colloidal etching lithography [13] have been introduced as an approach to fabricate tailored nanostructures, However, due to intrinsic limitations of the method, only randomly distributed antennas can be realized. Other methods, like direct nanocutting [14], nanoimprint and nanostencil lithography techniques [15, 16], have their own limitation such as a slow fabrication process of the mask.
In contrast to these methods, laser interference lithography (LIL) [17, 18] and direct laser writing (DLW) [19, 20] share many of the advantages of other fabrication techniques, while alleviating a majority of concerns such as cost and complexity. In this thesis, we demonstrate for the first time the ability of LIL and DLW for the preparation of large-area and low-cost plasmonic nanostructures and confirm their applicability for fabrication of plasmonics devices through manufacturing of surface enhanced infrared absorption (SEIRA) substrates and plasmonic perfect absorbers.
As a theoretical primer, chapter 2 presents some of the fundamental scientific concepts for describing and understanding the behavior of functional plasmonic nanostructures. This includes a general discussion of the electrodynamics of metal/dielectric interfaces and metal nanoparticles as well as an overview of the systems used in the presented thesis.
Chapter 3 gives a brief overview of the simple and versatile de-

sign of palladium based plasmonics perfect absorber for hydrogen sensing. Laser interference lithography is utilized to fabricate large-area palladium wire and square arrays, to realize plasmonic perfect absorber sensors in the visible- and near-infrared wavelength ranges.

Chapter 4 focuses on the fabrication and characterization of large-area plasmonic antenna arrays with excellent homogeneity, featuring high-quality plasmons in the near- and mid-infrared spectral range by employing laser interference lithography. The resonances are easily tunable and thus ideally suited for antenna-assisted surface-enhanced infrared absorption spectroscopy as demonstrated by enhancing the infrared vibrational signals of a monolayer octadecanethiol and by monitoring the ultraviolet degradation of the polymer XARP with an increased sensitivity via vibrational signal decay without modifying the degradation process itself.

Chapter 5 begins a detailed description of direct laser writing combined with argon ion beam etching to fabricate homogeneous large-area nanoantenna arrays providing adjustable plasmon resonances in the mid-infrared spectral range. This chapter also is comprised of comprehensive studies, discusses the use of these nanoantennas for surface enhanced infrared absorption, as demonstrated by enhancing vibrational signals of CBP molecules evaporated on antenna arrays with different spacings between the elements.

Chapter 6 shows the ability of both lithographic tools for large-area fabrication of alternative plasmonics material namely titanium nitride featuring high-quality plasmon resonances in the near- and mid-infrared spectral range. Thermal stability of such nanostructures is demonstrated accordingly.

In chapter 7, the main results of the thesis are summarized, and

a short outlook on how future large-area plasmonic devices can be built on the presented concepts is given.

2

PLASMONIC THEORY FOR SENSING

This chapter is an introduction to the surface plasmon theory and outlines the theoretical treatment of plasmonic systems for sensing applications. Building on this, surface plasmon and localized surface plasmon resonances are discussed. Then the key properties of surface plasmons for nanooptics are addressed in general terms, with special emphasis on the plasmonic nanoantennas.
Following the brief description of the working principle of localized surface plasmons of metallic particles, field enhancement by plasmon coupling for vibrational spectroscopy is introduced and the concept of plasmonic perfect absorber, surface enhanced infrared absorption (SEIRA), and refractory plasmonic are discussed. Finally, a general explanation of some nanofabrication techniques such as electron beam lithography (EBL), laser interference lithography (LIL) and direct laser writing lithography (DLW) are presented.
The basic principle of the plasmonic systems has been described in different textbooks. This introductory chapter follows the line of argument in Ref. [21] with some parts adapted from Ref. [22].

2.1 PLASMONICS FOR NANOOPTICS

Recently, a great attention on the new fields of research has been directed to nanophotonics. One of the major aims of nanophotonics is to achieve optical instruments with the ability to focus

the light much tighter than the diffraction limit (about half a wavelength) to strongly fulfill sub-wavelength light localization. This approach can provide many efficient tools for characterization of surfaces as well as biological objects.

The future of nanophotonic technologies strongly will be featured by plasmonic devices. Plasmonics is a knowledge that offers metallic nanostructures to authorize light at the nanoscale regime [23] and define the behavior of light at the nanometer scale when the size of elements in the optical components are significantly smaller than the wavelength. In fact, Plasmonics is able to resolve the mismatch between the wavelength-scale optical devices and the small components of integrated electronic circuits and consequently, merges photonics and electronics in nanoscale dimensions [24]. Plasmonic circuits enable both optical signals and electric currents through the same thin metal circuitry and therefore, create a new opportunity for the combination of the photonics and electronics advantages at the same time.

The required material properties to apply metamaterials to novel optical functionalities, however, involve unusual values of the permittivity and permeability which cannot be found in nature. Nevertheless, the advent of metamaterials enables tailored components with nanometer precision to address this concern for specific applications [25].

The majority of plasmonic devices including compact sources, detectors, and sensors rely on surface plasmon polaritons (SPPs), the special type of electromagnetic wave that propagates through the surface of metals. This feature, however, suffers scattering losses and consequently an attenuation of the SPPs, which restricts the range of SPPs applications. In certain cases, where the isotropic and non-magnetic elements are the only necessary

parameters for plasmonics desires, dielectric media allows for low-loss and broadband processes. Such attractive features have been pursued formerly [26–28]. Where plasmonics is used in a metal-dielectric system the magnetic-field component of two-dimensional SPPs lies parallel to the surface and perpendicular to the propagating direction. Therefore, modifications in the magnetic permeability of the dielectric can be avoided if no spatial transformation occurs along the direction of the magnetic field. These electromagnetic waves propagate along metal-dielectric interfaces and can be guided by metallic nanostructures beyond the diffraction limit [29]. This remarkable potential has unique prospects for the design of highly integrated photonic signal processing systems, nano-resolution optical imaging techniques, and sensors [29].

2.2 THE EXPERIMENTAL REVOLUTIONS

At the end of the 1960s and beginning of 1970s, the use of laser sources and photoresist layers had a great influence in the development of the theoretical and experimental tools used for the study of grating anomalies. Manufacturing of different types of holographic gratings with sub-micron periodicity by light and photosensitive material enabled accurate tools for technical and industrial application. Nowadays, technology develops the wide range of various lithographic techniques and thus many sub-micrometer nanostructures can be fabricated for plasmonics applications. The progress in nanofabrication techniques has opened up the possibility to fabricate well designed metallic nanostructures in macroscopic size arrays with oriented geometry and compact nanostructures on the substrate [30] compared to distributed nanostructures in the solutions [31, 32].

2.3 PLASMONIC SURFACES FOR SENSING AND SPECTROSCOPY

Functional and active surfaces play an important role in driving the plasmonic devices. In this section, nanoantenna metamaterial geometries are addressed as the platform for plasmonic schemes. In this section, to understand the key factors leading the optical response in finite metallic nanostructures, a review on the basic principle of localized surface plasmons (LSPs) based on optical antennas is described. Then both general terms of surface plasmon polariton and localized surface plasmon polariton are detailed. After that, the optical response of metallic sphere as a simple nanoantenna is discussed. Different aspects of optical nanoantenna such as influences of the particle shape in plasmon response, tuning of the spectral response, and the magnitude of the field enhancement in simple terms are also described in details. Furthermore, based on field enhancement by plasmonic coupling of nanoantenna the role of weak and strong coupling regimes of molecular excitons and plasmonic modes of the metamaterial on the optical properties is discussed. Optical antennas assisting in field-enhanced spectroscopy are also detailed in the context of surface-enhanced infrared absorption (SEIRA). A brief discussion of the fabrication processes will be presented in the next section.

2.3.1 *Plasmonic Nanoantenna as a Platform for Nanophotonics*

Metamaterials are manufactured nanostructures with a promising electromagnetic response, which can be tuned by the material properties and geometrical design of the nanostructures [33, 34]. The metallic nanostructures are typically accompanied by the dielectric medium and support surface plasmon excita-

tions associated with the free-electron motion in both interfaces of the metal and the dielectric. The plasmonic metamaterials are found in several combinations of metallic nanostructures, for example, nanoantenna arrays. They enable a flexible scheme of optical properties by adjusting the optical response of individual antennas and their electromagnetic interaction. The unique physical properties of metamaterials such as negative permeability and negative refractive index might be used to design new nanophotonic tools such as high-resolution lenses and imaging devices [35–41]. An important advantage of metamaterials in active nanophotonic applications is the possibility to design and tune the dispersion of plasmonic modes which can be done electrically, mechanically or optically [42–46].

The nanoantenna metamaterials typically consist of aligned nanoantennas oriented parallel on a substrate. They are classically fabricated by the combination of evaporation and lift-off on a substrate with well-defined geometrical parameters. The optical response of the metamaterial is influenced by the parameters of the nanoantenna such as aspect ratio, length, and separation in the array. In contrast to suspended nanorods in solutions, the nanoantennas have typically a much higher aspect ratio and are placed in a regular arrangement.

The optical properties of such nanoantenna arrays can be described by effective permittivity parameters. Comprehensive studies of the optical properties of this kind of metamaterials have shown that their strong anisotropic optical behavior can be beneficial for spectroscopic, sensing, as well as near-field optical imaging applications [47–51]. The most important feather of nanoantenna metamaterials is the possibility of wide range tuning of the geometrical parameters of the structure to control the electromagnetic interaction between the antennas. This can be

done, for example, by changing the antenna spacing and, which is crucial for determining the transmission (T), reflection (R), and associated linear and nonlinear properties. They also exhibit unique optical properties such as active optical functionalities, high-resolution imaging capabilities, high sensitivity to refractive index variations, and enhanced nonlinear properties [52–54].

2.3.2 *Localized Plasmons and Optical Antennas*

The oscillation of the surface charge density in metallic nanoparticles, commonly named localized surface plasmons LSPs, is a result of the collective oscillation of the conduction electrons under the constraints imposed by the physical boundaries of the nanostructures geometry [21].
Localized surface plasmons (LSPs) determine the optical properties of metallic nanoparticles. In contrast to the surface modes propagating along metal-dielectric interfaces, LSPs are stationary oscillations of the surface charge density at optical frequencies along the boundaries of a metallic particle [21]. LSPs are important elements to generate subwavelength-enhanced electromagnetic fields that can develop, control, and enhance physical processes such as vibrational spectroscopy [55], energy transfer [56], molecular sensing [57], photoemission [58], nanoscale microscopy [59].

2.3.3 *Surface Plasmon Polaritons Versus Localized Surface Plasmon Polaritons*

Surface plasmon polaritons (SPPs) are surface charge density waves that propagate at a metal-dielectric interface. Typical disper-

sion curve of SPPs is shown as a dashed blue line in Figure 2.1a. Since energy and momentum are not conserved simultaneously, light (black-solid line) cannot be coupled directly to plasmon excitations of a flat and semi-infinite metal surface. The intrinsic limitation of SPPs excitation causes the surface plasmon were predicted in the context of the interaction of charges with thin metallic films [60]. The excitation of plasmons by fast electrons is possible due to the momentum transfer $k \approx \omega/v$, from those electrons that involves their velocity v and ω the energy of the electrons. Since SPPs can also be excited by light, there are several possibilities to provide the additional momentum; therefore the surface plasmon can be coupled to incident light. An option would be modifying the planar metal surface using the gratings that provide so-called lattice momentum to warranty momentum conservation. This concept has been experimentally verified in order to authorize plasmons in surfaces and also to detect SPPs via scattering them from an interface [61].

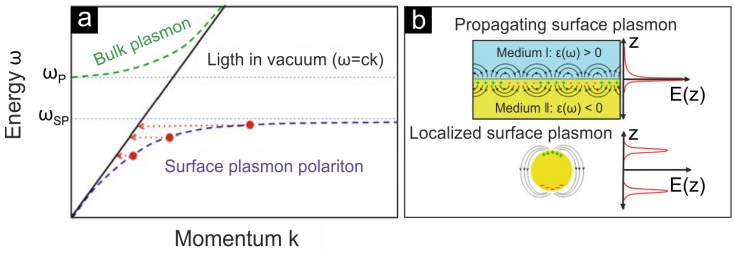

Figure 2.1: (a) Dispersion curve of the bulk plasmon (green dashed line) and SPP (blue dashed line). The curve of light in vacuum is displayed as a solid black line. Red dots and red-dashed lines denote schematically a certain momentum provision that allows for effective coupling to light. (b) Top: schematics of the surface charge density of a propagating surface plasmon polariton. Bottom: schematics of the surface charge density of an LSP. Adapted from Ref. [21].

In contrast to the propagating SPPs in a semi-infinitive surface confined geometrical boundaries in a metallic nanoparticle can support localized oscillation of the surface charge density. This localized excitation is schematically shown in Figure 2.1b).
The optical response of the LSP in a metallic particle can be described by particle polarizability α of the incoming electric field E_0 and the electric dipole moment $p = \alpha E_0$. Commonly, the polarizability of a metallic object depends on the frequency and consequently dielectric function $\varepsilon(\omega)$ of the metal and the surrounding medium, as well as on the particle geometry. An LSP resonance is associated with a pole of the polarizability α of the metal particle as a function of frequency (wavelength). For small nanoparticles made of noble metals such as gold and silver, the LSP resonances occur typically in the visible range of the spectrum.
The confined geometry of a metallic nanoparticle acts as a momentum source, generating a localized stationary surface charge density wave in the particle. The momentum provision Δk of the nanoparticle with confined boundaries is roughly approximated as $\Delta k = n2\pi/a$ with a discrete set of LSP modes of order n that can be effectively coupled to light. In Figure 2.1a, the effect of this momentum provision, which allows coupling to light, is illustrated by red-dashed lines. The finite geometry of the metallic nanoparticles does not only allow for coupling to external light, but it also provides a means to tune the energies of the plasmon excitations and to localize and enhance the optical fields in the vicinity of the particles.

2.3.4 *Metallic Nanoparticle As a Simple Optical Nanoantenna*

A structure that enable effective conversion of electromagnetic radiation from the far-field to the near-field and vice versa is considered an optical nanoantenna [62]. In this subsection, to understand the basic concepts of optical nanoantennas, a spherical metallic nanoparticle as a simplest optical nanoantenna is described. The scattering and absorption of a nanoparticle is described by the scattering and absorption cross-sections. The scattering cross-section $C_{scat} = I_{scat}/I_{inc}$ and the absorption cross-section $C_{abs} = I_{abs}/ I_{inc}$ depend on the scattered intensity I_{scat}, the absorbed intensity I_{abs}, as well as incoming intensity I_{inc}. For spherical particles with smaller radius than the incoming wavelength λ:

$$C_{scat} = \frac{8\pi}{3} k^4 a^6 |\frac{\varepsilon_{sph} - \varepsilon_{med}}{\varepsilon_{sph} + 2\varepsilon_{med}}| = \frac{k^4}{6\pi} |\alpha_{sph}|^2 \Rightarrow C_{scat} \propto \frac{\alpha^6}{\lambda^4} \tag{2.1}$$

$$C_{abs} = 4\pi k a^3 \mathrm{Im}\{\frac{\varepsilon_{sph} - \varepsilon_{med}}{\varepsilon_{sph} + 2\varepsilon_{med}}\} = k\mathrm{Im}\{\alpha_{sph}\} \Rightarrow C_{abs} \propto \frac{\alpha^3}{\lambda} \tag{2.2}$$

where α_{sph} is the dipolar polarizability of the spherical particle of radius a in the quasistatic approach:

$$\alpha_{sph} = 4\pi\varepsilon_0 a^3 \frac{\varepsilon_{sph} - \varepsilon_{med}}{\varepsilon_{sph} + 2\varepsilon_{med}} \tag{2.3}$$

where ε_{sph} and ε_{med} are the dielectric function of the particle and surrounding medium, respectively. The wavevector $k = \omega/c$ is related to the frequency ω and the speed of light in vacuum c. When ε_{sph} is constant and the imaginary part of the dielectric function ε'' is negligible, the scattering cross section shows a rather flat spectral response, which translate to zero absorption.

If the sphere is made of a metal and associated with a plasma frequency ω_p, the Drude model provide an approximation to describe the dielectric response ε_{sph} in the optical range is:

$$\varepsilon_{sph} = \varepsilon_{metal} = 1 - \frac{\omega_p^2}{\omega(\omega + i\gamma)} \tag{2.4}$$

where γ refers to the damping of the electrons, originated by the electron-phonon scattering in the metal. The optical properties of the nanoparticle are given by the polarizability in equation 2.3. When losses are small, the pole in the polarizability determines a maximum in scattering and absorption. In the case of a small particle, the expression that determines the optical properties of the nanoparticle is the so-called optical response:

$$\frac{\varepsilon_{sph} - \varepsilon_{med}}{\varepsilon_{sph} + 2\varepsilon_{med}}. \tag{2.5}$$

For the Drude-like dielectric functions in the equations 2.1 and 2.2, which are plotted in Figure 2.2a, the spherical nanoparticles show resonant behavior for scattering cross-section (Figure 2.2b) as well as absorption cross-section (Figure 2.2c). The resonance position appears at the frequency ω_{res} that fulfills $\varepsilon_{sph} + 2\varepsilon_{med} = 0$. By assuming vacuum as the surrounding medium ($\varepsilon_{med} = 1$), the resonance frequency ω_{res} is found at a frequency $\omega_{res} = \omega_p/\sqrt{3}$.

Dipolar surface plasmon of small particles is of interest for two reasons. First, the electromagnetic near-field associated with the plasmon excitation is strongly localized on the scale of the nanoparticle size, typically on the nanometer scale, allowing for an effective squeezing down of the oscillations of the electromagnetic field to sub-wavelength dimensions. Secondly, the LSP

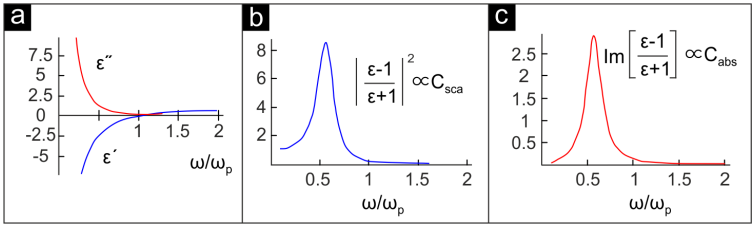

Figure 2.2: (a) The real and imaginary parts of a Drude-like dielectric function as a function of frequency normalized to the plasma frequency ω_p. (b) Modulus of the response function in a small spherical metallic particle shows the spherical surface plasmon dipolar resonance for a Drude-like sphere surrounded by vacuum. (c). The imaginary part of the same response function as in Figure b. A damping of 0.2 ω_p has been used in both cases. The resonances are not maximum at the same frequency, but for small damping, both are located close to the dipolar surface plasmon frequency $\omega_{res} = \omega_p/\sqrt{3}$. Adapted from Ref. [21].

resonances produce a considerable increase of the local fields around the particles ranging from 5 to 500 times enhancement in amplitude. This is the basis of many field-enhanced techniques such as spectroscopy and photovoltaics [21].

One can distinguish two regions around the particles, localized fields (near-field) and the propagating fields (far-field). The electric field E(r) of a dipole characterized by its dipolar momentum p located at the origin of coordinates as a canonical example of an emitter is expressed by the equation 2.6.

$$E(r) = \frac{1}{4\pi\varepsilon_0}\frac{e^{ikr}}{r}\{k^2((n\times p)\times n) + \frac{1}{r}(\frac{1}{r} - ik)(3n(n.p) - p)\}e^{-i\omega t} \tag{2.6}$$

If one assume the dipolar momentum p as the electric dipole given by the static polarizability of a sphere α_{sph}, which is function of the incident field E_0) as introduced above, the field produced by the sphere as a response to the incident field in both

near- and far-field regions can be driven. In the near-field region, where $kr \ll 1$, the equation 2.6 is simplified as:

$$E(r) = \frac{1}{4\pi\varepsilon_0} \frac{3n(n.p) - p}{r^3} e^{-i\omega t} \tag{2.7}$$

This near-field distribution of a metallic nanoparticle normalized to the incident field is shown in Figure 2.3a. From this Figure, one can conclude that a metallic particle acts as an effective optical antenna, which converts propagated electromagnetic energy (far-field) into strongly localized near-fields. Such a high degree of localization of the electromagnetic fields in nanoscale enable various applications such sensing, nanoscale imaging [59], controlling [63], and manipulating the optical signal [64].
On the other hand, in the far-field or radiation zone, where $kr \gg 1$, the field in equation 2.6 is simplified as:

$$E(r) = \frac{(n \times p) \times n}{r} \frac{k^2}{4\pi\varepsilon_0} e^{i(kr-\omega t)} \tag{2.8}$$

Figure 2.3b shows the far-field radiation scattered by the dipolar surface plasmon, which is similar to typical radiation pattern of the dipolar radio-antenna emission. Therefore, the properties of the LSPs will regulate the actual behavior of the optical nanoantenna.

2.3.5 *Influence of Particle Shape in Plasmon Response*

The optical response and resonance condition of a metallic nanoparticle is given by the maximum of its polarizability α, as detailed in the previous subsection. Since for nonspheric particles the polarizability becomes anisotropic, optical responses along the different directions are different. In this case, the polarizability should be defined as a tensor that addresses the optical response along several directions. For the ellipsoid particles with

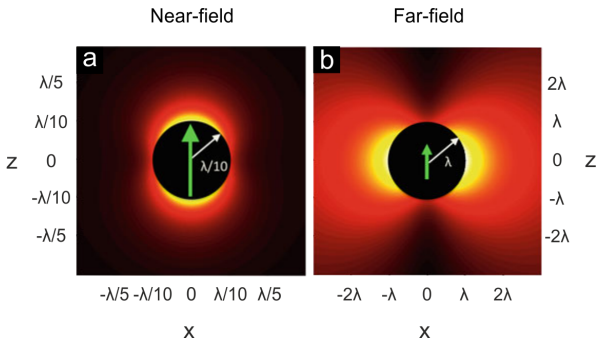

Figure 2.3: (a) Amplitude of the near-field around a plasmonic dipole ($r \ll \lambda$) and (b) the far-field radiation pattern emitted from a plasmonic dipole ($r \gg \lambda$). Adapted from Ref. [65].

one symmetry axis z, the following polarizabilities along the different symmetry axes x, y, z is expressed.

$$\alpha_{x,y,z} = \frac{4}{3}\pi L_x L_y L_z \frac{\varepsilon_{ell} - \varepsilon_{med}}{\varepsilon_{med} + P_{x,y,z}(\varepsilon_{ell} - \varepsilon_{med})} \tag{2.9}$$

Where $P_{x,y,z}$ are the depolarization factors in the direction of the x, y, and z axes, L_x, L_y, and L_z are the antenna lengths along the respective axis. ε_{ell} and ε_{med} are the dielectric function of the plasmonic material and surrounding medium, respectively. If the axes are equal, $L_x = L_y$ and therefore $P_x = P_y$. The depolarization factors $P_{x,y,z}$ are determined by the ellipticity e of the ellipsoid:

$$P_z = \frac{1-e^2}{e^2}\left(\frac{1}{2e}\ln\left(\frac{1+e}{1-e}\right) - 1\right) \tag{2.10}$$

$$P_x = P_y = \frac{1-P_z}{2} \tag{2.11}$$

with

$$e = \sqrt{1 - \left(\frac{L_x}{L_z}\right)^2} \tag{2.12}$$

Figure 2.4, show far-field spectra and near-field distribution of a nanorod when illuminated with polarization parallel and perpendicular to the long antenna axis. When light is polarized along the long axis, the LSP is commonly named as the longitudinal LSP. The resonance associated with the short antenna axis appears at the shorter wavelength and is commonly labeled as the transversal LSP. The near-field distribution of both the transverse and longitudinal LSPs can be observed in Figures 2.4b and 2.4c, respectively. For the longitudinal resonance, a large field concentration at the edges extremities is found because of the large polarizability and sharp edges. A much weaker field enhancement is found for the short axis resonance. The aspect ratio (L_x /L_z), therefore can tune the frequency (wavelength) of both the longitudinal and transverse LSPs [66].

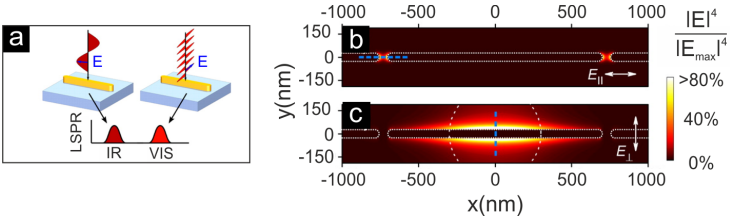

Figure 2.4: (a) Schematic extinction cross-section for the longitudinally polarized light and the transversally polarized light of a illuminated nanorod. (b) Near-field distribution of the longitudinal LSP at the resonant wavelength. (c) Near-field distribution of the transverse LSP in the proximity of the antenna at the resonant wavelength. Adapted from Ref. [67].

Various types of metallic nanoparticle shapes and their corresponding optical properties can be found in the literatures [67, 68]. Advent of lithographic techniques have made it possible to produce the different metallic particle geometries and configurations [69–71]. Besides the standard and canonical shapes

such as spheres and spheroids, other shapes such nanocubes, nanoshells, nanorings, nanocups, nanorice, nanostars can be obtained. The increase in the complexity of the particle geometry requires to go beyond analytical models to calculate their optical response. For this purpose, different computational methods such as dipole–dipole approximation (DDA) [72], finite difference in time domain (FDTD) techniques [73], or boundary element methods (BEM) [74] have been implemented to solve Maxwell's equations in arbitrarily shaped particles.

2.3.6 *Field Enhancement by Plasmon Coupling*

The localized modes of each single particle couple to each other through Coulomb interaction. That results new hybridized modes that are shifted with respect to the single particle resonance [75, 76]. The coupling of two closely spaced spherical nanoparticles in the dipole approximation are the simplest case of such a situation which is shown in Figure 2.5a. One can assign an effective polarizability (α_{eff}) to the coupled particles, which is a function of the particles polarizabilities α_1 and α_2, and the distance between the dipoles r. The effective polarizabilities (α_{eff}) of longitudinally aligned dipoles and transversally aligned dipoles are expressed by [77]:

$$\alpha_{eff}^{long} = \frac{\alpha_1 + \alpha_2 + \frac{\alpha_1 \alpha_2}{\pi r^3}}{1 - \frac{\alpha_2 \alpha_2}{4\pi^2 r^6}} \tag{2.13}$$

and

$$\alpha_{eff}^{trans} = \frac{\alpha_1 + \alpha_2 - \frac{\alpha_1 \alpha_2}{2\pi r^3}}{1 - \frac{\alpha_2 \alpha_2}{16\pi^2 r^6}} \tag{2.14}$$

The tendency of the longitudinal coupling in Figure 2.5b shows

by decreasing dipole separation r, the spectral response shifts to lower frequencies (red shift) and the effective polarizability slightly increases. In contrast to the longitudinally coupled dipoles, the transversally coupled dipoles exhibit a blue shift when the separation r is reduced [78, 79].

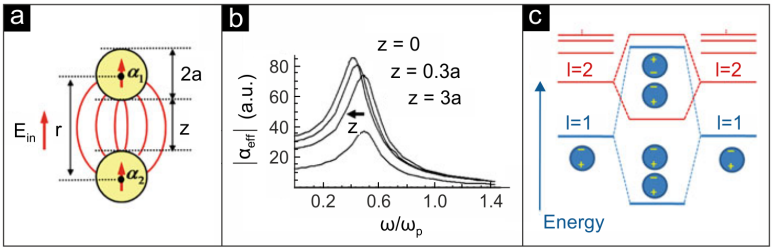

Figure 2.5: (a) Schematics of the longitudinal coupling. (b) The effective polarizability corresponds to the longitudinal coupling. (c) Schematics of the hybridization of the l=1 and l=2 modes of single metallic nanoparticles. As the particles come near to each other, new bonding (lower energy) and anti-bonding (higher energy) modes are created. Adapted from Ref. [21].

Figure 2.6 shows the resonance shift of metallic dimers as a function of the separation distance between the particles [80]. When the distance between the particles is very small, the surface charge densities of each particle interact strongly. This near-field interaction across the gap sustains a strongly localized symmetric surface plasmon mode, also called bonding dimer plasmon (BDP) which presents lower energy and comes from the hybridization of the single dipolar surface plasmons from each particle [81]. A schematic of the energetics of these hybrydized modes can be observed in Figure 2.5c. The formation of the hybridized bonding surface plasmon produces large field enhancement at the particles gap, commonly named as hot spot. A similar coupling can also be found with deferent particle shapes such as triangles or so-called bowtie antenna [82, 83] and rod

nanoantennas [84].

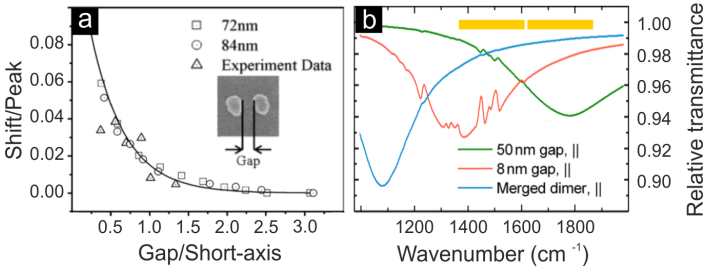

Figure 2.6: (a) The spectral shift of the antenna gap resonance as a function of separation distance of the gap. Adapted from Ref. [80]. (b) Red-shifted spectra due to the decreasing the nanogap sizes. A great shift is observed when the antennas touch each other. Adapted from Ref. [21, 84].

A very interesting regime occurs when metallic nanoparticles nearly touch each other. When the particles are separated by a certain distance, the interaction between both particles leads to the formation of the BDP [85], as described above. The physical situation at the gap can also be understood in terms of circuit theory [86] as a capacitive coupling between the metal particles. As the particles come to very close proximity and touch each other, a conductive connection between both particles is achieved, establishing a charge transfer plasmon [87] that sustains a longer wavelength mode with net charge at each particle. This can be understood within the circuit theory as an inductive coupling [86] between the two particles. The manipulation of the dielectric properties of the cavity to control the response of a nanoantenna (coupled metal nanoparticles) is the optical analog to the manipulation of the gap impedance to tune radiowave antennas.

2.4 PRACTICAL APPLICATION OF PLASMONICS

Plasmonics and metamaterials are in focus during the past two decades. Despite many fundamental breakthroughs and exciting science, however, their promising applications that were initially targeted have not been delivered yet. In this section some theoretical backgrounds of plasmonics applications such as perfect absorption, surface enhanced infrared spectroscopy, and refractory plasmonics are explained. These concepts are experimentally demonstrated in chapters 3, 4, 5, and 6.

2.4.1 *Plasmonics Perfect Absorbers*

Optical devices with the ability of very high absorption of light are of crucial importance for different applications, ranging from infrared imaging [88] to sensitive gas detection [18]. Thin perfect absorbers or so-called metamaterial absorbers offer promising tools for such application. The simple multilayer sample design based on metallic nanostructures that can exhibit near-perfect absorption from visible to mid-infrared wavelengths is introduced in this section. Such a perfect absorber can be utilized for chemical sensing by using the materials which their optical properties can be modified based on different parameters in the perfect absorber design. A schematic view of the perfect absorber design is shown in the Figure 2.7.

The localized plasmon oscillations in the metallic nanostructures are excited by incoming light resulting in charge distribution which leads to the antiphase oscillation of a mirror plasmon in the thick gold film. Circular current distribution and consequent magnetic response of the nanostructure [90], lead to the efficient coupling of the incident light into the nanostructure, where it

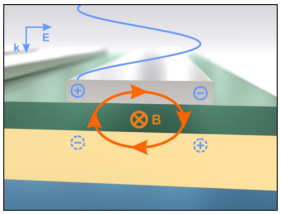

Figure 2.7: Schematic design of a plasmonics perfect absorber which is based on the efficient coupling of incident light into the structure to provide impedance matching condition and consequently suppression of reflection for a certain designed wavelength. Using a gold mirror in a multilayer design allows for suppressing the transmission through the structure, and therefore near-perfect absorption is obtained. Adapted from Ref. [89].

is dissipated as heat in the metallic and the dielectric components.

In a simple model, the nanostructure can be described as an effective medium with complex electric permittivity $\varepsilon(\lambda)$ and magnetic permeability $\mu(\lambda)$. By carefully choosing the geometric parameters of the nanostructure, both ε and μ can be adjusted such that its complex impedance $Z_{struc}=(\mu/\varepsilon)^{1/2}$ is matched to the vacuum impedance $Z_{vac}=1$ in centimetre–gram–second system (cgs) units for a designed wavelength λ_0. This impedance matching results in zero reflection according to following equation.

$$R = \frac{Z_{vac} - Z_{struc}}{Z_{vac} + Z_{struc}} \tag{2.15}$$

The transmission through the sample is completely suppressed by the gold (Au) film. Also as mentioned above, the reflection of the sample at specific wavelength can be suppressed by choosing the accurate geometrical parameters and consequently highest absorption absorption (A) can be obtained (A= 1–R–T=1). This is shown schematically in Figure 2.8. Such a high absorption

can be easily tuned by changing nanostructure size as will be discussed in more details in chapter 3.

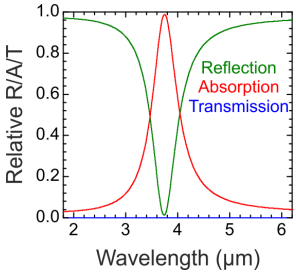

Figure 2.8: Schematic reflection, transmission, and absorption spectra of the metamaterial perfect absorber under normal incidence.

2.4.2 *Surface-Enhanced Infrared Spectroscopy*

The vibrational energies of various type of molecules are typically in order of milli-electron volt (meV) which translates to the infrared range of the electromagnetic spectrum. Since these energy spectra are strongly depend on the chemical bonds, corresponding vibrational signals can be utilized as the fingerprint for chemical identification of substances. Raman and infrared spectroscopy are two most important techniques that can extract the spectral information of these vibrational fingerprints.
Raman spectroscopy uses visible light for sample illumination, where photons interact with molecular vibrations thus inelastic light scattering happens. Therefore the energy between incoming and outgoing radiation is shifted (stokes and anti-stokes shifts). The low scattering cross-sections in Raman Spectroscopy ($\approx 10^{-28}$cm^2/molecule), prevents single molecule spectroscopy.
A complementary spectroscopic technique to SERS, Infrared spe-

ctroscopy, is based on the direct excitation of molecular vibrations using infrared light [91], where extinction cross-sections are of the order of $\approx 10^{-18}$cm^2/molecule is measured using typical transmission and reflection spectroscopy. Such weak cross-sections can be enhanced by adsorbing the molecules in the vicinity of metallic surfaces, where local field enhancement is produced [92]. This spectroscopic technique is commonly addressed as Surface-Enhanced Infrared Spectroscopy (SEIRA).This spectroscopic technique, enhance signal by generating surface plasmon polaritons or by antenna resonances, is called surface-enhanced infrared spectroscopy (SEIRA). Such a mechanism can also accrue in Raman scattering which labeled surface-enhanced raman spectroscopy (SERS). The basic idea of both SERS and SEIRA is to locate the molecules on top of the hot spots produced by the LSP or the antenna, as schematically shown in Figure 2.9.

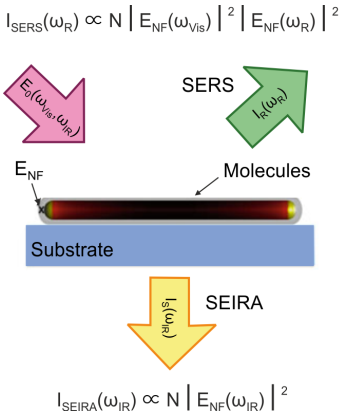

Figure 2.9: Schematics illustration of SERS and SEIRA as two most commonly used spectroscopic techniques. Molecules are located close to the metallic nanostructures which act as optical antennas. The inelastic scattering and the absorption signals from the molecular are enhanced. Adapted from Ref. [21].

The spectral information in SEIRA is usually obtained in transmission mode, as schematically shown in Figure 2.9, therefore the obtained information contains both absorption and scattering processes. In this section, SEIRA is on the focus of discussion, as it is incorporated experimentally in the large-area plasmonic nanoantenna arrays in Chapters 4 and 5.
Surface-enhanced spectroscopy was initially implemented in intense local fields at the gaps and protrusions of the rough metallic surfaces. Such areas are called hot spots due to their high local field and strong localization. The concept has been developed in the recent years by using of metallic nanostructures which act as optical antennas and enhance local fields at specific resonance frequencies. The field enhancement can be few orders of magnitude higher than the incoming amplitude which enables one to detect signals from only a few or even single molecules [93, 94].

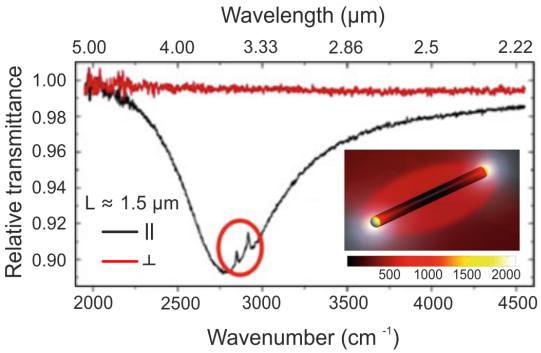

Figure 2.10: (a) Absorption spectroscopy of molecules adsorbed on top of a single gold nanoantenna.The enhanced signal of the molecules is circled by the red line. The inset shows local field intensity of a 1.341 μm long nanoantenna. Adapted from Ref. [95].

To achieve localized and intense signals in SEIRA, a significant

field enhancement is required. The main approach is to use antennas resonating at IR range. Therefore, such antennas have micrometer-dimensions. For instance, a gold nanoantenna with the length $L = \lambda/2$ acting as a linear dipole antenna [95].
Figure 2.10 (inset) shows hot spots are obtained at the nanoantennas edge, resulting in enhanced IR spectra from a few molecules attached on the antenna surface. This effect can be observed in transmission spectra where a broadband IR antenna resonance is clearly visible when the polarization of the incoming light is parallel to the antenna's long axis (black line). Two narrow kinks marked by a red circle are observed which correspond to the vibrational fingerprints of molecules attached to the antenna. When the polarization of the incoming light is parallel to the antenna's short axis, no antenna resonance is observed (red line) and consequently, vibrational fingerprints can are not visible. This experiment shows the power of SEIRA to overcome the limitation detection in IR spectroscopy. Due to the electromagnetic interference between the local field of the nanoantenna and the field of the molecular vibrations, the vibrational signals of the molecules appear as peaks rather than dips [95] which is similar to the quantum mechanical Fano effect. Antenna-assisted SEIRA can be further optimized by using more complex antenna structures [96–99].

2.4.3 *Refractory Plasmonics*

In order to improve the efficiency of current plasmonic designs and to realize novel concepts, there is an increased need for additional classes of plasmonic materials. Therefore, most of the recent studies are focused on the investigation of the new materials for plasmonics application. Among the desirable optical

properties of alternative plasmonics materials, metal-oxide semiconductor compatibility, bio- and chemical compatibility, tunability, and low losses have attracted great attention [100]. Also, high-temperature stability is a very promising feature in the field of plasmonics.

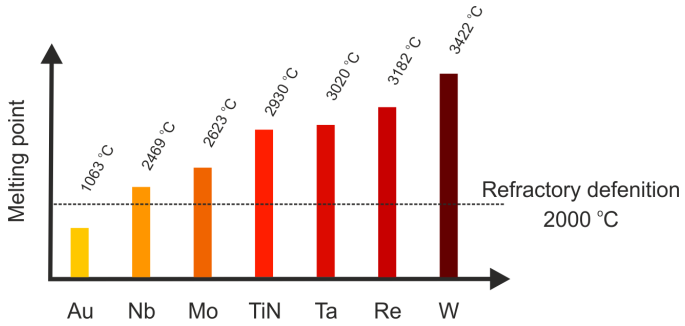

Figure 2.11: Refractory plasmonic materials are featuring high-temperature durability. The graph compares melting points of different refractory materials.

Refractory materials are featuring melting point and chemical stability at temperatures above 2000 °C. Refractory materials are usually nonmetallic and they cover a wide range of applications including industrial furnaces, space shuttle shields, and semiconductor technology. The wide range of metals have also been tried for high-temperature applications; however, the optical properties of those metals that have been studied were not satisfying to be used in plasmonic applications where they are almost based on noble metals. Refractory materials that exhibit reasonably good plasmonic behavior would undoubtedly open a door to new devices and strongly improve the uses of the existing applications such as heat-assisted magnetic recording (HAMR) [101], solar and thermo-photovoltaic [102], plasmon-assisted chemical vapor deposition [103], solar thermoelectric

generators [104], as well as nanoscale heat transfer systems [105]. Figure 2.11 compares the melting points of different refractory materials compare to gold as the most common metals that are used in the plasmonic application.

The main challenges of using noble metals in practical application come from several parameters such as poor chemical and thermal stability and high losses [100]. The losses cause heating of the plasmonic material and therefore, temperature arise in a confined volume around the nanostructure. Because of this local high-temperature, the mechanical and chemical stabilities of plasmonic nanostructures would be essential and refractory plasmonic materials are therefore obligatory. Several plasmonic applications with a great potential for practical use, such as photothermal treatment [106] and HAMR [101], rely on the heating effects.

One of most important application of refractory materials in plasmonics is in solar thermophotovoltaics technology where the basic idea is to absorb solar irradiation with using a broadband absorber, resulting in heating of an intermediate component. Subsequent emission of this thermal energy in a narrow spectrum can be utilized for efficient absorption by the photovoltaic cell with the energy conversion efficiencies of about 85% as theoretically investigated by Shanhui Fan [102]. The operational temperatures of the suggested device; however, are estimated at ~1500^{o}C, and therefore, the emitter materials that sustain at high temperatures in the long exposure time should be developed.

Refractory plasmonic materials are great solutions for the high-temperature durability limitations of current plasmonic devices to advance the existing S/TPV technology. Using ultrathin metamaterial absorbers and emitters made of the same refractory

plasmonic material allows for a narrow intermediate spectral converter, that can be easily heated [107].
Absorber and emitter devices [108] based on refractory metals have been fabricated [109, 110]; however, the working temperature of such devices are still far below the desired values. Also, using the protective layers made of refractory dielectric materials [110] will not provide enough stability at higher the temperatures.
To overcome this problem, the proper constituent materials should be used which can open a new door for high-temperature applications of advanced plasmonic and metamaterial devices. For instance, the transition metal nitrides such as titanium nitride and zirconium nitride, that exhibit plasmonic properties comparable to noble metals in the visible and near-infrared spectrum [111]. These materials can extremely improve the efficiency of S/TPV devices by incorporating their intrinsic refractory properties. Therefore, the traditional noble metals such as gold and silver or other refractory materials with poor optical properties can be replaced.

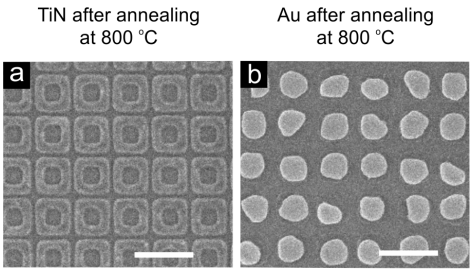

Figure 2.12: SEM images of (a) the TiN nanostructure after annealing at 800°C around 8 h. (b) The SEM images of Au nanostructure after annealing at 800°C around 15 min. Adapted from Ref. [113].

Figure 2.12 compares the high-temperature stability of the tita-

nium nitride and gold nanostructures. Au nanostructures melt into nanoparticles in the metamaterial absorber even only after 15 minutes of annealing at 800°C as indicated by the SEM image in Figure 2.12 while titanium nitride sustains after 8 hours annealing at the same temperature. This can be understood by the fact that bulk TiN has a melting point of 2930°C, much higher than that of Au (1063°C). One can assume the TiN absorber may work at temperatures much higher than 800°C if the oxidation is prohibited with an optically transparent protective layer or by keeping it in vacuum or in noble gases [112, 113].
An experimental investigation of the plasmonic behavior of TiN at high temperatures and effect of using the protective layer on top to prevent the oxidation is presented in chapter 6.

2.5 NANOFABRICATION TECHNIQUES FOR PLASMONICS APPLICATIONS

Well-defined metallic nanostructures have been considerably in focus for plasmonic applications recently. This section aims at giving an overview of the different nanofabrication techniques used in the thesis.

2.5.1 *Lithography: Evolution and Resolution*

Mask-assisted photolithography is the major lithographic technique that has been used in the development of microelectronics. The large-scale integration concept of the feature sizes enables thousands of transistors into a single chip.
In this technique, usually an ultraviolet light is exposed to a photoresist-coated thin film through a mask. The sample is moved stepwise along the light sheet in order to allow multi-

exposures over the large-scale. Photolithography is a diffraction limited technique since it is based on the projection of a mask via lenses. The mask for a feature sizes smaller than the wavelength of the light source will not restrict the illumination pattern, however, the pattern is limited by the numerical aperture (NA) and according to the Airy formula:

$$a = 1.22\frac{\lambda}{NA} \tag{2.16}$$

while NA = nsinθ is the numerical aperture of the lens, n the refractive index of the surrounding medium and θ is the projection angle. According to this simple formula, there are two possibilities to decrease the feature sizes.

The first possibility is to reduce the wavelength of the light source which has been decreased over the years from visible to the deep ultraviolet (UV). The second solution is to use the higher numerical aperture by utilizing medium with a refractive index larger than 1. This can be done also by using the immersion lithography.

In equation 2.16, by using a typical UV source and a numerical aperture of 1, the resolution limit is estimated by $\lambda/2$ or roughly 150 nm. This is larger than a typical plasmonic particle which resonates in the visible range. Currently by using 193 nm light source combined with immersion lithography, phase-shifting techniques and double-patterning 45 nm feature size is achievable in microelectronics. X-ray lithography with a typical wavelength of 13.4 nm is the most promising light source for this approach but there are main issues that are limiting the use of X-ray. The X-ray source efficiency is too low (2×10^{-7} %). Also, the nature of the X-rays prevents working in transmission and obtaining a reflective surface with high efficiency, multilayers coating with typical periodicity smaller than 10 nm is required.

Therefore, the cost of the lithographic tools has exponentially increased. Based on this, photolithography does not seem to be the best option as low-cost fabrication method and high throughput plasmonic structures.

2.5.2 *Electron-Beam Lithography*

In 1936 it was proposed to use accelerated electrons instead of photons for microscopy. The wavelength associated with 100 keV electrons can be as small as 3.9 pm, which is much smaller than the atomic scale. Based on equation 2.16, the diffraction limit should no longer be an issue and the atoms become visible using electron microscopy. Nowadays, it is common to use thin samples to observe at the atomic scale in transmission microscopy. The same electron beam was used to expose an electron-sensitive photoresist leading to electron-beam lithography as first reported in 1960 with the writing of 50-nm features [114].

The main steps of electron-beam lithography combined with the lift-off technique are illustrated in Figure 2.13. First, high energy electron beam is applied on the e-beam resist layer. The high energy electron beams break the long chain polymer of the resist and make it solvable in the developer solution (Figure 2.13a).

This exposure mode allows writing any geometry which is usually defined by a computer-aided design software. After exposure, the photoresist is developed in a solvent. Smaller chains in the exposed area lead to a material of higher solubility and therefore to a faster dissolution rate of the corresponding area (Figure 2.13b).

Afterward, the pattern can be transferred using an etching process. Another possibility is using the lift-off process which con-

sists in metalization of the sample via evaporation techniques. This process can be only done by making so-called inverted profiles to enable discontinuity between the metal deposited onto the substrate and the resist (Figure 2.13c). In addition to the inverted profile, a reasonable ratio of metal:resist thickness (at least 1:3) should be used to prevent any contact. Finally, to dissolve the remaining resist and consequently lifted up unwanted metal areas, the sample is dipped in a solvent (Figure 2.13d).

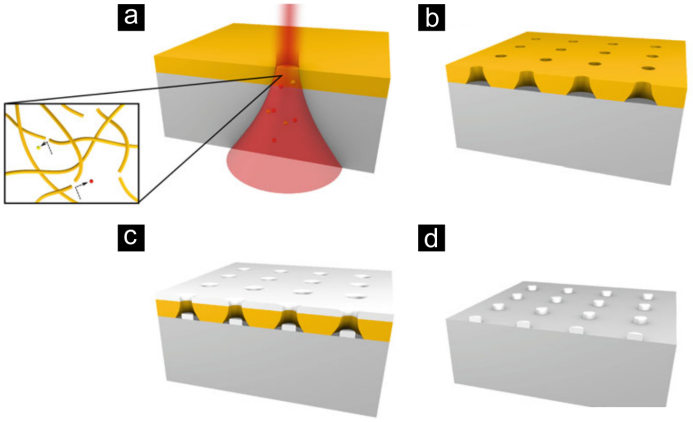

Figure 2.13: Electron-beam lithography is used for the selective and local deposition of metals. (a) Electron-beam exposure (red color) of the resist (yellow color) leads to break polymeric chains. (b) Inverted photoresist profile is achieved after development. (c) Metal (white color) is coated and (d) the structures remain after the stripping of the photoresist in a solvent. Adapted from Ref. [21]

Vieu et al. [115] have extensively demonstrated the electron-beam lithography resolution can be pushed below 10 nm for isolated structures and that the intrinsic resolution limit of the writing process in the resist can be as small as 3–5 nm at high energy (200 kV).

Although EBL allows for precise controlling of the nanostruc-

ture, however, it produces small-area, cost-intensive and time-consuming samples. In principle, state-of-the-art photolithography methods such as used in the semiconductor industry nowadays enable a fast and homogeneous production of decimeter-sized arrays of nanometer-sized and well-defined metal structures. However, mask fabrication for this process is expensive and inflexible, and particularly at the research level, the low-cost access to such facilities is quite limited.

2.6 ALTERNATIVE LITHOGRAPHIC TECHNIQUES

In this section, alternative or complementary lithographic techniques such as laser interference lithography as well as direct laser writing for fabrication of plasmonics nanostructures are briefly reviewed.

2.6.1 *Laser Interference Lithography*

Laser interference lithography (LIL) is a rather simple technique allowing for fabrication of sub-100-nm structures. LIL enables large-area and low-cost preparation of periodic or quasiperiodic nanostructures via fast fabrication process. In LIL interference pattern of two beams is recorded in a photosensitive material and can be metalized subsequently. Figure 2.14a illustrates a Lloyd configuration which is commonly used in LIL setups. For instance, the 70-nm wide line pattern in a photoresist obtained with such a configuration is shown in Figure 2.14b [116].
More recently, 50-nm period gratings have been obtained by the so-called multilevel interference lithography, where each grating level is patterned with a phase shift with respect to a reference grating [117]. This process could be used for the fabrication

of more complex periodic structures or metallic gratings [118]. Despite advantages and achievable feature sizes, this technique has been extensively applied to plasmonic structures.

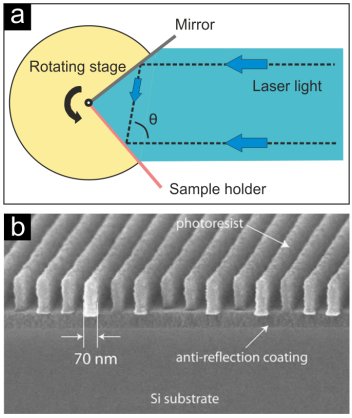

Figure 2.14: LIL is used to produce the periodic structures over large-scales. (a) One beam laser interference lithography setup which is known as Lloyd configuration. (b) An example of sub-100-nm pitch grating fabricated by LIL. Adapted from Ref. [116].

2.6.2 *Direct Laser Writing*

Direct laser writing is sub–diffraction-limited fabrication method which allows performing a fast optical lithography to make arbitrary nanostructures. In most of the DLW process, photopolymerizations are based on the two-photon-absorption processes. In this scheme, a resin is illuminated by laser light at a frequency below the single-photon polymerization threshold but when the laser light is tightly focused enough, the light intensity inside a small volume in the photoresist exceeds the threshold of polymerization.

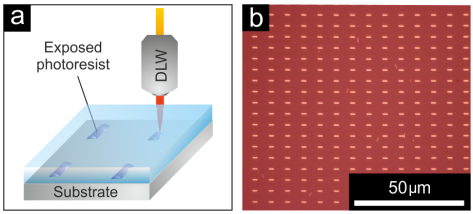

Figure 2.15: (a) Illustration of the direct laser writing process. The laser beam selectively scans and exposes the sample. (b) The nanostructures are achieved on the substrate after the development process. Adapted from Ref. [19]

Although direct laser writing has become a well established, versatile, and commercially available device for printing 3D devices, but it can also be utilized for writing 2D nanostructures at the interface between the substrates and the photoresist. Combining this method with etching or lift-off processes allows for metalization of the patterns. Figure 2.15 illustrates the direct writing process in a bulk polymer.
In the following chapters both laser interference lithography and direct laser writing are utilized for the preparation of large-are nanostructures for manufacturing of plasmonic devices such as plasmonic perfect absorber and SEIRA substrates.

3

LARGE-AREA PLASMONIC PERFECT ABSORBER CHEMICAL SENSOR

Perfect-absorber-based plasmonic sensors have attracted significant interest in recent years, owing to their ability to detect minute changes in the optical properties of the involved materials. This is especially important in the context of hydrogen (H_2) sensing, since small amounts of hydrogen gas in air can already lead to highly dangerous and explosive situations.

Tuning of the perfect absorption wavelength can be realized by adjusting the size and shape of the constituent nanostructures. This is highly desirable especially for sensing applications. However, to match such high sensitivity with real-world applications, a fast, low-cost, and homogenous fabrication of arbitrarily shaped and arranged nanoantennas over cm^2 areas is essential. These requirements are still lacking a practical solution.

In this chapter, for the first time laser interference lithography and subsequent argon (Ar) ion beam etching for the fabrication of large-area plasmonic perfect absorber sensors is introduced. Up to now, there were several methods published that suffer either from relative low sensitivity, i.e., randomly arranged metal films [2], chemical synthesis [4, 5, 13], or high time and cost expenditures, when using electron beam lithography [119]. Laser interference lithography, however, combines the advantages of both approaches in a unique way and thus allows for the fast and homogeneous preparation of arbitrarily shaped and arranged nanostructures featuring easily tunable absorption in wide

spectral ranges.

*Laser interference lithography is employed as a reliable and low-cost fabrication method to create nano-wire and nano-square arrays in photopolymers for manufacturing plasmonic perfect absorber sensors over homogenous areas as large as 5.7 cm^2. Subsequently, the fabricated patterns are transfered into a palladium (Pd) layer by using argon ion beam etching. Geometry and periodicity of the large-area metallic nanostructures are precisely controlled by adjusting the interference conditions during single- and double-exposure processes, resulting in active nanostructures over large areas with spectrally selective perfect absorption of light from the visible to the near-infrared wavelength range. In addition, the method's applicability for hydrogen detection schemes is demonstrated by measuring the hydrogen sensing performance of the polarization independent palladium-based perfect absorbers. Since palladium changes its optical and structural properties reversibly upon hydrogenation, exposure of the sample to hydrogen causes distinct and reversible changes within seconds in the absorption of light, which are easily measured by standard microscopic tools. The fabricated large-area perfect absorber sensors provide nearly perfect absorption of light at 730 nm and 950 nm respectively, and absolute reflectance changes from below 1% to above 4% in the presence of hydrogen. This translates to a relative signal change of almost 400%. The large-area and fast manufacturing process makes this approach highly attractive for simple and low-cost sensor fabrication, and therefore, suitable for industrial production of plasmonic devices in the near future.

* This Chapter is adapted from S. Bagheri et al., Large-Area Low-Cost Plasmonic Perfect Absorber Chemical Sensor Fabricated by Laser Interference Lithography, *ACS Sensors* 1, 1148-1154 (2016). Reprinted with permission. Copyright 2016 American Chemical Society.

3.1 BASIC PRINCIPLES

The interaction of light with metallic nanostructures reveals unique optical properties originating from the excitation of localized surface plasmon resonances [120–123]. Among the intriguing optical effects found in such systems, high or perfect absorption of light at a specific wavelength is used for a wide range of applications such as photovoltaic efficiency enhancement [124, 125], color printing [126, 127], spectroscopy [128, 129], and sensing [130, 131]. Tuning of the perfect absorption wavelength, which is highly desirable especially for sensing applications, can be realized by adjusting the size and shape of the constituent nanostructures [16, 20]. Perfect-absorber-based plasmonic sensors have attracted significant interest in recent years, owing to their ability to detect minute changes in the optical properties of the involved materials. This is highly important in the context of hydrogen (H_2) sensing, where small amounts of hydrogen gas in the air can already lead to highly dangerous and explosive gas mixtures [132]. There are several materials that change their optical or mechanical properties upon hydrogen exposure and can, therefore, be used in optical sensing schemes, such as palladium (Pd) [133], yttrium (Y) [134], and magnesium (Mg) [135]. Other than palladium, where the change of the dielectric properties due to hydrogenation leads to a shift of the plasmonic resonance, yttrium and magnesium undergo a complete phase transition from a metallic into a dielectric state. However, their lack of catalytic properties requires the addition of catalytic palladium or platinum elements to facilitate hydrogen dissociation, increasing the complexity of the nanostructures.

The concept of plasmonic perfect absorption is based on the effi-

cient coupling of incident light into the structure through matching of its optical impedance to the impedance of the surrounding medium, leading to a near-complete suppression of reflection (R) for a certain design wavelength [90]. By simultaneously suppressing the transmission (T) through the structure, near-perfect absorption can be obtained. In the visible wavelength range, this can be achieved by utilizing a perfect absorber consisting of palladium nanowires, separated from a gold covered substrate by a magnesium fluoride (MgF_2) spacer layer [119]. As mentioned above, the reflection can then be tuned to nearly zero by carefully adjusting the geometrical parameters of the system to provide perfect impedance matching of the vacuum impedance and consequently maximizing the absorbance A= 1 – T – R to almost 1. This measurement scheme is highly interesting for many sensing applications since it provides a high contrast ratio, going from (almost) no signal to a significantly higher signal at the position of minimum reflectance. Even if not perfect absorption (for example a value over 90% but not over 99%) is achieved, the enhanced relative signal change is advantageous for any kind of sensor.

Precisely defined and tailored nanostructures are essential for realizing such nanoplasmonic sensor schemes. Electron-beam lithography is a commonly used method to create well-defined masks for the fabrication of plasmonic perfect absorbers over small areas. However, a fabrication method for producing perfect absorbers in a low-cost and high-throughput manner over large areas is crucial to advance plasmonic sensors towards technological applications. Other methods such as self-assembly [2], chemical synthesis [3], metal nanoparticle deposition [4, 5] and colloidal etching lithography [13] have been proposed for the fabrication of plasmonic structures over large areas, but of-

ten suffer from large-scale inhomogeneity. Compared to other promising large-area fabrication methods, laser interference lithography (LIL) [17] shares many of the advantages of other lithographic techniques while alleviating a majority of concerns such as cost and complexity. It also provides well-defined, defect free and homogenous arrays of nanostructures over large areas, enabling high-performance perfect absorbers on the wafer scale. Through wafer scale production, standardized and robust measurement schemes with macroscopic cm^2 sized samples are possible, providing care-free user friendly devices.

Here, laser interference lithography and subsequent argon ion beam etching are employed to fabricate large-area plasmonic perfect absorbers. A perfect absorber sensor geometry based on palladium nanowire arrays is fabricated and its hydrogen sensing performance is demonstrated. This geometry provides highly sensitive hydrogen detection but requires the incident light to be polarized perpendicular to the wires. Therefore, this concept is subsequently extended towards the fabrication of large area palladium based perfect absorber sensors with rectangular nanoantennas, which provide perfect absorption of light independent of the incident polarization. Extensive numerical simulations are carried out to find an optimal design, and the hydrogen sensing performance of a fabricated polarization independent sensor is investigated. The high-throughput and low-cost fabrication method combined with the simple concept of a plasmonic device that provides pronounced signal changes in response to external stimuli makes the sensor well suited for real-world applications.

3.2 PALLADIUM-BASED PLASMONICS PERFECT ABSORBERS

Laser interference lithography is a low-cost fabrication method to prepare homogenous nanostructures over large areas. It relies on the interference of two coherent laser beams, which produces a standing wave grating pattern that can be transferred to a light sensitive photoresist for the preparation of one-dimensional wire structures [136]. Furthermore, the addition of a second exposure process enables the fabrication of geometrically tunable 2D-nanostructures [137]. Such nanostructures are transferable to metal via a subsequent etching process [19, 138]. Here, single and double-exposure processes are utilized to fabricate homogenous palladium nanowire and rectangle arrays for plasmonic perfect absorbers.

In preparation for the fabrication process, fused silica substrates are cleaned with acetone and isopropanol for 10 minutes in an ultrasonic bath. After that, 2 nm of chromium (Cr, adhesion layer) followed by 150 nm gold (Au, mirror), magnesium fluoride (MgF_2, spacer) and palladium (Pd, hydrogen sensitive material) are evaporated onto the substrate (Pfeiffer vacuum model PLS-500, 10^{-7} mbar). Afterward, a 90 nm thick photoresist film (ma-N 405) is spin-coated on top of the Pd layer. For the subsequent exposure process, an expanded light beam of a He-Cd laser (λ = 325 nm) and a Lloyd's mirror setup [139] are used. Typical UV exposure doses are about 1 mJ/cm² with typical exposure times of 30 seconds (s). To achieve two-dimensional structures, the sample is rotated 90 degrees followed by a second exposure process. Subsequently, the sample is immersed into the development solution (AZ 826) for 30 seconds. The areas covered with the developed photoresist are then transferred into the Pd layer via an argon ion beam etching process (Tech-

nics Plasma model R.I.B.-Etch 160, beam current range from 90 to 100 mA, typical etching times between 70 and 100 seconds). Finally, the remaining photoresist is removed using isopropanol followed by O_2 plasma treatment (Diener Electronic Plasma-Surface-Technology, 90 minutes, 1.4 mbar, 160 W).

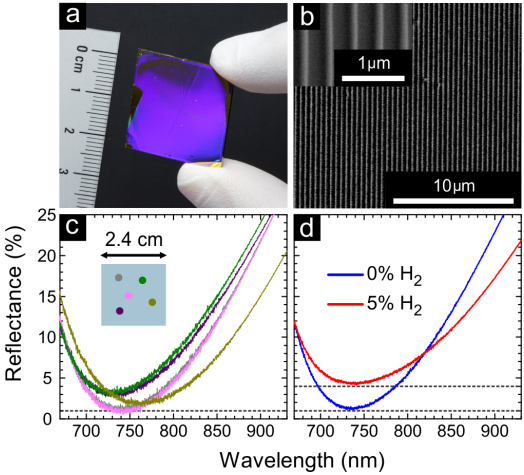

Figure 3.1: Large-area palladium-based one-dimensional perfect absorber sensor fabricated by laser interference lithography. (a) Photograph and (b) scanning electron microscope (SEM) image of a typical sample showing the homogeneity of the plasmonic structures over large areas. (c) The homogeneity is also confirmed by reflection measurements of five different areas of the sample. (d) The reflectivity of the sample (blue line, about 1% minimum reflectance) undergoes a pronounced increase after exposure to 5 vol.% hydrogen in N_2 carrier gas (red line, about 4% minimum reflectance). The typical sample size is 2.4×2.4 cm^2.

A photograph and also a scanning electron microscope (SEM) image of a typical large -area perfect absorber fabricated by laser interference lithography (sample size of 2.4×2.4 cm^2) are shown in Figures 3.1a and 3.1b respectively, demonstrating the large-area nature and homogeneity of the sample. The photo-

graph was taken with a Canon EOS 60D camera with a Canon EF100 mm f/2.8 Macro USM (f/8, 1/4°s, ISO 100). The sample was illuminated with a large diffuse light source (daylight color temperature). The scanning electron micrographs were acquired with an S-4800 scanning electron microscope (Hitachi Company).The periodicity of the depicted grating is 450 nm, the wire width is 120 nm, the spacer height is 65 nm and the Pd structures have a thickness of 20 nm. The homogeneity is additionally confirmed by reflectivity measurements of five different areas of the sample (indicated as colored points in the inset of Figure 3.1c). The measurements show less than 5% deviation in spectral location and modulation depth (Figure 3.1c) and a typical reflectance measurement for polarization perpendicular to the wires shows a minimum reflectance of about 1% and thus nearly perfect absorption of light at the resonance wavelength of 740 nm (blue curve).

The optical properties of the Pd nanowires are modified in the presence of H_2 through the phase transition from palladium (Pd) to palladium hydride (PdH) [140]. The significant change in real and imaginary part of the palladium dielectric function destroys the optimized impedance matching condition of the perfect absorber and consequently changes the reflectivity profile of the system. This can be observed in the spectra as a spectral redshift of about 10 nm and an increase of the minimum reflectance from 1% to 5% when exposing the sample to 5.0 vol.% hydrogen in nitrogen (N_2) carrier gas (Figure 3.1d).

3.3 POLARIZATION INDEPENDENT PERFECT ABSORBERS

To bring this approach to technological and life-science applications, a polarization independent system with two-dimensional

symmetric nanostructures is required. This is easily achievable using laser interference lithography in a double-exposure process. The schematic side view of such a perfect absorber is depicted in Figure 3.2a, where square palladium nanoantennas are stacked above a gold mirror separated by a MgF_2 spacer layer.
To estimate the optical properties of the nanostructure, simulations using a scattering matrix method [141] are performed to calculate the reflectance spectra of square nanoantenna arrays (periodicity 560 nm, Pd thickness 30 nm) for different square widths and spacer heights. Afterward, the lowest reflectance (Figure 3.2b) and the corresponding spectral location of the minimum (Figure 3.2c) are extracted. The figures indicate that square widths between 160 to 250 nm and spacer heights between 70 to 75 nm are expected to provide the best results. A target point with the square width of about 190 nm and spacer height of about 71 nm is indicated by the white circle and dashed lines in the color plots (The reflectance is shown as a logarithmic color scale for better visualization).
According to the simulations, the working range of the large-area perfect absorber can be tuned from 800 to 1300 nm by changing the rectangle size from 150 to 250 nm. The main experimental constraint for tunability is given by the fact that the laser interference method only allows nanostructure sizes between 20 and 75% of the periodicity (560 nm in this case). Nevertheless, the Lloyd's mirror setup enables full control of the periodicity from the UV up to about 900 nm and therefore full tunability of the square widths. Even higher periodicities are accessible using other laser interference lithography setups [17, 136].
To achieve polarization independent perfect absorption of light over large areas, palladium square arrays (periodicity 560 nm, square width 190 nm) are fabricated. An SEM image of the

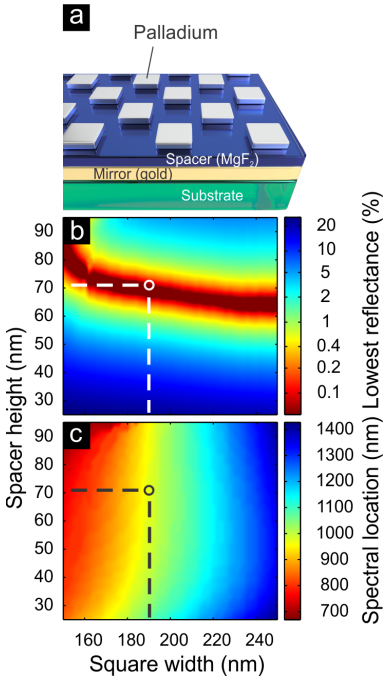

Figure 3.2: (a) Schematic view of the large-area perfect absorber sensor. (b) Simulated minimum reflectance for different square widths and spacer heights. The suitable parameters for a perfect absorber are located in the dark red area (The reflectance is shown in a logarithmic color scale for better visibility). (c) The spectral locations of the minimum reflectance (i.e., perfect absorption) for corresponding square widths and spacer heights. The target square width and spacer height for fabrication are indicated by the white circle.

sample is shown in Figure 3.3a, demonstrating high homogeneity over large areas. The angular behavior of the structure is studied by angle-resolved reflectance measurement for both p- and s-polarization (Figures 3.3b and 3.3c, respectively). The angle-resolved reflectance measurements are performed via a free-space, goniometer-based angular-resolved reflectivity setup.

The light intensity from a xenon lamp, coupled to a monochromator and polarized using input polarizer, is detected via a silicon detector with output analyzer. The light beam is highly collimated (angular divergence smaller than 0.15 degree) and has a diameter of about 1 mm. The incident angle was varied between 20 and 50 degrees in steps of 10 degree.

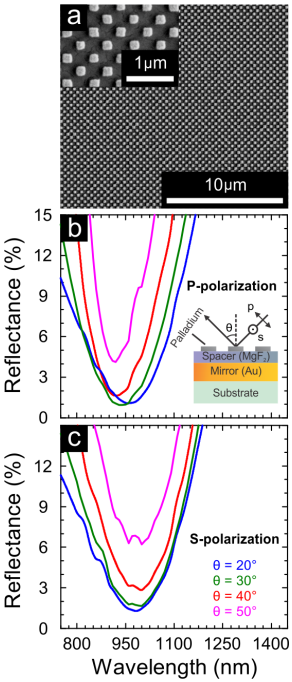

Figure 3.3: (a) SEM image of square palladium nanoantenna arrays utilized in a large-area plasmonic perfect absorber sensor fabricated by laser interference lithography. (b) and (c) Angle-resolved reflection measurements for p- and s-polarization show a residual reflectance below 7% for incident angles up to 50 degree. In p-polarization, the reflectance spectra shift to lower wavelengths for higher incident angles, whereas the spectral location of lowest reflectance in s-polarization remains constant.

In both polarizations, the minimum reflectance re-mains below 7% for incident angles up to 50 degree. This means that the device is able to maintain near-perfect absorption even at high angles, making it a good candidate for technological applications. The small observed changes in reflectance at higher angles are expected for arrayed elements due to the onset of evanescent grating modes, and can only be avoided by using plasmonic perfect absorbers with disordered structures [142].

3.4 HYDROGEN SENSING

The reflectance spectrum of the fabricated perfect absorber at normal incidence and excitation by unpolarized light shows nearly perfect absorption (i.e., R= 1%) at the target wavelength of 950 nm (Figure 3.4a, blue line). This is in excellent agreement with the simulations (see Figure 3.2b, 3.2c). Small differences are expected since the nanostructuring process, including evaporation, photoresist patterning, and etching, can introduce impurities and defects into the system.

The gas concentration-dependent reflection measurements under normal incidence are performed using a commercial Fourier transform infrared spectroscopy system (FTIR), allowing for laterally resolved measurements on the micrometer scale. For the hydrogen-dependent measurements, the sample is mounted in a custom-made vacuum-tight gas cell connected to Bronkhorst mass flow controllers that regulate and monitor the hydrogen and nitrogen gas flows during the measurement with very high accuracy (0,5% Rd). Exposing the sample to low hydrogen concentrations (e.g. 2 vol.% H_2 in N_2) causes only small changes in the minimum reflectance of the perfect absorber, introducing a small wavelength shift to higher wavelengths (about 9 nm) and a

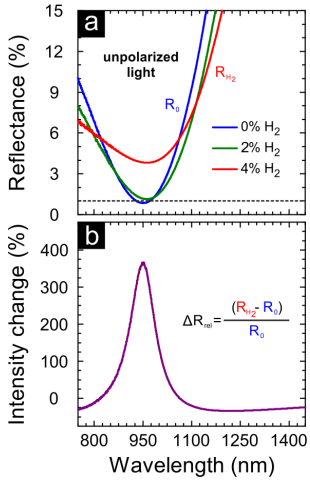

Figure 3.4: (a) Reflection measurement of the large-area perfect absorber for different H_2 concentrations in the N_2 carrier gas. The initial reflectance of the sample (blue line) increases after hydrogen exposure (green line, 2%; red line, 4% hydrogen in nitrogen). (b) Relative reflectance change ($\Delta R_{rel.}$) between the 0% and 4% hydrogen concentrations over wavelength, indicating signal changes of almost 400%.

slight decrease of the absorbance (Figure 3.4a, green line). However, using slightly higher hydrogen partial pressures (4 vol.% H_2 in N_2) causes a pronounced change of the reflectance spectrum. In addition to the wavelength red-shift of about 13 nm, a spectral broadening of the reflection profile as well as a reflectivity increase from 1% to about 5% (Figure 3.4a, red line) is visible. The strong relative reflectance changes ($\Delta R_{rel.}$) of about 400% at minimum reflectance, induced by relatively small changes in environmental hydrogen concentration, demonstrate the performance advantages of the perfect absorber sensing scheme (see Figure 3.4b). The palladium/hydrogen interaction is reversible, allowing the minimum reflectance of the system to return to its

initial state after removing H_2.

To investigate this sensitivity of the perfect absorber to hydrogen gas in detail, a second sample with the reflectance minimum at about 900 nm is fabricated . The sample then is exposed to various hydrogen concentrations and its reflectance changes over the time is continuously monitored during both the loading and unloading processes (Figure 3.5a). After a pure N_2 atmosphere, the concentration sequence starts with 600 s of 0.5 vol.% H_2 in N_2, followed by 2000 s of pure nitrogen, then 600 s at 1 vol.% H_2 and so on, until a maximum H2 concentration of 10 vol.% is reached.

The temporal and spectral response of the perfect absorber sensor during hydrogen exposure is shown as a color-coded plot in Figure 3.5a, indicating the wavelength shift as well as the reflectance (R) change for each spectrum on a logarithmic color scale. To quantify the spectral shift of the perfect absorber resonance during the concentration sequence, the centroid wavelength (CWL) is calculated from the FTIR reflectance measurements, which enables the detection of small resonance shifts independent of the shape and noise characteristics of the spectral features [143]. The initial reflectance minimum (at 897 nm) undergoes a 3 nm shift to higher wavelengths when applying a hydrogen concentration of 0.5 vol.% H_2 in N_2 and further redshifts when higher hydrogen concentrations are applied (see Figure 3.6.

The time traces of the reflection at different wavelengths are shown in the Figure 3.7 which indicates that the changes in reflection become smoother with increasing wavelength.

In Figure 3.5b, the time trace of the reflection at 1150 nm for H_2 concentrations up to 10% is depicted. The initial reflectance (at 37%) undergoes a 1% decrease when applying a hydrogen

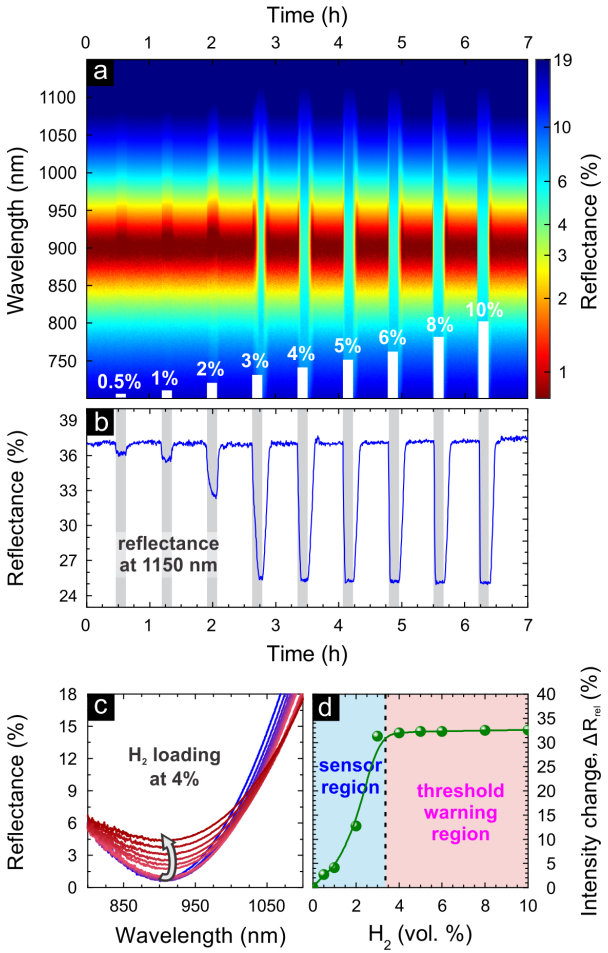

Figure 3.5: Time-resolved spectral response of the palladium based plasmonic perfect absorber sensor during exposure to hydrogen gas. (a) Color-coded plot of time-dependent reflectance spectra for different hydrogen concentrations (white colored bars). (b) Time trace of the reflection of the large-area perfect absorber sensor at 1150 nm for different hydrogen concentrations. (c) Evolution of the reflectance spectra of the plasmonic perfect absorber during 4 vol% H_2 loading. The minimum reflectance initially red-shifts (Pd in α-phase) and then shifts into the blue with strongly increasing reflectance and broadening of the spectra, when Pd transforms into the β-phase. (d) Relative intensity change of the perfect absorber at different hydrogen concentrations splitting the functionality of the sample into a quantitative sensor region (blue area) and a threshold warning region for hydrogen concentrations of 3% or more (red area).

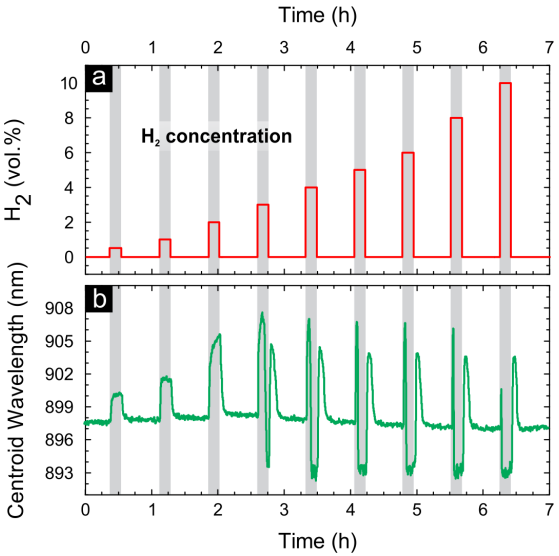

Figure 3.6: Optical response of the palladium based plasmonic perfect absorber sensor during exposure to different hydrogen concentrations in nitrogen carrier gas. (a) The hydrogen cycling condition is identical for all experiments. The sample is exposed to different hydrogen levels for 600 seconds and to 100% N2 for 2000 seconds after each hydrogen step. (b) Centroid wavelength of the large-area perfect absorber sensor for different hydrogen concentrations. The minimum reflectance initially red-shifts (Pd in α-phase) and then shifts into the blue with strongly increasing reflectance and broadening of the spectra, when Pd transforms into the β-phase.

concentration of 0.5 vol.% H_2 in N_2 and is further reduced when higher hydrogen concentrations are applied. When exposing the sensor to 2 vol.% of H_2, a pronounced and slow change of the reflectance is observed, which can be understood by considering the hydrogen-induced phase-transition in palladium. In the case of palladium nanoparticles, this transition between α and β-phase starts to occur at hydrogen partial pressures of about 20 mbar (2 vol.% H_2 at atmospheric pressure) at room temper-

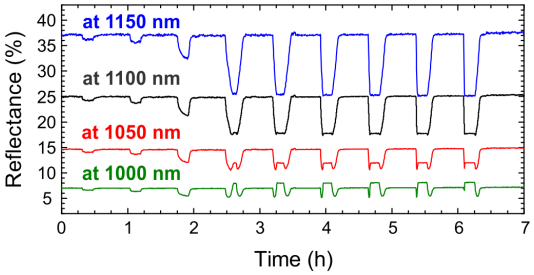

Figure 3.7: Time trace of the reflection of the large-area perfect absorber sensor for different hydrogen concentrations at different wavelengths. The changes in reflection become smoother when increasing the wavelength.

ature [140, 144]. Through exposure to higher hydrogen partial pressures, the palladium patches are fully transformed into the β-phase, resulting in a quasi-saturation of the sensor [145, 146]. The same measurement is carried out for the sample in Figure 3.4a, showing a similar behavior (Figure 3.8). The stability of the sensor device over multiple gas exposure cycles is confirmed by carrying out a second measurement on the same sample (see Figure 3.8).

Full reflectance spectra illustrating the evolution of the optical response during this hydrogen loading cycle are displayed in Figure 3.5c. When the H_2 loading starts, the Pd is first transformed into PdH_x in the α-phase with $x>0.2$. This phase has different optical properties than pure Pd but almost no effect on the lattice spacing between the palladium atoms [147], resulting in a small modification of the perfect absorber's optical response (red-shift of the minimum reflectance). Exposure to higher H_2 partial pressures leads to a phase change into the PdH_x β-phase ($x\cong0.7$), which is accompanied by a drastic change in nanoantenna volume of up to 12% [148] in addition to a change in the electronic and, therefore, dielectric properties. The expansion

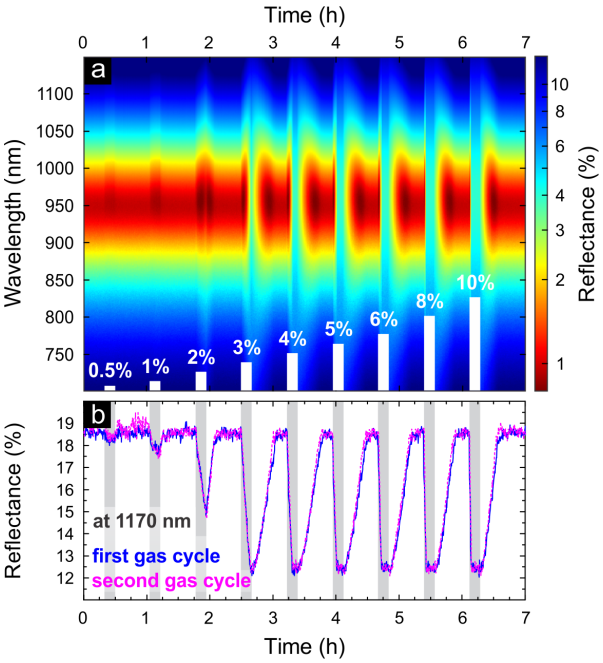

Figure 3.8: Time-resolved optical response of the palladium based plasmonic perfect absorber sensor with minimum reflection at 950 nm during exposure to hydrogen. (a) The color-coded plot of the time-dependent reflectance spectra for different hydrogen concentrations (white colored bars). The sample is exposed to different hydrogen concentrations for 600 seconds and to pure nitrogen for 2000 seconds after each hydrogen step. (b) Reflection of the large-area perfect absorber sensor for different hydrogen concentrations at 1170 nm. A second measurement of the same sample is shown as dashed pink line. The small changes between the first and second sensing cycle are due to structural changes in the palladium squares.

seems to be dominated by a growth in the direction perpendicular to the surface due the excellent adhesion of Pd to the MgF_2 spacer layer. This thickness increase of the nanoantennas leads to an overall blue-shift of the resonance [144].

Figure 3.5d shows the equilibrium intensity changes of the perfect absorber device at 1150 nm for different H_2 concentrations. The minimum reflectance was extracted at each H_2 concentration step right before the subsequent unloading process. At H_2 concentrations below 3.5 vol.%, a near-linear relation between the relative intensity changes and the applied hydrogen concentration is observed. Therefore, in this concentration range, the system can be operated as a quantitative sensor for hydrogen in the environment (blue area). At higher concentrations, the amplitude stays mostly constant and the system can still be utilized as a threshold warning device (red area).
The fabricated plasmonic perfect absorber sensor can be optimized for special applications where the fast response or maximum wavelength shift to H_2 exposure is required by using other novel materials such as yttrium, magnesium, and titanium dioxide (TiO_2) [134, 135, 149] or by using direct contact palladium-gold nanostructures [150].
In summary, laser interference lithography was utilized to fabricate large-area palladium wire and square nanoantenna arrays with excellent homogeneity to realize plasmonic perfect absorber sensors in the visible- and near-infrared wavelength ranges. The fabricated perfect absorbers provide near zero reflection at specific design wavelengths, which translates to almost 100% absorption of light. The working wavelength of the perfect absorber can be tuned over a wide range, as demonstrated by different fabricated samples as well as extensive scattering matrix simulations. Additionally, the optical response of the large-area sensor in the presence of hydrogen was measured and relative intensity changes of up to 400% at hydrogen concentrations of above 3 vol.% in N_2 was observed. The simplicity and versatility of the large-area and low-cost fabrication process will enable the

further development of perfect absorber sensors into a fascinating tool for the optical detection of small amounts of hydrogen or other trace gases in a multitude of industrial applications.

4

LARGE-AREA ANTENNA-ASSISTED SEIRA SUBSTRATES BY LASER INTERFERENCE LITHOGRAPHY

Surface-enhanced infrared spectroscopy (SEIRA) requires resonant plasmonic antennas, which enable material-specific detection of minute amounts of analytes. This allows for a broad range of applications in life sciences, medical diagnostics, and environmental as well as industrial monitoring of harmful or toxic substances. However, to match the high SEIRA sensitivity with real-world applications, a fast and low-cost fabrication of homogenous antenna arrays over cm^2 areas is essential. This requirement is still lacking a practical solution.

In this chapter, for the first time laser interference lithography is introduced for the fabrication of tailored SEIRA substrates. Up to now, there have been published several methods that suffer either from relative low sensitivity, i.e., randomly arranged metal films, or from small areas, when using electron beam lithography. laser interference lithography, however, combines the advantages of both approaches in a unique way and thus allows for the fast and homogeneous preparation of metal antennas featuring easily tunable resonances in the infrared spectral range over square centimeter.

In order to demonstrate the SEIRA activity of the resonant antenna substrates prepared by laser interference lithography, they are covered with different molecular layers of 3 and 30 nm thickness. As a result, sensitivities that were comparable to other

SEIRA studies are found. These sensitivities were orders of magnitudes larger when compared to conventional IR spectroscopy. Furthermore, it was possible to use this method in real time to in-situ monitor the ultraviolet-degradation of the 30 nm thick polymer film with an increased sensitivity and without modifying the degradation process itself.
These findings are of high interest for the researchers in the field of nanofabrication and plasmonics as well as for users of surface-enhanced infrared spectroscopy.
*In this chapter, laser interference lithography is utilized to fabricate large-area plasmonic antenna substrates for surface enhanced infrared absorption (SEIRA). Changing the interference condition in each exposure process allows to precisely control the geometrical parameters of the structures and thus to specifically tailor their optical response. Independent of the underlying wafer, the technique enables a homogeneous preparation of antennas over cm^2 areas with tunable and high quality plasmonic resonances in the near- and mid-infrared spectral range. The broad applicability of such SEIRA substrates is demonstrated by enhancing the infrared vibrational signals of a monolayer octadecanethiol and by monitoring the ultraviolet degradation of a polymer via the decrease of its specific vibrational modes. Due to the large-area and fast fabrication process, laser interference lithography is ideally suited for the preparation of low-cost sensing platforms for a variety of different SEIRA applications in the chemical, analytical, and life sciences.

* This Chapter is adapted from S. Bagheri et al., Large-Area Antenna-Assisted SEIRA Substrates by Laser Interference Lithography, *Advanced Optical Materials* 2, 1050-1056 (2014). Reprinted with permission. Copyright 1999-2016 John Wiley & Sons, Inc. All Rights Reserved.

4.1 BASIC PRINCIPLES

Infrared (IR) spectroscopy is a standard tool in life science and medicine for the detection and chemical characterization of molecular species, since it allows for an unambiguous identification based on the specific molecular vibrations. Unfortunately, these molecular vibrations are excited inefficiently with infrared light. Thus, the detection of minute amounts of toxic or harmful [151, 152] substances, which is essential for sensing applications, is hampered. One way to overcome this limitation is the use of specially designed metal structures, known as resonant plasmonic antennas. Such structures concentrate electromagnetic radiation in nanometer-sized volumes and therefore provide huge near-field enhancements (see Figure 4.1a and Ref. [153]). Molecular vibrations of species located in these hot spots can be enhanced up to five orders in comparison to conventional infrared spectroscopy [95, 154, 155].

Although, several studies [67, 153], discussed near-field distributions of resonantly excited nanoantennas intensively, However, a near-field map of the fabricated nanoantenna is helpful to get an idea about the intensity distribution and the SEIRA enhancement factors. Therefore, the numerically calculated near-field intensity distribution of a resonantly excited ellipsoidal antenna is shown in Figure 4.1a.

The near-field intensity distribution was calculated by numerically solving Maxwell's equations under normal incidence of infrared radiation polarized parallel to the long antenna axis using the commercial finite-difference time-domain (FDTD) software Lumerical FDTD-Solutions v8.5.3. Based on the fabricated structures the gold antenna was modeled as a vertical extrusion (height 35 nm) of an oval with length L = 1 μm, width

W = 0.5 µm placed on a calciumdifluoride (CaF_2). The substrate was described by a dispersionless refractive index of n = 1.41 and the optical data of gold was taken from Palik [156]. The antenna was situated at least one wavelength size away from the perfect matched layers (PMLs) that describe the boundary conditions of the simulation volume. In order to reduce computational resources the total field scattered field (TFSF) approach and subgridding techniques were chosen. Typical mesh sizes of 2 nm were used in the vicinity of the antenna and mesh sizes smaller than 100 nm elsewhere. A plane wave from a broadband source (2000 to 5000 cm^{-1}) excited the structure. The electromagnetic field intensities were recorded with a 2D field profile monitor placed parallel to the substrate at half height of the structure at the resonance frequency (ω_{res} = 3380 cm^{-1}). Convergence testing was performed by iteratively reducing mesh sizes and increasing the number of PMLs, simulations times, and the simulation volume.

Several studies following this approach of antenna-assisted surface enhanced infrared absorption (SEIRA) utilize small-area samples fabricated by cost-intensive and time-consuming electron-beam lithography [154, 157–159]. To transfer the high sensitivity enabled by antenna assisted SEIRA to life science laboratories and to allow for a broad range of sensing applications a fast, large-area and low-cost fabrication is required. Ideally, one would like to have low-cost and cm^2 sized chips, which provide plasmonic resonance over the whole area and can be simply put into standard infrared spectrometers, serving as smart substrates for the detection and identification of biological or chemical substances. Randomly distributed metal island films [6, 7] or metal stripe gratings [160] enable such large-area fabrication, but their plasmonic enhancement is orders of magni-

tudes smaller than the one of tailored nanoantennas. In contrast, metal antennas prepared by bottom-up approaches, such as nanosphere lithography [8–10], offer higher enhancements but suffer from inhomogeneity on large scales. Recently, colloidal hole mask lithography [11, 12] has been introduced as an approach to fabricate tailored nanostructures that provide high near-field enhancements. However, due to intrinsic limitations of the method, only randomly distributed antennas can be realized. Other methods, like nanoimprint techniques, have their own limitation such as a slow fabrication process of mask [14–16]. In contrast laser interference lithography enables a fast preparation of tailored polymer and metal structures arranged in well-defined geometries on large scales up to 4 inches [161], with a high structure density [162]. These characteristics make laser interference lithography a powerful tool for the fabrication of plasmonic materials with a broad range of applications, for example, plasmonic color filtering [163] or biosensing [164, 165]. Also, the fabrication of substrates for antenna-assisted SEIRA is enabled by this flexible approach as will be demonstrated in this chapter.

In particular, the potential of laser interference lithography as a powerful tool for the fast and low-cost preparation of homogeneous large-area substrates for antenna-assisted SEIRA will be highlighted. More specifically, laser interference lithography is utilized to prepare tailored metal structures featuring high-quality plasmon resonances in the near- and mid-infrared spectral range. These substrates provide excellent SEIRA activity as demonstrated with two different molecular layers attached to the antennas. Furthermore, they enable sensitive in-situ monitoring of the UV degradation of polymers via the signal contrast in their vibrational spectra.

4.2 LASER INTERFERENCE LITHOGRAPHY

The interference of two coherent laser beams with wavelength causes a standing wave grating pattern which can be used for the preparation of tailored structures in photoresists and optionally transferred to metals via etching processes. Tuning the periodicity

$$p = \frac{\lambda}{2 \times \sin(\theta/2)} \tag{4.1}$$

of this grating pattern by changing the angle θ between the two incident beams and adding a second exposure step enables the fabrication of geometrically tunable structures [166]. Here, such a two-exposure process is utilized to fabricate large-area and defect-free plasmonic antenna arrays for antenna-assisted surface-enhanced infrared absorption.

A schematic drawing of the laser interference lithography setup is shown in Figure 4.1b. Two parts of an expanded HeCd laser beam at 325 nm wavelength are selected with movable mirrors and directed towards the sample. The first UV exposure process generates a grating pattern in a photoresist which is spun onto a metal film (in this case gold) on the sample. Subsequently a second grating pattern with different orientation is achieved after rotating the sample (angle φ which is 53 degree here) and exposing the photoresist a second time. Tuning the exposure dose for each step enables us to employ the double-exposed areas as an antenna mask, which can be used for a flexible preparation independent of the underlying wafer. The pattern is then transferred via directional argon ion beam etching into the metal film, resulting in large-area regular arrays of metallic antennas with tunable lengths and widths as well as periodicity.

Prior to the laser interference lithography exposure, the CaF_2

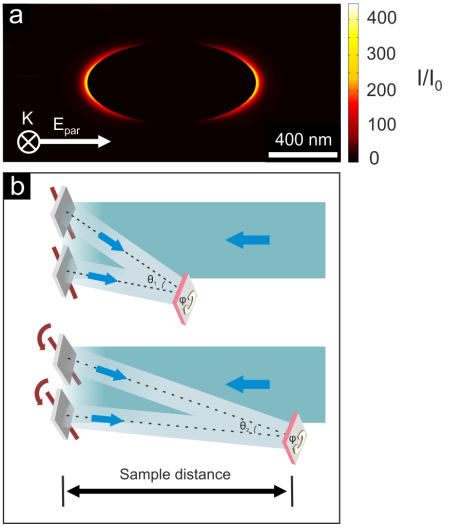

Figure 4.1: (a) Numerically calculated electromagnetic near-field intensity I/I_0 (18 nm above the CaF_2 substrate, parallel polarization) of an ellipsoidally shaped antenna (length L =1.0 µm, width W = 0.5 µm, and height H = 35 nm) resonant at 3380 cm^{-1}. The electromagnetic near-field intensity is concentrated in hot spots at the antenna tip ends. (b) Schematic view of the laser interference lithography set up: The expanded laser beam (blue-green) is directed by two mirrors to the gold and photoresist-covered wafer. This wafer is rotated by an angle φ (here 53 degree) for a second exposure process in order to obtain 2D periodic structures. Antennas with various geometrical parameters (length, width and distance between antennas) are produced by changing the interference angle θ. This is realized by moving the sample holder in direction of the expanded laser beam, thus changing the sample distance, and controlling the direction of the reflected light (sky blue) by tuning the mirrors.

and glass wafers are cleaned with acetone and iso-propanol for 10 minutes in an ultrasonic bath and subsequently dried them with nitrogen. After that a 2 nm thick chromium (adhesion layer) followed by 35 nm thick gold layer (Pfeiffer Vacuum Model PLS-500, 10^{-7} mbar) is evaporated onto the wafer and spin-coated a

90 nm thick photoresist (ma-N 405) film [167] on top of the Au layer.

For the subsequent UV exposure a HeCd laser (Kimmon Electric Co, λ = 325 nm, 14 mW) is used as a light source and achieved an expanded Gaussian laser beam using a UV objective lens (Carl Zeiss, 10-fold magnification, NA = 0.2) and a 5 µm pinhole. The samples were placed between 185 and 215 cm behind the pinhole. Typical UV exposure doses were between 0.8 and 2 mJ/cm² with typical exposure times between 25 and 45 seconds. After the exposure the samples are immersed in a developer (AZ826, development time between 25 and 40 seconds), distilled water for 60 seconds and are dried using nitrogen. Then the areas covered with the developed photoresist were transferred into the gold layer via an argon ion beam etching process (Technics Plasma Model R.I.B.-Etch 160, etching time 90 seconds) resulting in the gold structures of desired shape and size. Finally, the remaining photoresist was removed using acetone and isopropanol. These steps are shown in 4.2 (a-f).

As a result of the sample fabrication process, highly homogenous antenna substrates on large scales (10×10 mm²) are obtained as shown in the photograph (Figure 4.3a) and the scanning electron microscopy (SEM) image (Figure 4.3b). This finding is also supported by the infrared optical properties of the antenna substrates.

Infrared spectroscopy was performed using a Bruker Hyperion microscope (15-fold magnification, NA = 0.4) coupled to a Bruker Vertex 80 spectrometer, allowing for laterally resolved measurements on the micrometer-scale. Typical infrared spectra were recorded in parallel and perpendicular polarization with at least 25 scans and a resolution of 2 cm^{-1}. Typical infrared transmittance spectra recorded at various positions of such a sample

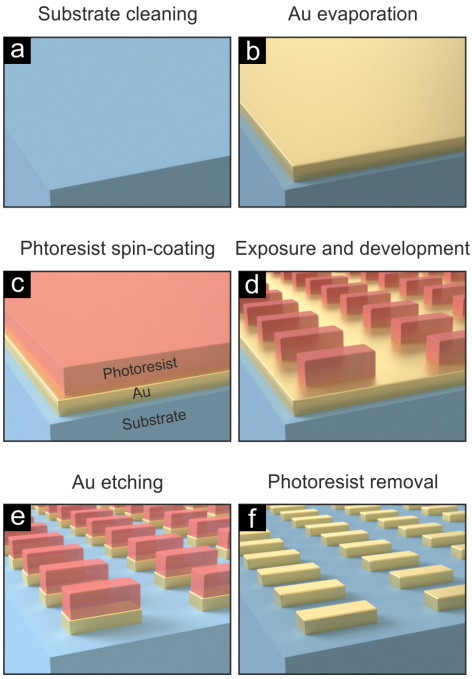

Figure 4.2: Schematic drawing of the fabrication process of Au nanoantennas: (a) Substrates are cleaned with acetone as well as iso-propanol (b) Au films are are evaporated on a substrate. (c) Subsequently, the photoresist is spin-coated on top. (d) Exposure and development processes create the antennas mask in the polymer, which is transferred to (e) Au via argon ion beam dry etching. (f) The photoresisti is removed by using acetone and iso-propanol.

feature plasmonic antenna resonances with frequencies and extinction varying by less than 3% (Figure 4.3c). This excellent homogeneity of the large-area antenna substrates enables routine measurements with cm-sized apertures in simple standard FTIR spectrometers as they are present in many life sciences, chemistry and pharmacy laboratories. For a demonstration, the transmittance of an antenna substrate (L = 1.8 μm and W = 0.8 μm)

with a simple FTIR spectrometer (Bruker Alpha) and a high-end FTIR spectrometer combined with an IR microscope is acquired. As expected a good agreement is found (see Figure 4.4).

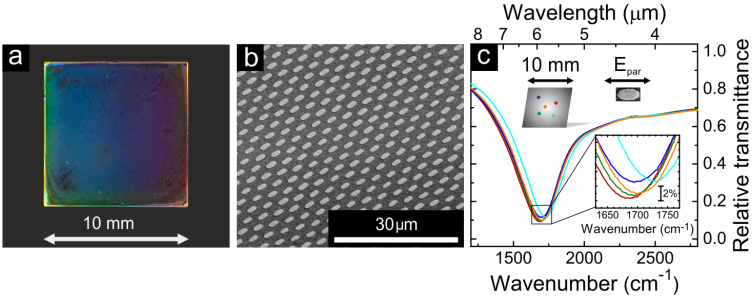

Figure 4.3: (a) The photograph and (b) the scanning electron micrograph (tilted view) of gold antennas (length: 2.1 µm, width: 1 µm, height: 35 nm) demonstrate the excellent homogeneity of the fabricated substrates on a large scale. (c) The homogeneity is further confirmed by infrared transmittance measurement (parallel polarization, E_{par}) recorded at different positions of the antenna substrate.

It is a well-known fact that the resonance frequencies of metal particles are tunable by their geometrical dimensions [95, 168]. In laser interference lithography technique, these geometrical parameters, such as length (L), width (W), and distance between the antennas cannot be chosen completely independently and are linked via simple geometrical relations:

$$L = \frac{\Delta a(p)}{2\sin(\varphi/2)} \tag{4.2}$$

$$W = \frac{\Delta a(p)}{2\cos(\varphi/2)} \tag{4.3}$$

As mentioned before the rotation angle is given by φ and the photoresist linewidth by Δa, depending on the periodicity p. According to these equations and equation 4.1 one can, for example, adjust the periodicity by changing the interference angle θ

for a constant ratio of length and width. Additionally one is able to the control the antenna geometry by using different exposure doses or different development times of the photoresist. Larger antennas are fabricated with a higher exposure dose or shorter development time, whereas smaller antennas are produced with lower exposure dose or longer development time. These parameter variations enable us to prepare micro- and submicrometer-sized structures in different geometries on a large scale with plasmon resonances in the near- and mid-infrared spectral range.

4.3 MEASUREMENT OVER LARGE-AREA

FTIR-spectroscopy is a standard characterization technique used in chemistry, life sciences and pharmacy. An FTIR spectrometer (Bruker Vertex 80) combined with a Hyperion microscope for laterally resolved infrared spectroscopy with micrometer-sized apertures is chosen to check the homogeneity of the sample (Figure 4.3c). However, one also could just use a simple FTIR spectrometer without a microscope with aperture sizes in the cm range. Such measurement is shown in the Figure 4.4.
Both, the spectrum acquired with an expensive FTIR setup including an infrared microscope (spot size 0.01 mm^2, blue curve) and the spectrum recorded with a cheaper standard FTIR spectrometer (Bruker alpha, 63 mm^2 spot size, black curve), show the fundamental antenna resonance at around 2100 cm^{-1}. This plasmon resonance can be excited with infrared radiation polarized along the long wire axis. The differences between both spectra are mainly caused by different illumination geometries in the respective setup. Unfortunately, there are no simple infrared spectrometers that work out to the 3-6 μm range, where

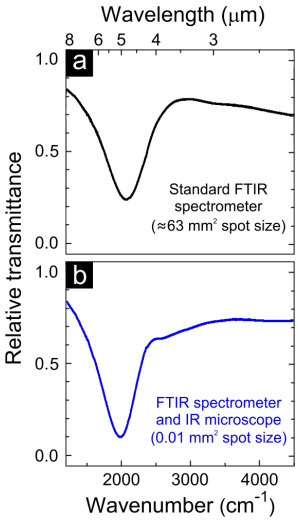

Figure 4.4: Relative transmittance of an antenna array with L = 1.8 μm and w = 0.8 μm measured in parallel polarization. (a) The blue black curve represents a spectrum acquired with a standard FTIR spectrometer whereas (b) the blue curve was recorded with an expensive infrared microscope combined with a high-end FTIR spectrometer. The spectral differences are mainly due to different illumination geometries in the respective experiment.

vibration fingerprints can be found. The inexpensive Ocean Optics spectrometers that work in the near IR range already cost about 20 kEUR. A brand new Yokogawa grating spectrometer up to 3 μm (no FTIR) sells for about 100 kEUR. Hence a low-cost lab FTIR as found in many chemical labs for about 20 kEUR as the Perkin-Elmer used above is exactly what can be considered cheap lab equipment. Furthermore, the aim is to produce large-area low-cost substrates to enable SEIRA detection in the mid-IR using such low-cost spectrometers which have usually apertures in the range of 1 to 10 mm.

4.4 TUNABILITY OF THE PLASMONIC RESPONSE

To demonstrate the capability of the method to precisely control the geometrical parameters of metal antennas and consequently the tuning of their plasmon resonances, SEM images and typical relative transmittance spectra of five different antenna substrates are shown in Figure 4.5.
The lengths (L) and widths (W) of the antennas vary from 2.1 to 0.8 μm and 1 to 0.4 μm, respectively, resulting in tunable plasmon resonances in the near- and mid-infrared spectral range (2.5 to 6.2 μm) with modulation depths up to 90% for parallel polarization independent of the underlying wafer (Figure 4.5a). On the contrary, plasmon resonances measured with perpendicularly polarized light (Figure 4.5b) are less intense and much broader, mainly resulting from smaller dipole moments [67]. Beside the fundamental resonance a variety of resonant modes are observed for both polarizations. Some of them have their origin in higher order excitations [169]; others are due to collective modes [170]. Such Rayleigh anomalies stem from the coupling of densely packed and periodically arranged metal structures [171] with distances in the range of the resonant wavelength as present. This coupling behavior combined with the low aspect ratio of the antennas causes a non-linear dependency of the infrared resonant wavelength on the antenna length in contrast to single nanoantennas with high aspect ratio [172].
As mentioned above the laser interference lithography setup has been designed especially for a precise control of the antenna parameters in order to achieve large tunability of plasmon resonances in the near- and mid- infrared independent of the underlying wafer (Figure 4.5). For example, silicon as underlying wafer is also feasible, however it will reduce the SEIRA enhance-

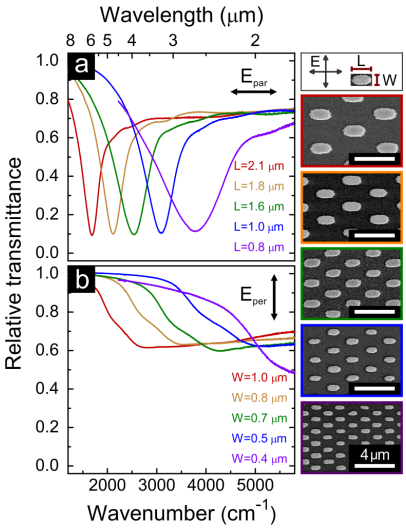

Figure 4.5: SEM images and typical relative transmittance spectra of gold antenna arrays prepared by laser interference lithography featuring tunable IR plasmonic resonances for (a) parallel (E_{par}) and (b) perpendicular (E_{per}) polarization (see upper right panel). The antennas are placed on CaF_2 (red, orange, green and blue) and glass wafers (violet). Lengths (L) and corresponding standard deviations are (2.1 ± 0.04) μm, (1.8 ± 0.02) μm, (1.6 ± 0.04) μm, (1 ± 0.04) μm, (0.8 ± 0.02) μm. Widths (W) of the antennas and corresponding standard deviations are (1 ± 0.02) μm, (0.8 ± 0.02) μm, (0.7 ± 0.02) μm, (0.5 ± 0.02) μm, (0.4 ± 0.03) μm. The height of antennas is 35 nm and their distances are different for each sample due to the fabrication process. The error in height results from the evaporation process whereas the deviations in length and width of the antennas are mainly caused by the photoresist. Typical angles θ range from 4 to 16 degrees.

ment due to its higher refractive index [9]. One can easily extend the spectral range to lower or higher energies by changing the interference conditions. For instance, smaller interference angles θ will enable the fabrication of larger antennas with plasmon resonances located at larger wavelengths. In contrast to that, us-

ing the maximum interference angle (θ = 90 degree) will allow for a preparation of nanometer-sized antennas (L = 100 nm and W = 50 nm), with particle plasmon resonances in visible spectral range.

4.5 ANTENNA-ASSISTED SURFACE-ENHANCED INFRARED ABSORPTION

The large tunability range, high modulation depths, and a homogeneous sample preparation make the antenna substrates ideally suited for sensing applications based on surface-enhanced infrared absorption. The only precondition for SEIRA, however, is a good overlap between the plasmonic excitation of the antennas and the molecular vibration. Consequently, tailored antenna arrays are required which can be easily prepared with laser interference lithography as shown in Figure 4.5a. In order to demonstrate the SEIRA activity of the large-area substrates, two different samples with an octadecanethiol (ODT) monolayer and a 30 nm thick photoresist film are covered, respectively. ODT [173] has been introduced before as a self-assembled monolayer on gold surfaces in SEIRA experiments [95].
Since the adsorption requires a clean gold surface, before the adsorption of octadecanethiol (ODT, Sigma Aldrich, 95 %) the antenna substrates are cleaned using oxygen plasma (Diener electronic Plasma-Surface-Technology, 25 min, 1.3 mbar, 160 W) in order to remove any residues from the fabrication process. Subsequently the samples were immersed into a 1 mM ODT solution in pure ethanol for at least 48 hours. During that time a monolayer of ODT covalently bound to the gold surface. Afterwards the samples are rinsed by ethanol several times to remove unbound ODT molecules and any other contaminations.

A typical relative transmittance spectrum of antennas covered with ODT is shown in Figure 4.6a. The plasmonic resonance frequency is tailored to the symmetric and asymmetric CH_2 vibrations of the ODT molecules for light polarized parallel to the long wire axis. Additionally, for perpendicular polarization, enhanced ODT vibrational bands are found.

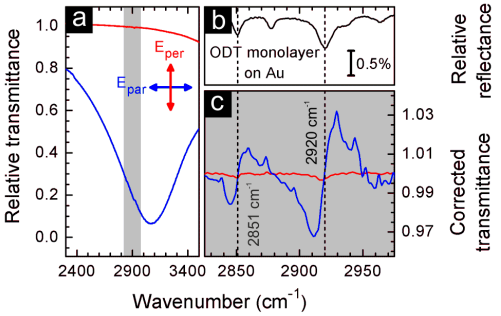

Figure 4.6: (a) Typical relative IR transmittance spectrum of antennas covered with a monolayer of ODT measured with parallel, E_{par} (blue), and perpendicular, E_{per} (red), polarized light. For parallel polarization the plasmonic resonance is tuned to the ODT vibrational bands to obtain highest enhancement. (b) IR reflection absorption measurements of one monolayer ODT adsorbed on a flat gold wafer. (c) Zoom to the baseline corrected transmittance showing the ODT vibration modes (2851 cm^{-1} and 2920 cm^{-1}, dashed lines) for parallel and perpendicular polarizations. Due to the better resonance match, a higher enhancement is observed for the parallel polarization.

To quantitatively evaluate the vibrational signal enhancement, the baseline correction introduced by Eilers [174] is performed. This algorithm allows us to remove any spectral features caused by the antenna and thus provides the undisturbed line shape of the enhanced signal (see Figure 4.6c). As know from other studies [95, 155, 175] and clearly seen in the measurements, the enhanced vibrational signals exhibit a characteristano-type be-

havior resulting from the coupling of the plasmonic and vibrational excitation. The detailed shape of the vibrational band, in this case is asymmetric structure, is given by the phase between the plasmonic and the vibrational excitation and changes with the spectral position of the resonance relative to the vibrational band [176, 177]. It is worth mentioning that also for perpendicular polarization a significant vibrational signal, defined as the difference between minimum and maximum (0.3% for asymmetric and 0.2% for symmetric CH_2-stretching modes of ODT), is observed. However, it is much smaller due to the worse resonance match in comparison to parallel polarization, where values of 6.4% and 2.8%, are extracted respectively. Furthermore even for a similar match, one has to expect less signal enhancement due to the lower dipole strength of the antenna modes excited along the antenna short axis [67].

Infrared reflection absorption spectroscopy (IRRAS) of an ODT monolayer on a gold layer (Figure 4.6b) is used to estimate an enhancement factor. Based on Fresnel's equations for a three-layer system, the measured reflection change is converted to an IR transmission change (I_{calc} = 0.0087% for the asymmetric CH_2 and 0.0035% for the symmetric CH_2 stretching vibration) [95] and compared to the enhanced transmission signal (I_{SEIRA} = 6.4% for the asymmetric CH_2 and 2.8% for the symmetric CH_2 mode) obtained from SEIRA studies. Furthermore, the relative fractions of illuminated spot areas in IRRAS and SEIRA geometry need to be considered. Whereas in IRRAS the IR signal stems from the whole illuminated layer, in SEIRA only a small fraction of molecules actively contribute to the enhanced vibrational signal. These molecules are located in the highly confined near-field around the tip ends (see Figure 4.1a).

Indeed, the estimated enhancement factor strongly depends on

the active area. Since the SEIRA signal is proportional to the enhanced electromagnetic near-field intensity, enhancement from the hot spots of the antennas is expected . As seen in the near-field intensity distribution, which is shown in Figure 4.1a), the near-field intensity is highly confined on the nanometer scale around the antenna tips. Recently this distribution was experimentally confirmed with SEIRA studies [178, 179]. For example, Dregely et al. varied the position of molecular patches along the antenna with nanometer precision and recorded the SEIRA signal. The authors found, that the signal enhancement vanishes rapidly if the patch is place more than 200 nm placed away from the tip end. These experiments and the numerical simulations indicate that the tip ends should be taken as active areas as suggested in Ref. [67].

Indisputable, the active area is difficult to define as it varies with lengths, widths and shape of the antennas. Due to that reason, the approach given in D'Andrea et al. is employed even though the shape of the antenna is different. This approximation seems sufficient to estimate the order of magnitude of enhancement and to ensure the compatibility with other studies.

For the estimation of an enhancement factor, the two end faces of the nanoantenna as SEIRA active areas, i.e. $2\times500\times35$ nm^2 are taken. This approximation was also suggested by D'Andrea et al. [67]. Considering these effects, enhancement factors up to 72000 are estimated for antennas resonantly tuned to the ODT vibrations. In contrast to that, enhancement factors up to 1500 are obtained if the entire antenna surface is considered to be SEIRA active. These factors are one order of magnitude lower than values reported for nanometer-sized antennas [95, 154]. These differences are attributed to the relatively low aspect ratio of the antennas resulting in less confined electromagnetic near-fields.

Furthermore, strong interaction between the structures may lead to a suppression of the enhanced vibrational signals as discussed in Ref. [180].
Our antenna substrates fabricated by laser interference lithography can not only be used for the detection of minute amounts of analytes but also for in-situ monitoring of dynamic processes such as the UV degradation of polymers as will be demonstrate in the following. Therefore, the sample is spin-coated with a positive photoresist (XARP 3100/10, All Resist) and monitored its UV degradation via the decrease of a selected vibrational band (2110 cm^{-1}) when illuminating the polymer-covered sample with UV light (λ = 320-390 nm).
In order to achieve the maximum signal enhancement antennas with spectrally tailored resonances close to the XARP vibration are prepared and covered with a 30 nm thick layer of XARP. Please note that due to the spin-coating process no uniform XARP coverage of the antennas was achieved. In order to obtain more information on the coverage several SEM images were recorded. In the Figure 4.7 a typical SEM image is displayed. Please note that in the upper part of the image the XARP layer was removed by scratching softly over the sample, whereas in the lower part the XARP layer is still intact. Obviously, the area between the antennas is completely covered with XARP. The antennas themselves are still covered but still visible in the XARP covered lower part.
In order to achieve a more uniform coverage evaporation techniques need to be employed. But even the evaporation of molecules do not provide a perfect homogeneous coverage of the antenna, due to the diffusion and absorption properties of the respective molecules on the antennas or substrate [181]. In addition, evaporation techniques are not practicable for real applica-

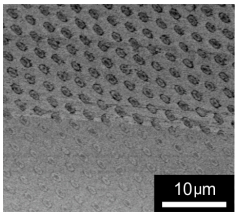

Figure 4.7: Typical SEM image of XARP-covered antenna array. Please note that in the upper part of the image the XARP layer was removed by scratching softly over the sample

tion in chemistry of life sciences. Of course, structures covered with thicker layers do not suffer from inhomogeneous coverage, but here the SEIRA signal is vanishing due to the rapidly decaying fields as for example shown in Ref. [181]. Based on these reasons we decided to spin-coat the XARP molecules, which can also easily be done with other substances in possible applications. Furthermore, a layer thickness of 30 nm is chosen, since here the SEIRA enhancement is still presented. Also infrared transmittance measurements are performed (Figure 4.8a) and as expected an increased vibration signature is observed, which is a superposition of two vibrational signals originating from different sample areas. One part originates from the coupling with the antennas and features the characteristic asymmetric Fano-type line shape, while the other fraction stems from molecules located outside of the enhanced plasmonic near-fields, i.e., the area between the antennas. Since only the enhanced vibrational signal is interested, one should calculate the ratio of the spectrum measured with parallel (perpendicular) polarized light and the reference spectrum of XARP deposited on an unstructured CaF_2 wafer to obtain purely the antenna-enhanced XARP vibrational signal (Figure 4.8b).

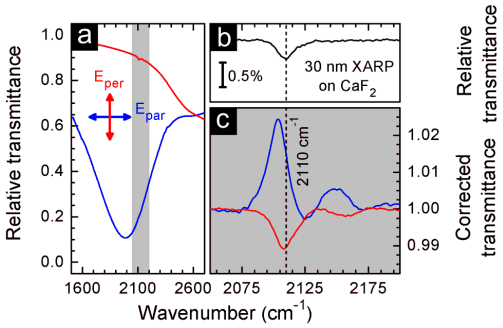

Figure 4.8: Antenna-assisted SEIRA of the spin-coated polymer XARP using large-area plasmonic substrates. (a) Typical relative IR transmittance spectrum of antennas covered with 30 nm of XARP for parallel, E_{par} (blue), and perpendicular, E_{per} (red), polarization. To achieve the highest enhancement the plasmonic resonance is tuned to the polymer vibration mode. (b) Relative IR transmittance spectra of 30 nm XARP spin-coated on a CaF_2 wafer. (c) Baseline corrected transmittance (zoom in) of the polymer vibration mode (2110 cm^{-1}, dashed line) for parallel and perpendicular polarizations. Please note that we only consider the most prominent vibrational band at 2110 cm^{-1} and neglect the less intense one at 2134 cm^{-1}. Different near-field enhancements cause different signal enhancements for parallel and perpendicular polarization.

For further analysis the spectrum is baseline corrected and a signals strength of 2.7% for parallel polarization is extracted (Figure 4.8c). This value corresponds to an enhancement factor of about 900 if only the hot spots are taken into account and 20 if the entire antenna surface is considered. Please note that only the most intense vibration at 2110 cm^{-1} is focused and the less intense vibration at 2134 cm^{-1} which shows a very similar behavior is not considered. In contrast to the ODT studies, lower enhancement factors are observed originating from the different deposited layer thicknesses of 30 nm for XARP and 2.8 nm for ODT [173]. The result is in qualitative agreement with recent studies, where the antenna-enhanced signal evolu-

tion with molecular layer thickness was investigated [181]. Due to the rapidly decaying near-fields of resonantly excited antennas, molecules located in the direct vicinity of the antennas are strongly enhanced, while vibrations of molecules located apart do not contribute significantly to the integrated signal, resulting in lower enhancements for thicker molecular layers.

4.6 IN-SITU MONITORING OF POLYMER UV DEGRADATION

The UV induced degradation of the above mentioned XARP polymer layer deposited on a structured and unstructured wafer is in-situ monitored. As previously described, a normalization and subsequent baseline-correction provides the antenna enhanced vibrations for parallel (Figure 4.9a) and perpendicular (not shown) polarization. For this experiments a UV source (DYMAX Blue Wave 50, λ = 320 - 390 nm) with the fiber end placed approximately 3 cm away from the sample is used.
The vibrational signals decrease with UV illumination time due to the decomposition of the polymer. To point out the degradation process in more detail, the signal (difference between minimum and maximum) in dependence of the illumination time is plotted (Figure 4.9b). Obviously, the vibrational signal strengths in both parallel and perpendicular polarizations are enhanced in comparison to reference measurements of the polymer layer spin-coated on an unstructured CaF_2 wafer with the very same thickness (black curve). For example, after 65 seconds of UV illumination, the unenhanced vibrational signal of the polymer is below the noise level and not detectable with conventional infrared spectroscopy. In contrast to that, the enhanced signals are still visible. The slope of the curve, however, is not affected by the antennas, indicating that the confined electromagnetic near-

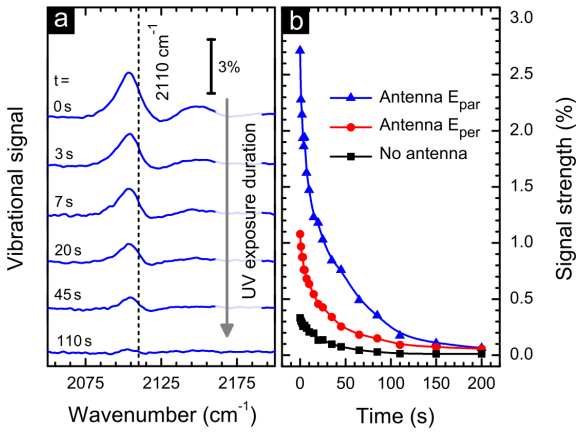

Figure 4.9: UV degradation of the photoresist XARP is monitored via the decrease of the selected vibrational mode at 2110 cm^{-1}. (a) Baseline corrected IR spectra (parallel polarization, E_{par}) show a decrease of the enhanced vibrational signal for different UV exposure times. The dashed line indicates the vibrational mode. (b) Signal strength (difference between minimum and maximum) of the antenna-enhanced vibrational mode as extracted from (a). As references the time traces are also shown for perpendicular polarization (E_{per} red) and a wafer without any antennas (black). The errors of the vibrational signals are smaller than the symbol size.

fields do not influence the degradation behavior. Thus SEIRA can be used as reliable tool to monitor chemical processes with higher sensitivity without influencing the process itself.

In summary, laser interference lithography was employed to fabricate large plasmonic antenna arrays with an excellent homogeneity, featuring high quality plasmons in the near- and mid-infrared spectral range. Depending on the process parameters, the resonances are easily tunable and therefore ideally suited for antenna-assisted surface-enhanced infrared absorption as demonstrated for two molecular substances, namely octadecanethiol and the polymer XARP. The measured differences

in signal enhancement (72000 for octadecanethiol and 900 for the polymer) are related to the rapidly decaying near-fields, since the ODT molecules are directly adsorbed on the antennas whereas the polymer film extends over a range of 30 nm. In comparison to conventional infrared spectroscopy, however, the signal enhancement still provides significant improvement. For example, it was possible to in-situ monitor the UV induced degradation of the XARP polymer with an increased sensitivity via vibrational signal decay without modifying the degradation process itself. These results demonstrate the capability of laser interference lithography to homogeneously fabricate plasmonic antennas on large areas with high quality resonances that can be specifically tailored for various antenna-assisted SEIRA applications.

5

FEMTOSECOND DIRECT LASER WRITING FOR LARGE-AREA FABRICATION OF PLASMONIC NANOANTENNA

Surface-enhanced infrared spectroscopy (SEIRA) requires resonant plasmonic nanoantennas, which enable material-specific detection of minute amounts of analytes. This allows for a broad range of applications in life sciences, medical diagnostics, and environmental as well as industrial monitoring of harmful or toxic substances. However, to match the high SEIRA sensitivity with real-world applications, a fast and homogenous fabrication of arbitrarily shaped and arranged nanoantennas over cm^2 areas is essential. These requirements are still lacking a practical solution.

In this chapter, for the first time two-photon femtosecond direct laser writing combined with argon ion beam etching is introduced for the fabrication of tailored SEIRA substrates. Up to now, there were several methods published that suffer either from relative low sensitivity, i.e., randomly arranged metal films, or from small areas, when using electron beam lithography. Direct laser writing, however, combines the advantages of both approaches in a unique way and thus allows for the fast and homogeneous preparation of arbitrarily shaped and arranged nanostructures featuring easily tunable resonances in the infrared spectral range.

In order to demonstrate the flexibility of the approach with respect to the arrangement of nanostructures, several nanoantenna

arrays having specific antenna spacings are prepared. Enabled by this versatility it was possible to systematically investigate the influence of collective plasmonic excitations originating from periodically arranged nanostructures on the SEIRA enhancement. As a result, strongly modified enhancements for different configurations are observed. For the optimum configuration, close to the Rayleigh anomaly, a maximum SEIRA enhancement factor of about four orders of magnitude is found which is comparable to the SEIRA activity of substrates prepared with previous nanofabrication methods. These findings are of high interest for the researchers in the field of nanofabrication and plasmonics as well as for users of surface-enhanced infrared spectroscopy. *In this chapter, the use of femtosecond direct laser writing lithography is demonstrated for a fast and homogeneous large-area fabrication of plasmonic nanoantennas on a substrate by creating patterned polymer as an etch mask on a metal layer. Subsequent argon ion beam etching provides plasmonic nanoantennas with feature sizes below the diffraction limit of the laser light. They exhibit tunable and high-quality plasmon resonances in the mid-infrared spectral range, which are ideally suited for surface-enhanced infrared absorption (SEIRA). In the present chapter, a reliable, fast, and simple low-cost fabrication of a wide variety of antenna arrays ia demonstrated and the influence of plasmonic coupling between neighboring antennas on the SEIRA enhancement effect is particularly examined. Specifically, the enhanced infrared vibrational bands of a 5 nm thick 4,4′-bis(N-carbazolyl)-1,1′-biphenyl (CBP) layer evaporated on arrays with

* This Chapter is adapted from S. Bagheri and K. Weber et al., Fabrication of Square-Centimeter Plasmonic Nanoantenna Arrays by Femtosecond Direct Laser Writing Lithography: Effects of Collective Excitations on SEIRA Enhancement, *ACS Photonics* 2, 779-786 (2015). Reprinted with permission. Copyright 2015 American Chemical Society.

different longitudinal and transversal spacings between antennas is measured. An optimum SEIRA enhancement per antenna of four orders of magnitude is found close to the collective plasmon excitation in the nanoantenna array, rather than at the highest antenna density. The method establishes a low-cost replacement technique for electron beam lithography. Simple, fast, and straightforward fabrication of optimized SEIRA antenna arrays with cm^2 areas, which can be used in real-world applications such as chemical and biological vibrational sensing, is now possible.

5.1 BASIC PRINCIPLES

Infrared (IR) spectroscopy is a standard technique in chemistry and life science for the unambiguous identification of materials and molecules based on their specific infrared absorption. The main limitation of infrared spectroscopy, however, is the relative low-absorption cross-section of molecular excitations [182]. Recently, special designs of metal structures, known as plasmonic antennas [157–159], are employed to overcome this limitation. Such plasmonic nanoantennas provide huge electromagnetic near fields, which can be used to enhance vibrational signals of any molecules located in such hot spots. Following this approach of surface-enhanced infrared absorption (SEIRA), the sensitivity is increased by up to five orders of magnitude in comparison to conventional infrared transmittance spectroscopy [95].

While large-area fabrication methods are required for practical applications of SEIRA, nanoantennas in the above-mentioned studies are typically prepared by EBL and lift-off techniques. This process allows for precise control of the nanostructure ge-

ometries but hampers direct and maskless large-area fabrication on reasonable timescales. In contrast to that, randomly distributed metal island films [6, 7] can easily be prepared on large scales at low-costs but provide relatively low SEIRA enhancement. Nanostructures fabricated by colloidal mask lithography [9, 11] or laser interference lithography [17] offer a higher enhancement, but only randomly or particularly arranged nanostructure geometries with low aspect ratios are feasible. Some other methods such as nanostencil lithography [15, 16], or direct nanocutting [14] employ a patterned sample as a mask, which needs to be prepared by other techniques, mostly EBL. However, the use of tailored masks allows for a fast nanofabrication on large areas. For example, reconstructable mask lithography proposed by Yang et al. [183] is able to fabricate wafer scale-sized metamaterial with nanoscale dimensions. Recently, photo-induced fabrication methods have been introduced for SEIRA applications, but the tailored nanostructures fabricated by these methods do not provide a sufficient homogeneity and high SEIRA enhancement at the same time. For example, nanospherical lens lithography [10] suffers from inhomogeneities, and metal stripe gratings produced by photolithography offer only moderate enhancement [160].
In contrast to that, direct laser writing (DLW) as a two-photon absorption process allows for a homogeneous and well controlled fabrication of nanostructures [184, 185] over large areas at low-costs.

5.2 DIRECT LASER WRITING LITHOGRAPHY

In this approach, a tightly focused spot of femtosecond laser light causes local polymerization in a polymer and thus enables

the writing of arbitrarily shaped 3D structures, e.g., for perfect absorption [186], telecommunications [187], and optical devices for integrated optics [188–190]. However, the preparation of 2D metal nanostructures is easily feasible via selectively scanning the photoresist interface and subsequent argon ion etching as demonstrated in the following. Besides a homogeneous fabrication of nanostructures on large areas, this versatile nanofabrication technique allows for the preparation of arbitrarily arranged nanoantennas. Thus, systematic studies on the impact of various plasmonic coupling effects on the enhancement in surface-enhanced spectroscopic techniques, such as surface-enhanced Raman spectroscopy (SERS) [191], enhanced fluorescence [192] or SEIRA, are feasible.

Numerous studies during the last decade report on how the optical properties of such specially arranged nanoantennas depend on the interaction with other particles situated in the near [80, 193] or far field [194, 195]. For SEIRA it was demonstrated that nanoantennas with nanometer-sized gaps increase the enhancement by one order of magnitude in comparison to individual antennas [84]. However, also collective plasmonic excitations originating from periodically arranged nanostructures can provide additional SEIRA enhancement [155, 175] if the critical grating periodicity Δ_x and Δ_y fulfill the following equation:

$$\frac{n_s}{\lambda_{collective}} \approx \sqrt{(\frac{i}{\Lambda_x})^2 + (\frac{j}{\Lambda_y})^2} \tag{5.1}$$

Here, n_s denotes the refractive index of the substrate, i and j the diffraction grating orders, and $\lambda_{collective}$ the resonance wavelength of the collective mode. Nanoantennas with resonances tuned to this Rayleigh anomaly [196] strongly enhance the collective plasmonic response, which results in an efficient funnel-

ing of incident light into stronger near field excitations. The effect was first exploited for SEIRA by Adato et al. [155], employing nanoantenna arrays with identical periodicities perpendicular (Δ_y) and parallel (Δ_x) to the long antenna axis, whereas in the present study both periodicities are varied individually.
In this chapter, it will be demonstrated how direct laser writing lithography combined with argon ion etching can be used as a reliable method to prepare homogeneous large-area arrays of plasmonic nanoantennas for vibrational sensing in mid-infrared range. Enabled by the versatility of DLW with respect to the arrangement of nanostructures, nanoantenna arrays with different longitudinal and transversal spacings are fabricated. After the evaporation of the molecular probe named 4,4'-bis(N-carbazolyl)-1,1'-biphenyl (CBP), their SEIRA-activity is measured and then evaluated regarding the optimum configuration for SEIRA.
CaF_2 substrates (refractive index n_s = 1.42) were cleaned with acetone and iso-propanol for 10 minutes in an ultrasonic bath. After drying with nitrogen, 5 nm of Cr as an adhesion layer and a 100 nm thick layer of gold (Pfeiffer Vacuum Model PLS-500, 10^{-7} mbar) as a plasmonic material are evaporated onto the substrate. A drop of photoresist (Nanoscribe IP-Dip), needed for the dip-in direct laser writing process, [197] was then cast on top of the gold surface.
For direct laser writing process, a Photonic Professional GT machine (Nanoscribe GmbH, Germany) with a femtosecond laser beam (λ = 780 nm), which was focused by an objective lens (fold magnification = 63, NA = 1.4) into the photoresist is used.
The tunable laser power at the entrance of the objective was between 5 and 9 mW resulting in different thicknesses (175 to 105 nm) and linewidths (full widths at half maximum between

305 to 245 nm) of the exposed photoresist mask after development. The typical writing speed was 12000 µm/sec, enabling the illumination of a 7.6×7.6 mm²-sized sample within 90 minutes using stitching techniques as described in the following.
After the illumination process, the samples is kept in the developer (Microresist mr-dev 600) for 15 minutes and in isopropanol for 2 minutes to remove the non-illuminated areas. The patterned areas are used as a mask and transferred into the gold layer via an argon ion beam etching process (Technics Plasma Model R.I.B.-Etch 160, beam current range from 90 to 100 mA, typical etching times between 200 to 300 seconds). The etching rates are 0.5 nm/sec for gold, 0.24 nm/sec for CaF_2 and 0.54 nm/sec for the polymer are measured by atomic force microscopy (AFM). Thus the etching ratios of exposed photoresist to gold and to CaF_2 are approximately 1:1 and 2:1 respectively. The remaining polymer was removed using oxygen plasma (Diener electronic Plasma Surface Technology, 90 min, 1.4 mbar, 160 W). As a result, different antenna arrays with typical antenna length and width in the range of 1.7 to 2.8 µm and 105 to 350 nm, respectively are obtained. Also the spacing along the long (d_x) and short (d_y) antenna axis were varied individually. For both directions six different distances (0.5 µm, 1 µm, 2 µm, 5 µm, 8 µm, and 10 µm) were chosen, resulting in 36 different configurations for (d_x, d_y) with five lengths per configuration. The antenna heights were approximately 105 nm. For the initial design, the geometrical parameters were estimated by Fourier modal method simulations [141].
An illustrated drawing of the two photon direct laser writing process is shown in Figure 5.1a. The femtosecond laser light selectively exposes the photoresist, and a photoresist mask is generated via scanning the interface between photoresist and the

gold-coated calciumdifluoride (CaF_2) substrate. After the development process, the exposed photoresist remains on the surface and is used as a mask for argon ion beam etching (Figure 5.1b) enabling the fabrication of gold nanoantennas with well-defined geometrical parameters. In order to prepare large-area samples required for practical applications, the maximum scanning area ($200 \times 200\ \mu m^2$) is subsequently extended by using a positioner stage that moves up to several centimeters.

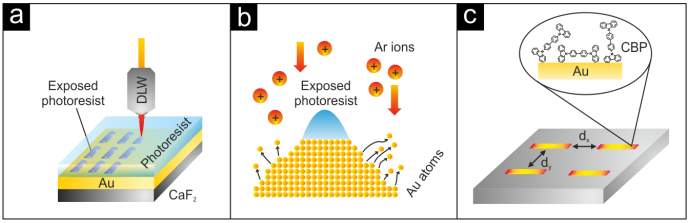

Figure 5.1: Illustration of the nanoantenna fabrication process using femtosecond direct laser writing (DLW) lithography. (a) The laser beam scans the sample and exposes the photoresist at the gold interface selectively. (b) argon (Ar) ion beam etching process: after photoresist development the exposed resist is used as an antenna mask during the etching process. Positive Ar ions are accelerated towards the sample and remove gold atoms from the surface. (c) Antennas with different distances (d_x, d_y) are covered by 5 nm thick 4,4′-bis(N-carbazolyl)-1,1′-biphenyl (CBP) layer to investigate the impact of collective excitations on the signal enhancement in surface-enhanced infrared spectroscopy.

5.3 PLASMONIC RESPONSE OF LARGE-AREA ANTENNA ARRAYS

5.3.1 *Large-Area Fabrication*

Following this approach, homogenous nanoantenna arrays on large areas are fabricated as shown exemplarily in the photo-

graph (Figure 5.2a) and a scanning electron microscope (SEM) image (Figure 5.2b). The photograph was taken with a Canon EOS 60D camera with a Canon EF100 mm f/2.8 Macro USM (f/8, 1/4 sec, ISO 100). The sample was illuminated with a white LED light source. The scanning electron micrographs were acquired with an S-4800 scanning electron microscope (Hitachi Company). Charged areas in the SEM image were removed for a better visualization. The large-area sample is fabricated by stitching 2601 fields next to each other. Each field has a size of 150 × 150 μm^2, hence the antenna array covers 7.6 × 7.6 mm^2. In order to prevent stitching errors the whole area is designed in the way that only small movements of the mechanical stage are necessary and additionally the stage is always moved from one direction to each field. Typical DLW illumination times of such cm^2-sized samples are one order of magnitude smaller than standard EBL exposure times. Their remarkable homogeneity is also confirmed by their infrared optical properties measured at different positions with average distances of about 2 mm (Figure 5.2c and 5.3). IR optical properties were measured using a Bruker Hyperion 2000 IR microscope (Schwarzschild-objective with 15-fold magnification, NA = 0.4) coupled to a Bruker Vertex 80 spectrometer with an optical path purged with nitrogen. To obtain the relative transmittance spectra, the transmittance at the position of the CBP-covered nanoantenna is normalized to an unstructured but CBP-covered area close the nanostructures. Typical spot size is 100 × 100 μm^2 for the SEIRA measurements, allowing the illumination of about 500 antennas for (d_x, d_y) = (1, 5) μm. All spectra were acquired with an IR polarizer (working range 2 to 10 μm) and a liquid-nitrogen-cooled mercury cadmium telluride (MCT) detector with at least 25 scans and a resolution of 2 cm^{-1}. For the acquisition of the non-enhanced CBP spectrum,

an area without nanostructures on the sample and a bare CaF_2 wafer as reference are used. As seen in the inset, the resonance frequencies (transmittance minimum) deviate less than 2 % over the sample, confirming the excellent homogeneity of the nanoantennas on large scales.

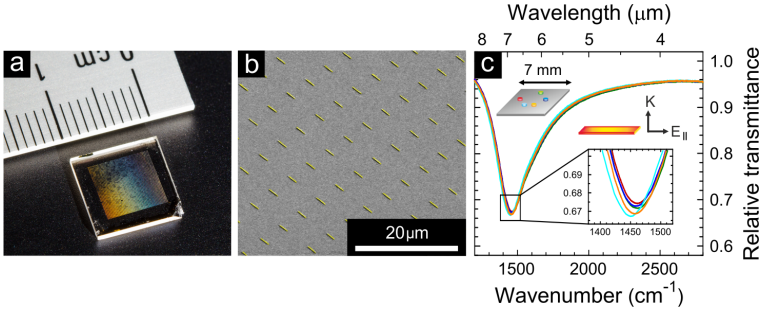

Figure 5.2: (a) The macro photograph demonstrates the fabrication of nanoantennas on cm²-sized areas. (b) The excellent homogeneity representatively shown in the tilted view scanning electron micrograph for antennas (2.4 µm length, 140 nm width, and 105 nm height) arranged in arrays with (d_x, d_y) = (5, 5) µm. (c) The homogeneity is also confirmed by relative transmittance spectra ($E_{||}$, parallel polarization) measured at different positions by infrared microscopic spectroscopy (spot size≈100×100 µm²). Typically, the resonance frequency of the plasmonic excitation deviates less than 2 % as seen in the inset.

5.3.2 *Measurement Over Large-Area*

Although, an FTIR spectrometer (Bruker Vertex 80) combined with a Hyperion microscope are used for laterally resolved infrared spectroscopy with micrometer-sized apertures to check the homogeneity of the sample (Figure 5.2c). However, a simple FTIR spectrometer without a microscope such as the Bruker "Alpha" with aperture size in the cm range can be used to demonstrate the viability. This measurement is shown in the figure 5.3.

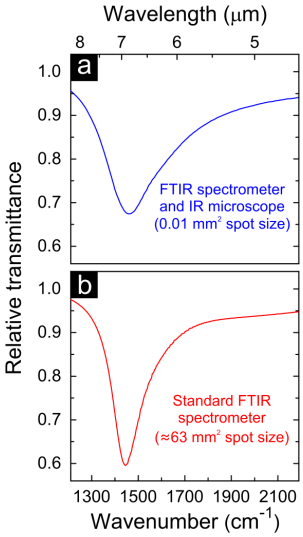

Figure 5.3: Relative transmittance spectrum of a large-area gold antenna array ((d_x, d_y) = (5, 5) μm, L = 2.4 μm and W = 140 nm) measured in parallel polarization. (a) The blue curve was measured with an expensive infrared microscope attached to a high-end FTIR spectrometer whereas the spectrum in (b) the lower panel (red curve) was recorded with a standard FTIR spectrometer (Bruker alpha). The minor spectral differences between both measurements are due to different illumination geometries in the respective setup.

Both, the spectrum acquired with an expensive FTIR setup including an infrared microscope (spot size 0.01 mm², black curve) and the spectrum recorded with a cheaper standard FTIR spectrometer "Bruker alpha" (63 mm² spot size, red curve), show the fundamental antenna resonance at around 1450 cm^{-1}. This plasmon resonance can be excited with infrared radiation polarized along the long wire axis. The differences between both spectra are mainly caused by different illumination geometries in the respective setup.

5.3.3 *Controlling the Feature Size*

Precise tunability of plasmonic properties is desirable for any sensing application but requires full control over their geometry [15]. Direct laser writing combined with argon ion etching offers such versatile control during the fabrication process.

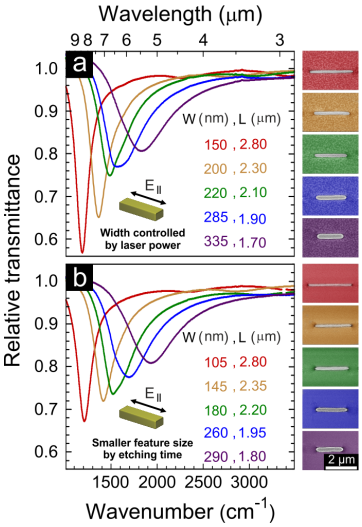

Figure 5.4: SEM images (right) and relative transmittance spectra ($E_{||}$, parallel polarization) of nanoantennas with widths below the diffraction limit of radiation used in the direct laser writing lithography process are shown. The width (W) of each antenna can be defined independently of the length (L) by changing the laser power (a) and further narrowed by increasing the etching time (210 to 255 seconds) (b). Lengths and widths of the antennas are varied from 1.7 to 2.8 μm and 105 to 335 nm, respectively. The laser powers in (a) and (b) are varied from 9 to 5 mW (in steps of 1 mW) resulting in narrower antennas for lower illumination powers. The height of the narrowest antenna is 75 nm, for all other antennas it is approximately 105 nm and the distances between antennas are (d_x, d_y) = (5, 5) μm.

Also, specific illumination times and laser powers in the DLW

process result in different antenna lengths (L) and widths (W), respectively. Keeping the argon ion beam etching time at 210 seconds, for example, but changing the DLW illumination power from 9 to 5 mW (in steps of 1 mW), enables us to prepare nanoantennas with widths changing from 335 to 150 nm. Such nanoantennas with design lengths between 1.7 and 2.8 μm feature tunable plasmon resonances in the mid-IR spectral range as shown in Figure 5.4a.
On the other hand, antenna geometries can be controlled by the argon ion etching process. The widths of antennas can be further narrowed by higher argon etching times, 255 seconds instead of 210 seconds, but same laser powers during direct laser writing. Figure 5.4b shows typical SEM images (selected antenna arrays) and typical relative transmittance spectra of such antennas measured in parallel polarization. Their widths vary from 105 to 290 nm, demonstrating the capability of the approach to prepare antennas with feature sizes below the diffraction limit of the femtosecond laser light. Please note that longer argon etching times slightly decrease the antenna lengths. However, this is only a small absolute change (50 nm) compared to the design length (micrometer range) and thus does not influence the resonance properties significantly.

5.4 ANTENNA-ASSISTED SEIRA

In order to demonstrate the SEIRA activity of the nanoantennas, a homogeneous layer of CBP (thickness 5 nm) on antenna arrays with various lengths and spacings (see Figure 5.1c) is evaporated. 4,4′-bis(N-carbazolyl)-1,1′-biphenyl (CBP, Sigma Aldrich, 99.9%) was evaporated under ultra-high vacuum (HUV) conditions [84]. The homogeneity of the CBP layer is confirmed by relative trans-

mittance spectra measured at five different positions Figure 5.5.

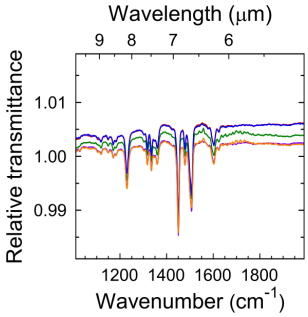

Figure 5.5: The homogeneity of the 5 nm thick CBP layer is confirmed by relative transmittance spectra acquired at five different positions. Typical distances between the measured points were around 1 mm. The IR microscopic spectroscopy was performed using a 100 × 100 μm²-sized aperture.

The slightly varying offset is caused by the reference measurement, which is taken on a bare CaF_2 wafer. An average of the shown spectra was used as a reference to determine the absorption strengths of non-enhanced CBP vibrations. The strengths of 1.3 % for the vibration at 1504 cm^{-1}, 1.7 % for the vibration at 1450 cm^{-1} and 0.8 % for the vibration at 1230 cm^{-1} are found.
Since the optical properties of nanoantenna arrays strongly depend on the plasmonic coupling caused by their periodical arrangement, a similar behavior for their SEIRA enhancement [175, 180] is expected. To independently investigate the effects of longitudinal (parallel to long antenna axis) and transversal (perpendicular to long antenna axis) plasmonic coupling on SEIRA, the spacing along the long antenna axis (d_x) and the short antenna axis (d_y) are varied individually from 0.5 to 10 μm (Figure 5.1c). Additionally, the fabrication of different antenna lengths for each configuration (d_x, d_y) ensures a good match of the plasmonic

resonances and selected CBP vibrations (combined CH deformation and CN stretching mode at 1504 cm^{-1} as well as CH deformation mode at 1230 and 1450 cm^{-1}), which is necessary for an optimum SEIRA enhancement. For this preparation task, DLW combined with argon ion etching is ideally suited, since it provides full flexibility regarding antenna arrangement and geometry on reasonable time scales.

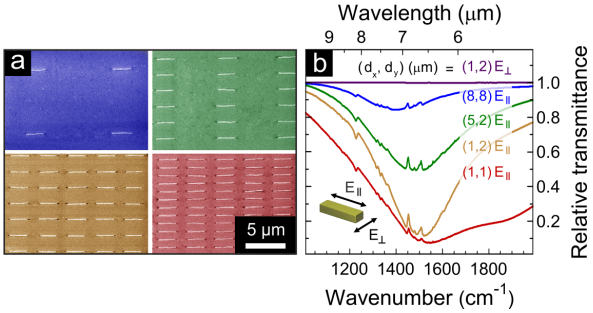

Figure 5.6: (a) Representative SEM images of nanoantennas with selected antenna distances prepared by direct laser writing lithography for the SEIRA studies. (b) Relative transmittance spectra of the corresponding antennas (2.6 µm length, 140 nm width, antenna spacings in µm are indicated by colored numbers in the plot) covered with a 5 nm thick layer of CBP acting as a probe for the SEIRA enhancement. Depending on the antenna distances, different enhancements of the CBP vibrational bands are found for parallel polarization ($E_{||}$), whereas no enhanced signals are found for perpendicular polarization ($E_{\perp}$, purple curve).

Representative SEM images of four selected nanoantenna arrays with similar lengths (L = 2.6 µm) but different spacings (d_x, d_y) and also their corresponding transmission spectra are shown in Figure 5.6. IR measurements in perpendicular polarization (purple curve) do not provide infrared plasmonic resonances, and thus no enhanced CBP vibrations are detected. In contrast to that, broadband plasmonic resonances are excited with parallel

polarized light. Here, the CBP absorption bands are enhanced by the plasmonic near fields. In the spectra, they appear as sharp features on the antenna resonance curve with Fano-type lineshapes originating from the coupling between the plasmonic and the vibrational excitation [95, 176]. As expected, arrays with higher antenna densities mostly show higher signal intensities. However, this correlation does not hold for distances smaller than $(d_x, d_y) = (1, 2)$ µm. For example, although configurations (1, 1) and (1, 2) have the same extinction, the enhanced vibrational signals of configuration (1, 2) are significantly stronger despite the lower antenna density. Consequently, plasmonic interactions between nanoantennas, which considerably change the IR optical properties, must play a significant role in the SEIRA enhancement.

5.5 PLASMONIC COUPLING EXCITATION

In order to investigate this effect, the enhanced vibrational signals from the baseline-corrected transmittance are extracted and normalized to non-enhanced CBP vibrations (see Figure 5.5) as well as to the antenna density given by (d_x, d_y). In more detail, the baseline of the antenna resonance are approximated using an adoption of the computational approach of asymmetric least square smoothing [174] while excluding the spectral regions of the selected vibrational bands. As an example the measured spectra of $(d_x, d_y) = (1, 2)$ µm for different antenna lengths is shown in Figure 5.7a (top panel) and the corresponding baseline corrected signals (bottom panel) obtained by the ratio between the measured transmission spectrum and the fitted baseline.
The vibrational signals of the baseline corrected spectra exhibit a typical asymmetric Fano shape [95, 176]. As seen in the upper

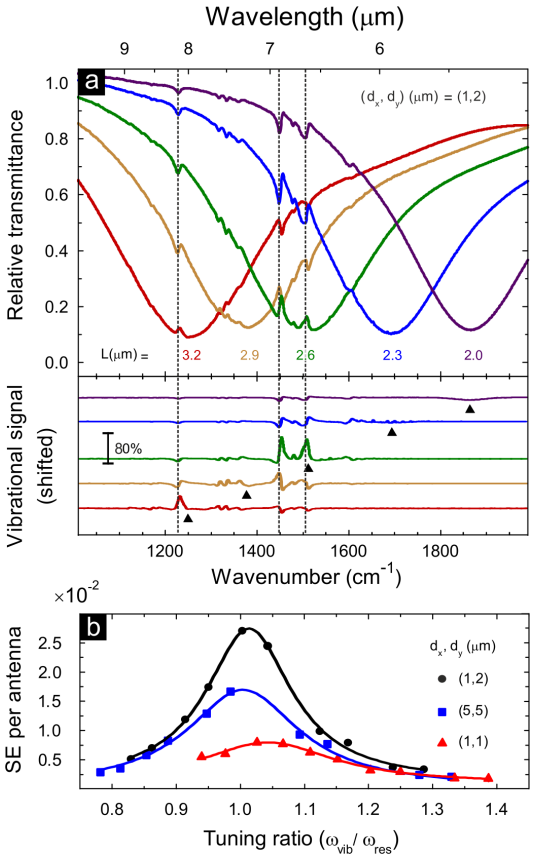

Figure 5.7: Surface-enhanced infrared spectroscopy of CBP covered nanoantennas. (a) Upper panel: relative transmittance spectra of a representative antenna arrays with same distances and antenna widths (140 nm) but different lengths as indicated. Lower panel: Corresponding baseline corrected IR spectra with resonance positions indicated by black triangles. Due to the differences in resonance matching of the antennas, different enhanced signals and line-shapes are observed. (b) Signal enhancements (SE) per antenna of the strongest CBP vibrational bands (1450 and 1504 cm^{-1}) versus tuning ratio (ratio of vibration frequency to resonance frequency).

panel, the signal enhancement strongly depends on the match between the vibrational frequency (ω_{vib}) and the plasmonic resonance frequency (ω_{res}). This becomes even more obvious in Figure 5.7b, where the signal enhancement per antenna of the CBP vibration at 1450 and 1504 cm^{-1} in dependence of the tuning ratio ($\omega_{vib}/\omega_{res}$) is plotted for selected configurations (d_x, d_y). As expected, the signal enhancement per antenna peaks around a tuning ratio of one, corresponding to a perfect match between vibrational and resonance frequency.

Finally, by taking the maximum values determined in Figure 5.7b, the signal enhancement per antenna over the longitudinal and transversal spacings between antennas is obtained (Figure 5.8). Notably high values are found close to d_y = 5 μm for the vibration at ω = 1230 cm^{-1} (Figure 5.8a) and d_y = 2 μm for the vibrations at ω = 1450 cm^{-1} and ω = 1504 cm^{-1}, (Figure 5.8b). The appearance of the enhancement maxima can be explained by the excitation of collective resonances in metal arrays, namely the Rayleigh anomalies [198, 199]. As discussed in the introduction, stronger near fields and thus stronger SEIRA enhancements [178, 200] are found for nanoantennas arranged with the critical grating periodicity. In a first approximation, only the interaction between next neighbors is considered and the contributions from longitudinal coupling is neglected, since a dipole antenna radiates preferentially perpendicular to its axis of polarization [180, 201]. According to equation 5.1, a critical grating distance $d_{crit} \approx 5.6$ μm (difference of critical grating periodicity Δ_y and antenna width W) for the maximum signal enhancement per antenna of the CH deformation vibration at 1230 cm^{-1} is deduced, which is in the good agreement with the experimental data (see Figure 5.8a). Slight deviations may originate from an angle dependency of the collective plasmonic excitation [201]. For the vi-

brations located at 1450 and 1504 cm^{-1}, which can be pooled due to their spectral vicinity, one calculates $d_{crit} \approx 4.6$ µm as critical grating distance. Obviously, this estimated critical spacing deviates from the experimentally determined maximum signal enhancement per antenna (Figure 5.8b). As shown by Adato et al. [201], spacings slightly larger than the critical grating distance result in a strong damping of the collective plasmonic resonances and a loss of the additional near field enhancement. Thus, only a relatively small spectral window provides additional enhancement, which was not precisely matched to the antenna resonance and the vibrational bands at 1450 and 1504 cm^{-1} in the experiments. However, the maximum signal enhancements per antenna of different vibrations scale with the critical grating distance as expected from equation 5.1 and qualitatively seen in Figure 5.8. Furthermore, the maximum value differs due to the stronger near fields found for longer antenna lengths [202].
For both plots, a remarkably sharp drop is observed for transversal spacings d_y smaller than 2 µm while the effect is much less prominent for longitudinal spacings d_x. This result is in agreement with previous studies [155, 180], where a strong broadening of the plasmonic resonances and a decrease of the near field intensity was found for small spacings d_y induced by transversal coupling. In contrast to that, longitudinal coupling over µm-sized d_x only marginally affects the antenna resonance and near field enhancement [180]. However, a further decrease of d_x down to several tens of nanometers, which is not subject of the present study, results in higher SEIRA enhancements due to near field coupling as shown for example in ref [84]. For larger separations of d_y, the benefit of plasmonic interaction vanishes and the signal enhancement per antenna decreases. Nevertheless, also the limit of a single nanoantenna is of potential in-

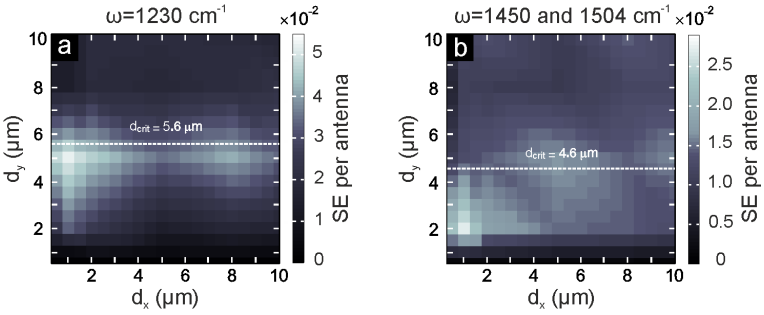

Figure 5.8: Signal enhancement (SE) per antenna of the vibrations at (a) 1230 cm^{-1} and (b) 1450 and 1504 cm^{-1} over the longitudinal d_x and transversal d_y spacing. Due to the close spectral vicinity of the vibrations at 1450 cm^{-1} and 1504 cm^{-1}, both modes are grouped together (see text). Notably high values are found in (a) for d_y = 5 µm and in (b) for d_y = 2 µm with the highest signal enhancement at (d_x, d_y) = (1, 5) (µm) and (1, 2) (µm), respectively, indicating a significant influence of the collective plasmonic excitation in antenna arrays on the signal enhancement. The total enhancement is the signal enhancement per antenna multiplied with the total number of antennas that participate in the collective resonance, which ranges typically in the order of 100 to 4000. The dashed lines indicate the calculated critical grating distances d_{crit}. The area between the measurement points is linearly interpolated.

terest, since here the absolute amount of detectable molecules is lowest. Please note that the signal enhancement (not normalized to one antenna) peaks at slightly smaller spacings (see Figure 5.9), but the above-mentioned behavior still holds. For example, smaller distances do not necessarily provide higher signals, even though more antenna hotspots are available for enhancement. This is in contrast to other studies with periodically arranged ITO nanoparticles acting as SEIRA substrates [175]. There, the signal enhancement scales with the antenna density, since collective plasmonic excitations are negligible due to the high absorption but low scattering of the particles.

Finally, the SEIRA enhancement factor is representatively esti-

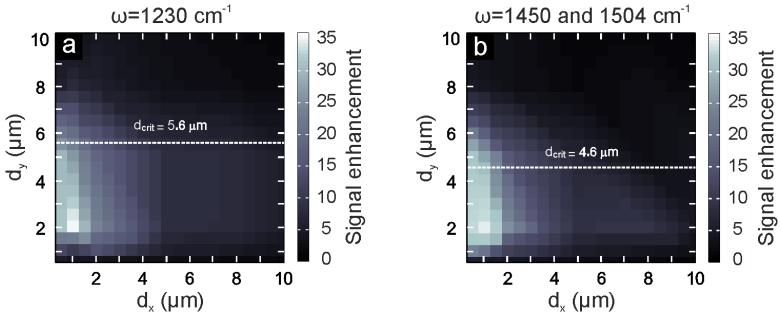

Figure 5.9: Signal enhancement (not normalized to one antenna) of the vibrations at (a) 1230 cm^{-1} and (b) 1450 and 1504 cm^{-1} over the longitudinal d_x and transversal d_y spacing. Due to the close spectral vicinity of the vibrations at 1450 cm^{-1} and 1504 cm^{-1}, both modes are grouped together. Notably high values are found in (a) and (b) for d_y = 2 µm with the highest signal enhancement at (d_x, d_y) = (1, 2) (µm), indicating a significant influence of the collective plasmonic excitation in periodically arranged antenna arrays and the number of available hotspots. The dashed lines indicate the calculated critical grating distances d_{crit}. The area between the measurement points is linearly interpolated.

mated by taking into account the molecules located in the confined electromagnetic near fields of the antennas. Only molecules situated in these active areas contribute to the enhanced vibrational signal. Therefore, the maximum signal enhancement per antenna (SE $\approx$ 0.04) is multiplied, which is found for the spacing (d_x, d_y) = (1, 5) µm and ω = 1230 cm^{-1}. Assuming an active area two times the antenna end faces according to Ref. [67] and a homogenous coverage, an enhancement factor of 14000 is found, in agreement with other studies [17, 155, 203].

In summary, femtosecond direct laser writing and argon ion beam etching were combined to fabricate homogeneous large-area nanoantenna arrays providing plasmon resonances in the mid-infrared spectral range. Such nanoantennas are ideally suited as substrates for surface-enhanced infrared absorption, as

demonstrated by enhancing vibrational signals of CBP molecules evaporated on antenna arrays with different spacings between the elements. The signal enhancement is strongly influenced by plasmonic coupling that originates from the periodical arrangement of antennas and is maximum close to the Rayleigh anomaly. For this optimum configuration, a maximum SEIRA enhancement factor of about four orders of magnitude is found, which is comparable to the SEIRA activity of substrates prepared with other nanofabrication methods such as interference lithography, colloidal hole mask lithography, or electron-beam lithography.

5.6 PLASMONIC NANOANTENNAS ON SINGLE CRYSTALLINE GOLD PLATES

As suggested, the method establishes a low-cost replacement technique for electron beam lithography since it allows for simple, fast, and straightforward fabrication of nanoantenna arrays. However, the method can be optimized for further application. For example to make nanostructures out of single crystalline gold plates. Single crystalline gold plates have been attracting due to the their high structural homogeneity compared with conventional multi-crystalline structures. They are atomically flat and significantly more precise shapes and favorable optical properties compared to those made from evaporated gold films. Moreover, gold plate synthesis is simple, cheap and requires no specialized instrumentation. Also, it has been shown that surface-enhanced infrared spectroscopy benefits from nanoantenna made of such plates. Normally, focused ion beam (FIB) milling is used for nanostructuring of single crystalline gold plates by using gallium beam to remove unwanted area but it can be also done by using etching process. Figure 5.10 shows

how the hexagonal shaped gold plate (located in the gray circle) can be etched via argon ion beams. Optical microscope images of the 40 nm thick gold plate on silicon substrate before etching is shown in Figure 5.10a. The plate is etched partially via 120 seconds standard etching process (Figure 5.10b, beam current range from 90 to 100 mA) and can be totally removed by using an extra etching process with same parameters (Figure 5.10c). Compared to evaporated gold films this gold plates show higher resistivity (about factor of 2) in front of argon ions. Etching of the gold

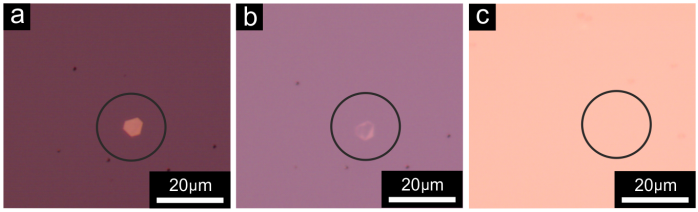

Figure 5.10: Microscope images of a single crystalline gold plate after and before etching via Ar ions. (a) A 40 nm thick hexagonal shaped gold plate before etching process. (b) The sample then is put into the etching machine for 120 seconds (beam current range from 90 to 100 mA), resulting in a decrease the thickness. (c) An extra etching process with same parameters cause vanishing of the gold plates. The position of hexagonal shaped gold plate is shown by black circles.

plates can be done selectively via illumination of photoresist-covered plate by using direct laser writing and subsequent argon ion beam etching. Figure 5.11a shows a microscope image of such a plate after exposure and development processes. The pattern then is etched to the gold via argon etching as shown in the SEM image (Figure 5.11b). Antenna lengths and widths are 500 and 200 nm respectively.

As the direct laser writing lithography is independent of substrate such a nanoantenna can be fabricated on the transparent substrate such as CaF_2. Figure 5.12 shows plasmonic resonances

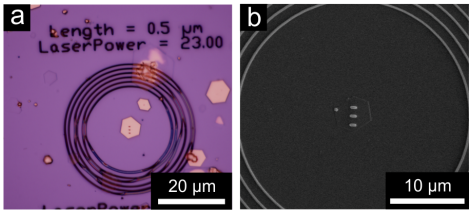

Figure 5.11: Nanostructuring of single crystalline gold plates by direct laser writing lithography. (a) Microscope image of hexagonal shaped gold plate on silicon substrate which has antenna pattern of polymers on top. (b) Nanoantenna are transfered to the gold via Ar ion beam (etching time 300 seconds, beam current range from 90 to 100 mA). Antenna lengths and widths are 500 and 200 nm respectively.

of the nanoantennas at 3800 cm^{-1}. The corresponding SEM image is also shown as an inset. Antenna lengths and widths are 800 and 200 nm respectively. The quality of the plasmon resonance is comparable with previous works have done by focused ion beam milling and can be tuned by changing the nanostructures geometry.

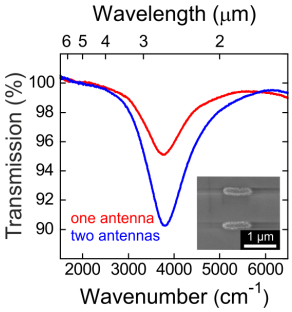

Figure 5.12: Optical properties of gold nanoantenna on CaF_2 substrate fabricated by direct laser writing lithography. Antennas (length: 800 nm, width 200 nm) show plasmon resonance at about 3800 cm^{-1}. The inset shows an SEM image of corresponding antennas.

These preliminary results show direct laser writing lithography can be easily utilized for nanostructuring of chemically synthesized gold plates. Further work can be done to improve the uniformity of gold microplates with larger size to achieve arrays of gold nanostructures for plasmonics application.

6

REFRACTORY PLASMONICS

In this chapter, Titanium nitride (TiN) nanoantennas that are tunable throughout the mid-IR are fabricated and their optical performance are demonstrated. The antennas are overcoated with aluminum oxide (Al_2O_3) to prevent degradation during annealing of up to 800°C and prove the existence of the plasmonic resonances after high temperature treatment. Also two different methods are given to fabricate large-area (cm^2 sized) arrays of such high-temperature antennas. Following the general theme that novel materials for plasmonics are highly sought after, in particular for refractory plasmonics, the finding can contribute significantly to this field.

*Robust plasmonic nanoantennas at mid-infrared wavelengths are essential components for a variety of nanophotonic applications ranging from thermography to energy conversion. TiN is a promising candidate for such cases due to its high thermal stability and metallic character. Here, direct laser writing as well as interference lithography are employed to fabricate large-area nanoantenna arrays of TiN on sapphire and silicon substrates. Both lithographic tools allow for fast and homogeneous preparation of nanoantenna geometries on a polymer layer, which

* This Chapter is adapted from S. Bagheri et al., Large-Area Fabrication of TiN Nanoantenna Arrays for Refractory Plasmonics in the Mid-Infrared by Femtosecond Direct Laser Writing and Interference Lithography, *Optical Materials Express* 5, 2625-2633 (2015). Reprinted with permission. Copyright 2016 The Optical Society. All Rights Reserved.

is then selectively transferred to TiN by subsequent argon ion beam etching followed by a chemical wet etching process. The antennas are protected by an additional Al_2O_3 layer which allows for high-temperature annealing in argon flow without loss of the plasmonic properties. Tailoring of the TiN antenna geometry enables precise tuning of the plasmon resonances from the near to the mid-infrared spectral range. Due to the advantageous properties of TiN combined with the versatile large-area and low-cost fabrication process, such refractory nanoantennas will enable a multitude of high-temperature plasmonic applications such as thermophotovoltaics in the future.

6.1 BASIC PRINCIPLES

Plasmonics is at the heart of many aspects of nano-optics and photonics, where it has been utilized for a broad variety of research and commercial applications. One significant feature of plasmonic resonators is their ability to concentrate light into deep subwavelength volumes, enabling efficient light confinement on the nanoscale as well as antenna-enhanced sensing approaches [2, 120, 121, 204]. Building on this concept, plasmonic geometries have led to the realization of artificial optical materials with novel properties such as negative refraction [205], perfect absorption [13, 90, 119, 128], and the plasmonic analogue of electrically induced transparency from atomic physics [206, 207]. Plasmonic geometries commonly rely on noble metals such as Au, silver (Ag) and aluminum (Al) due to their comparatively small Ohmic losses and well-understood optical and mechanical properties.

However, in order to improve the efficiency of current plasmonic designs and to realize novel concepts, there is an increased need

for additional classes of plasmonic materials. Particularly, semiconductor materials such as highly doped silicon (Si) [208] and transparent conducting oxides (TCO) [209] have been introduced due to their tunable optical properties and compatibility with standard industrial chip-scale processing technologies. Also, materials which undergo a phase change in response to an external stimulus such as vanadium dioxide (VO_2) [210], germanium antimony telluride (GST) [211], Y [134] and Mg [135] have been employed to realize active plasmonic devices.

Another crucial material-related challenge is the stability of plasmonic structures at the very high-temperatures that are relevant to many industrial processes. This requirement is difficult to satisfy using metals with comparatively low melting points, and hence necessitates a transition to more stable, so-called refractory materials [212]. Such materials are chemically stable at temperatures above 2000°C and are thus ideal candidates for high-temperature plasmonic applications such as thermophotovoltaics [102], perfect absorption and thermal emission [113, 213], and nanoscale-heat transfer systems [105]. This is especially important when operating plasmonic structures as thermal emitters, where high device temperatures are needed to achieve the desired emission wavelengths, e.g., in the mid- and near-infrared. Titanium nitride (TiN) has emerged as a promising material for refractory plasmonics [212, 214] and other high-temperature applications [215] due to its negative real value of permittivity and low interband loss in the near- and mid-infrared spectral range [100, 111, 216]. However, the fabrication of TiN nanostructures with tunable plasmonic resonances over large areas has proven challenging. Here, fast and wafer-scale fabrication methods such as direct laser writing (DLW) [19] and laser interference lithography (LIL) are utilized [17, 217–219] to create a regular polymer

pattern, which is then selectively transferred into a TiN layer through a combination of dry and chemical wet etching processes. Following this approach, large-area nanoantenna arrays of TiN with tunable plasmon resonances from the near- to the mid-infrared spectral range are achieved. Due to the refractory properties of TiN, the fabricated nanoantennas are good candidates for high-temperature plasmonic applications, particularly when covered with an oxide-resistant layer with high temperature stability such as Al_2O_3 or silicon nitride (Si_3N_4) layer.

6.2 TIN NANOANTENNAS FABRICATION

A schematic drawing of the TiN nanoantenna fabrication process is shown in Figure 6.1. First, substrates are sonicated for 10 minutes in acetone as well as isopropanol. In addition, the Si substrates undergo a 30 second hydrofluoric acid (49 %) dip prior to sonication. Subsequently, the substrates are loaded into the sputtering chamber (AJA International ATC 2200-V6) and cleaned under vacuum condition by Ar plasma (25W). Afterwards a 50 nm TiN layer is deposited using non-reactive sputtering (10^{-8} Torr, RF power: 150 W, Ar flow: 40 sccm, deposition pressure: 4 mT, temperature: 20^{o}C, applied bias: 100 V). Then, a 5 nm chromium (Cr) adhesion layer and a 100 nm gold (Au) intermediate layer are evaporated (Pfeiffer Vacuum Model PLS-500, 10^{-7} mbar). The purpose of the gold layer is to assist in the wet etching process as an additional mask since the polymer layer is partly damaged during the wet etching.
Figure 6.1a-f show the fabrication processes of the nanoantennas. The photoresist (Nanoscribe IP-Dip, development in Microresist mr-dev 600 for 15 minutes) is drop-cast onto the multilayer sample, and direct laser writing (Nanoscribe GmbH) is

utilized to create nanoantenna patterns in the polymer. These patterns are then transferred first to the gold film via argon ion beam etching (Technics Plasma Model R.I.B.-Etch 160, etching rate: 0.5 nm/sec) and then to the TiN film via a chemical wet etching process by using NH_4OH: H_2O_2: H_2O (1: 2: 5) solution (75°C, etching rate: 0.5 nm/sec). Afterwards, the sample is immersed in distilled water for 60 seconds and dried using nitrogen. Finally the photoresist and the gold layer are removed via oxygen plasma (Diener electronic Plasma-Surface-Technology, 100 min, 1.3 mbar, 160 W) and argon ion beam etching, respectively. Relative transmittance spectra of the nanoantenna arrays (200×200 μm^2) are measured using a Bruker Hyperion microscope coupled to a Bruker Vertex 80 spectrometer.
The proposed refractory plasmonic TiN nanoantenna design can be implemented using other large-area fabrication methods such as interference lithography. However, this requires optimization of photoresists and metal thicknesses as will be demonstrate in the following. For manufacturing TiN nanoantenna arrays by interference lithography, the photoresist (ma-N 405) is spin-coated on Cr (2 nm) and Au (35 nm) layers and the development process is carried out in AZ826 developer for 48 seconds.

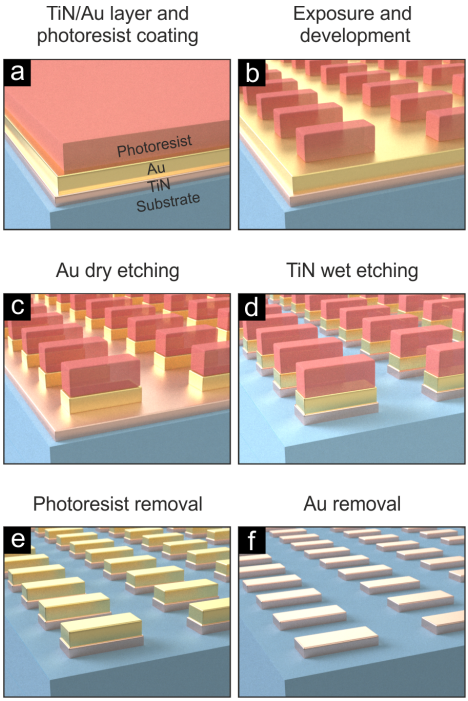

Figure 6.1: Schematic drawing of the fabrication process of TiN nanoantennas: (a) TiN films are sputtered and Au films are evaporated on a substrate. Subsequently, the photoresist is coated on top. (b) Exposure and development processes create the antennas mask in the polymer, which is transferred first to (c) Au via argon ion beam dry etching and then to (d) the TiN film by chemical wet etching. (e) The photoresist and (f) gold are removed by oxygen plasma and argon ion beams, respectively. Additionally, an oxidation-resistant layer can be deposited onto the TiN antennas to protect them from oxygen when annealing at high-temperatures.

6.3 OPTICAL PROPERTIES OF TIN NANOANTENNAS

The fabricated nanoantennas provide a plasmon resonance which is strongly dependent on the antenna material and consequently

the dielectric function of the TiN film. To investigate this further, the dielectric functions of the TiN films used in the fabrication process (thickness 50 nm) are measured via spectroscopic ellipsometry (Woollam variable angle spectroscopic ellipsometer (VASE), spectral range 0.3 to 2.2 μm, angles of incidence varied from 45^{o} to 65^{o} in steps of 5^{o}). The ellipsometric data are modeled by a general oscillator layer model with a mean square error (MSE) of 0.7. The real and imaginary parts of the dielectric function were extrapolated from the model up to the mid-infrared range as shown in Figure 6.2a and 6.2b respectively. The real (ε_1) and the imaginary (ε_2) parts of the dielectric function of the TiN film on both silicon and sapphire substrates exhibit metallic behavior (negative real permittivity and low interband loss) in the near- and mid-infrared spectral regions, comparable to TiN films demonstrated by other groups [220]. The slight difference between dielectric functions of TiN film on silicon and sapphire substrate is to be expected since the different lattice matching of the substrates influences the dielectric functions of TiN films as demonstrated previously [221]. However, the modeled results show some sensitivity to the film thickness; therefore, the rate-estimated sputtering thickness are verified by performing both Dektak profilometry and X-ray reflectometry measurements. These optical constants are used to estimate the plasmonic resonance of the nanoantennas by employing a Fourier modal method numerical simulation approach [141]. As expected, the geometry of the TiN nanoantennas plays an important role for tailoring the plasmon resonance wavelength over the near- and mid-infrared range. Figure 6.2c shows simulated relative transmittance spectra (parallel polarization) of the nanoantennas with different periodicities (P) and antenna lengths (L) on a sapphire substrate, demonstrating ge-

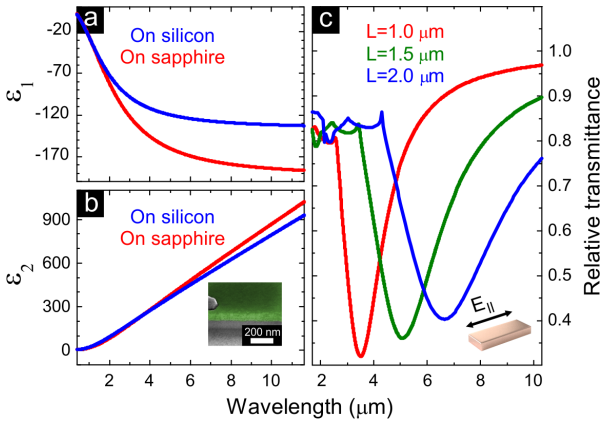

Figure 6.2: (a) Real (ε_1) and (b) the imaginary (ε_2) parts of the dielectric function of a TiN thin film on silicon (blue line) and sapphire (red line) substrates extracted from the modeled spectroscopic ellipsometry measurements and extrapolated to 12 μm. (c) The measured optical properties of the TiN film are used to simulate the plasmon resonance (polarization of the electric field $E_{\|}$ is parallel to the antenna long axis) of nanoantennas with different lengths (L) using a Fourier modal method numerical simulation, resulting in tunable plasmon resonances from near- to mid-infrared in spectral range. The kinks in the simulated plasmonic resonances (panel c) are Rayleigh anomalies due to grating resonances. A cross section SEM image of the TiN film is shown as the inset in Figure 6.2b.

ometrical plasmon resonance tunability from the near- to mid-infrared (red: P = 1.5 μm and L = 1.0 μm, green: P = 2.0 μm and L = 1.5 μm, blue: P = 2.5 μm and L = 2.0 μm). Figure 6.3 shows the plasmon resonance of such a nanoantenna array (P = 1.5 μm, L = 0.83 μm), demonstrating good agreement between simulation and experiment. However, the slight difference between the simulation and the experiment could arise from the chemical wet etching process which causes imperfect walls and surface roughness of the antennas.

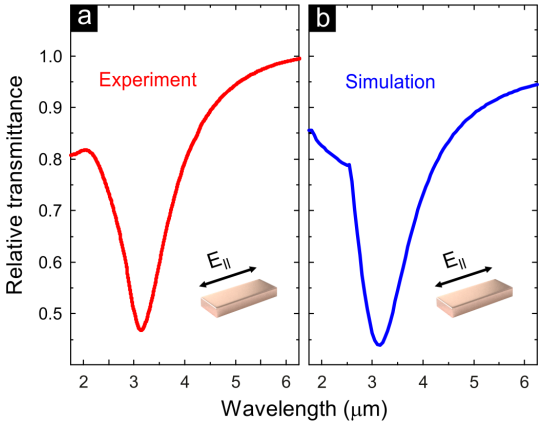

Figure 6.3: Simulated (a) and experimental (b) results of relative transmittance spectra of the TiN antenna arrays fabricated by direct laser writing (parallel polarization, $E_{||}$). The antenna lengths and widths are 0.83 μm and 200 nm, respectively, and the periodicity of antennas parallel to the antenna long (short) axis is 1.5 μm. The height of the TiN is 50 nm.

6.4 THERMAL STABILITY OF TIN NANOANTENNAS

A crucial point for applications is the stability of the TiN nanoantenna arrays at high-temperatures. As has been shown previously, TiN is a refractory material with excellent thermal stability, even for temperatures above 2000°C [212]. However, high-temperature annealing of TiN in oxygen-containing environment will lead to oxidation of the material [168] and consequently, due to the small size and high surface area of the nanoantennas, cause the complete disappearance of the plasmon resonance as shown in Figure 6.4a. Previous studies have shown that TiN will not significantly oxidize at temperatures below 300-350°C [216, 222], but as with many nitrides, at higher temperatures such as those explored here, oxidation can become an issue.

Whereas annealing of TiN under vacuum condition can prevent oxidization of TiN nanostructures and keep the optical properties of TiN film stable [113], the use of thin dielectric coatings has also been suggested to reduce this oxidation in TiN films [168]. Figure 6.4a shows relative transmittance of the nanoantenna arrays before (blue line) and after annealing (red line) at 800°C. The plasmon resonance clearly disappears after the annealing process. To overcome this problem, a 200 nm thick Al_2O_3 layer, a refractory dielectric transparent over the near- to mid-IR range, is incorporated and sputtered on top of the fabricated TiN nanoantenna arrays in an attempt to prevent oxygen from the surrounding environment from reaching the TiN antennas. The addition of this film only causes a 0.5 μm spectral shift of the antenna resonance to longer wavelengths combined with a slight broadening of the lineshape, while the modulation depth is maintained as shown in Figure 6.4b.

The sample is then annealed in Ar flow at a temperature of 800°C for about 45 minutes. The argon flow does not prevent oxidization of TiN but is necessary for an accurate measurement of the annealing temperature. Looking again at the optical response of the antenna arrays, the resonance position is maintained while the modulation depth of the resonance decreases by around 15 % as shown in Figure 6.4 (red line). The reduced modulation depth is most likely due to intrinsic oxygen interdiffusion between Al_2O_3 and TiN or diffusion of oxygen from the native surface oxide (TiO_2) into the thin film. Choosing different oxidization-resistant cap layers, e.g. Si_3N_4, may decrease the rate of oxidization or avoid it entirely. Still, the experiments clearly demonstrate the thermal stability of the Al_2O_3-protected TiN nanoantenna arrays, as confirmed by the pronounced plasmonic resonance visible after annealing.

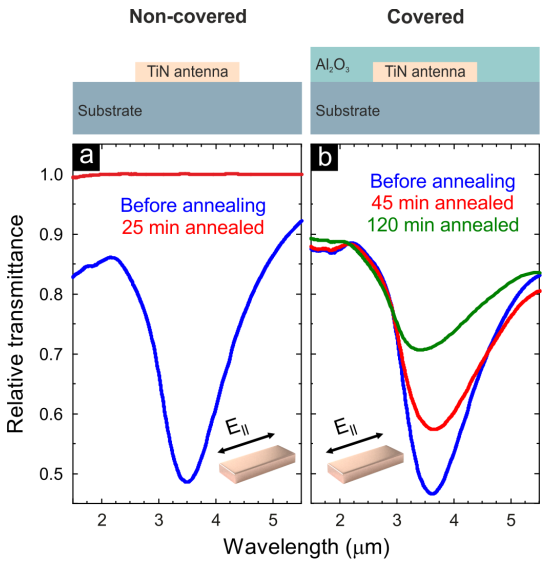

Figure 6.4: High-temperature stability of TiN nanoantennas on sapphire substrate without protection layer as well as covered with aluminum oxide (Al_2O_3). (a) The TiN nanoantennas (fabricated by direct laser writing) show a pronounced plasmonic resonance at a wavelength of around 3 μm (blue line). After annealing at 800°C the plasmon resonance is vanished due to the oxidization (red line). (b) When the sample is covered with a 200 nm thick Al_2O_3 protective layer, the resonance undergoes a spectral shift of around 0.5 μm to longer wavelengths combined with a slight broadening of the lineshape (blue line). Annealing at a temperature of 800°C induces only a small decrease of the modulation depth of the resonance (red line). Further annealing (green line) causes a degradation of the Al_2O_3 layer and consequently a blue shift of the plasmon resonance as well as a further decrease of the modulation depth (periodicity = 1.5 μm, length = 1.0 μm, width = 200 nm, height = 50 nm).

This fabrication method enables the fabrication of a wide range of antenna arrays with varying lengths from 0.2 to 1.4 μm. This is demonstrated by displaying selected scanning electron microscope (SEM) images of the nanoantenna arrays on Si sub-

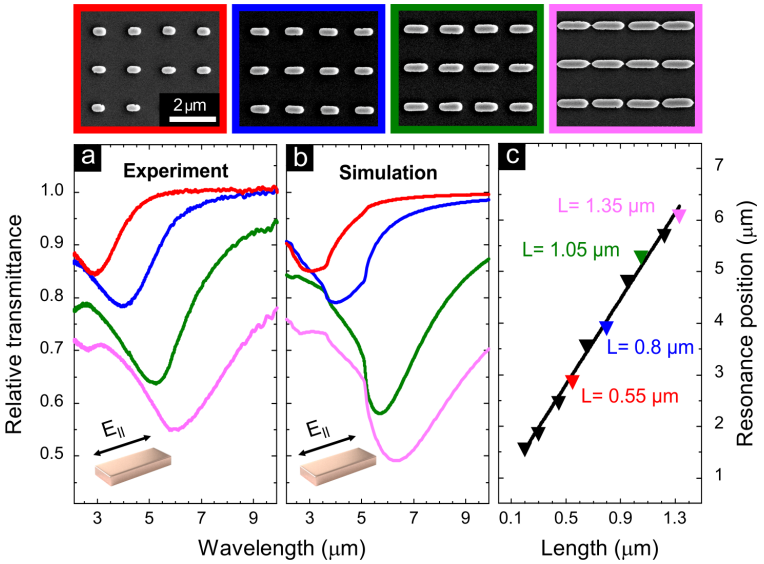

Figure 6.5: SEM images, relative transmittance spectra (experiment and simulation), and plasmon resonance positions of antennas fabricated by direct laser writing lithography on a Si substrate are shown. (a) Relative transmittance spectra (parallel polarization, $E_{||}$) of the selected antenna arrays show tunability of the plasmon resonances from the near- to mid-infrared. (b) The corresponding simulated spectra are in fair agreement with experiment. Deviations are due to the imperfect surface of the antennas created by the wet etching process. (c) The plasmon resonance position of the antenna arrays exhibits a linear dependence of the resonance wavelength on the antenna length. Selected antennas are labeled with the corresponding color from panel (a). The periodicity of antennas parallel to both the long and the short antenna axes is 1.5 μm, antenna lengths are varied from 0.2 to 1.35 μm, and the antenna widths and heights are 250 and 50 nm, respectively.

strate. Typical relative transmittance spectra (parallel polarization, $E_{||}$) of the corresponding nanoantenna arrays are shown in Figure 6.5a, demonstrating tunability of the resonance wavelength from the near- to mid-infrared spectral range. The results

are in fair agreement with the simulation. The plasmon resonance positions of different nanoantenna arrays fabricated by femtosecond direct laser writing lithography show a linear correlation with the antenna lengths as shown in Figure 6.5b. The peak positions correspond to different temperatures of blackbody radiation and can thus be designed to provide the best match with the blackbody emission spectrum for a given temperature [88].

6.5 LARGE-AREA FABRICATION

Direct laser writing lithography can easily provide antenna masks over 200 × 200 μm^2 areas with processing times on the order of a few seconds; however, the approach for nanoantenna fabrication can also easily be extended to other lithographic tools. Particularly, large-area and low-cost fabrication is highly sought after for real-world applications. As an established technique for wafer-scale processing, laser interference lithography is a prime candidate for fabricating large-area plasmonic structures. This is demonstrated by fabricating a large-area (10 × 10 mm^2) sample covered with TiN nanoantennas as shown by the photograph in Figure 6.6a. Figure 6.6b shows the typical SEM image of TiN antenna arrays fabricated by interference lithography (periodicity: 2.1 μm, length: 1.7 μm, width: 0.8 μm, height: 50 nm) and demonstrates the excellent homogeneity of the large-area sample. The relative transmittance spectrum of such antenna arrays (parallel polarization, $E_{||}$) clearly shows a plasmon resonance in the mid-infrared (around 7 μm) as evident from Figure 6.6c.
In summary, direct laser writing as well as laser interference lithography were employed to fabricate TiN nanoantennas featuring high quality plasmon resonances in the near- and mid-

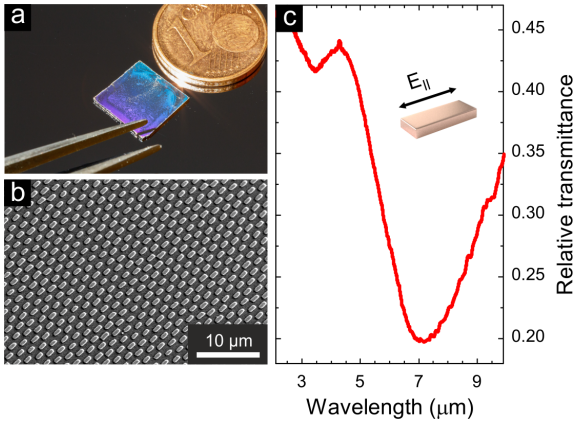

Figure 6.6: Large-area fabrication of TiN antennas by laser interference lithography on a Si substrate. (a) A photograph of the sample demonstrates the homogeneity of the antenna arrays over a large-area (10 × 10 mm²). (b) Tilted view scanning electron micrograph of the fabricated TiN antennas (length: 1.7 µm, width: 0.8 µm, height: 50 nm). (c) Relative transmittance spectrum (parallel polarization, $E_{||}$) of the fabricated antennas.

infrared spectral range. Large-area and low-cost preparation of such nanoantenna arrays combined with the intrinsic character of TiN as a refractory material makes such nanoantennas well-suited for high-temperature plasmonic application such as thermophotovoltaics, thermal imaging as well as nano-heat transfer systems. A protective layer of 200 nm Al_2O_3 makes the optical response of the antennas nearly immune to annealing at 800°C in argon flow. This indicates that the Al_2O_3 layer greatly improves the thermal stability of the TiN antennas. To prevent oxygen interdiffusion, oxygen-less capping layers such as Si_3N_4, SiN and HfO_2 should also be tried in the future. Due to its simplicity and broad applicability, the method opens the door to large-area and low-cost refractory plasmonics in the mid-infrared.

7

CONCLUSION

This thesis has covered a variety of active plasmonic devices for applications ranging from gas and molecular sensing to refractory plasmonics.

In order to perform spectroscopy over large-area, homogeneous plasmonic nanostructures were fabricated in the fast and low-cost manners such as laser interference lithography and femtosecond direct laser lithography.

Focusing first on plasmonic-based perfect absorption concept for facilitating hydrogen dissociation, Lloyd's mirror setup [139] in laser interference lithography was used, which allowed for square centimeter preparation of plasmonics nanostructures with different geometries such as wire and square in polymers where periodicities below 800 nm are required. The subsequent etching process was used to transfer the pattern to palladium to obtain widely tunable plasmon resonances and consequently spectrally selective perfect absorption of light from visible to near-infrared in the spectral range.

The optical properties of the Palladium was modified in the presence of H_2 through the phase transition from palladium to palladium hydride [140]. The significant changes in the real and imaginary parts of the palladium dielectric function destroy the optimized impedance matching condition of the perfect absorber and consequently change the reflectivity profile of the system. This was observed in the spectra as a spectral red-shift of about 10 nm and also relative reflectance change ($\Delta R_{rel.}$) be-

tween the 0% and 4% hydrogen concentrations over wavelength, indicating signal changes of almost 400%[18].

In order to push our high-quality resonances toward mid-infrared regime and consequently perform vibrational sensing using surface enhanced infrared spectroscopy, a home build setup [17] was employed, which enabled us to increase periodicity larger than 800 nm and consequently achieve bigger nanostructures than what had obtained via Lloyd's mirror setup. Therefore, the resonances were easily tunable in the mid-infrared regime and thus ideally suited for antenna-assisted surface-enhanced infrared absorption. To demonstrated that two molecular substances, namely octadecanethiol and the polymer XARP were used and measured differences in signal enhancement (72000 for octadecanethiol and 900 for the polymer) were observed. In comparison to conventional infrared spectroscopy, the signal enhancement significantly improved. Also, the UV-induced degradation of the XARP polymer with an increased sensitivity via vibrational signal decay without modifying the degradation process itself was in-situ monitored. The results demonstrated the capability of laser interference lithography for homogeneous fabrication plasmonic nanoantennas over the large-areas with high-quality resonances that can be specifically tailored for SEIRA applications [17].

Although laser interference lithography turned up as a very promising fabrication method to achieve large-area and low-cost plasmonic nanostructures, the geometrical parameters can not be selected independently, which limits the application of this method for specific approaches. Moving beyond this limitation, for the first time, the use of femtosecond direct laser writing combine with argon ion beam etching was applied to overcome the problem and achieve homogeneous large-area nanoantenna

arrays. Such nanoantennas were used for surface-enhanced infrared absorption by enhancing vibrational signals of CBP molecules evaporated on antenna arrays with different spacings between the elements.

Via our comprehensive study, it was shown the signal enhancement is strongly influenced by plasmonic coupling that originates from the periodical arrangements of the antennas and is maximum close to the Rayleigh anomaly. For the optimum configuration, a maximum SEIRA enhancement factor of about four orders of magnitude was found, which was comparable to the SEIRA activity of substrates prepared with other nanofabrication methods such as interference lithography, colloidal hole mask lithography, and electron-beam lithography[19].

In the last part of the thesis, both direct laser writing and interference lithography were combined with the chemical wet etching as well as dry etching for nanostructuring of titanium nitride (TiN) featuring the high-quality plasmon resonances in the near- and mid-infrared spectral ranges. The large-area and low-cost preparation of such nanoantenna arrays combined with the intrinsic character of TiN as a refractory material made such nanoantennas well-suited for high-temperature plasmonic applications such as thermophotovoltaics, thermal imaging as well as nano-heat transfer systems. A protective layer of 200 nm Al_2O_3 greatly improved the thermal stability of the TiN antennas and made the optical response of the antennas nearly immune for annealing at 800°C [20]. Due to its simplicity and broad applicability, this method opens the door to large-area and low-cost refractory plasmonics in the mid-infrared.

Building on the presented results, there are several promising research directions, where active plasmonic devices can be applied in the future.

First, to prevent oxygen interdiffusion, oxygen-less capping layers such as Si_3N_4 and hafnium oxide (HfO_2) can also be tried in the future.
Second, other refractory plasmonics materials such as niobium (Nb) could be explored, aiming to establish a universal material for plasmonics application since niobium shares many advantages of other plasmonics materials such as hydrogen storage capabilities, high-temperature stability, and superconductivity.
Finally, the concept of high-temperature plasmonics can be combined with surface enhanced infrared spectroscopy for detection of the molecular vibration such as carbon monoxide (CO), where temperatures higher than 250°C are necessary to load CO molecules on the surface of oxide catalysis such as tin dioxide (SnO_2).
Going beyond the ideas outlined here, the versatility of laser interference lithography and direct laser writing for fabrication of various plasmonic geometries will lead to a multitude of new designs and applications, which can potentially bring plasmonic-based concepts to technological and industrial devices that are used every day.

ACRONYMS

A absorption

AFM atomic force microscopy

Ag silver

Al aluminum

Al_2O_3 aluminum oxide relative intensity

Ar argon

Au gold

BDP bonding dimer plasmon

BEM boundary element methods

CaF_2 calciumdifluoride

cgs centimetre–gram–second system

CO carbon monoxide

CBP 4,4′-bis(N-carbazolyl)-1,1′-biphenyl

Cr chromium

CWL centroid wavelength

DDA dipole–dipole approximation

DLW direct laser writing

EBL electron beam lithography

FDTD finite difference in time domain

FIB focused ion beam

FTIR Fourier transform infrared spectroscopy system

GST germanium antimony telluride

H_2 hydrogen

HfO_2 hafnium oxide

HAMR heat-assisted magnetic recording

HUV ultra-high vacuum

IR Infrared

IRRAS Infrared reflection absorption spectroscopy

L lengths

LIL laser interference lithography

LSPs localized surface plasmons

meV milli-electron volt

Mg magnesium

MgF_2 magnesium fluoride

MCT mercury cadmium telluride

N_2 nitrogen

NA numerical aperture

Nb niobium

ODT octadecanethiol

Pd palladium

PdH palladium hydride

PMLs perfect matched layers

R reflection

s seconds

Si silicon

Si_3N_4 silicon nitride

SEIRA surface enhanced infrared absorption

SEM scanning electron microscope

SERS surface-enhanced raman spectroscopy

SPPs surface plasmon polaritons

SnO_2 tin dioxide

T transmission

TCO transparent conducting oxides

TiN Titanium nitride

TiO_2 titanium dioxide

TFSF total field scattered field

UV ultraviolet

VO_2 vanadium dioxide

W widths

Y yttrium

BIBLIOGRAPHY

[1] M. Hentschel, T. Weiss, S. Bagheri, and H. Giessen, "Babinet to the half: coupling of solid and inverse plasmonic structures," Nano Letters **13,** 4428–4433 (2013).

[2] Z. Liu, P. Zhan, J. Chen, C. Tang, Z. Yan, Z. Chen, and Z. Wang, "Dual broadband near-infrared perfect absorber based on a hybrid plasmonic-photonic microstructure.," Optics express **21,** 3021–30 (2013).

[3] A. Moreau, C. Ciracì, J. J. Mock, R. T. Hill, Q. Wang, B. J. Wiley, A. Chilkoti, and D. R. Smith, "Controlled-reflectance surfaces with film-coupled colloidal nanoantennas.," Nature **492,** 86–9 (2012).

[4] Y. Zhang, T. Wei, W. Dong, K. Zhang, Y. Sun, X. Chen, and N. Dai, "Vapor-deposited amorphous metamaterials as visible near-perfect absorbers with random non-prefabricated metal nanoparticles.," Scientific reports **4,** 4850 (2014).

[5] D. Wang, W. Zhu, M. D. Best, J. P. Camden, and K. B. Crozier, "Wafer-scale metasurface for total power absorption, local field enhancement and single molecule Raman spectroscopy.," Scientific reports **3,** 2867 (2013).

[6] C. V. Hoang, M. Oyama, O. Saito, M. Aono, and T. Nagao, "Monitoring the presence of ionic mercury in environmental water by plasmon-enhanced infrared spectroscopy.," Scientific reports **3,** 1175 (2013).

[7] D. A. Perry, R. L. Borchers, J. W. Golden, A. R. Owen, A. S. Price, W. A. Henry, F. Watanabe, and A. S. Biris, "Surface-enhanced infrared absorption on elongated nickel nanostructures," Journal of Physical Chemistry Letters **4,** 3945–3949 (2013).

[8] F. Le, D. W. Brandl, Y. A. Urzhumov, H. Wang, J. Kundu, N. J. Halas, J. Aizpurua, and P. Nordlander, "Metallic nanoparticle arrays: A common substrate for both surface-enhanced Raman scattering and surface-enhanced infrared absorption," ACS Nano **2,** 707–718 (2008).

[9] J. M. Hoffmann, X. Yin, J. Richter, A. Hartung, T. W. W. Maß, and T. Taubner, "Low-cost infrared resonant structures for surface-enhanced infrared absorption spectroscopy in the fingerprint region from 3 to 13 μm," Journal of Physical Chemistry C **117,** 11311–11316 (2013).

[10] Y.-C. Chang, S.-C. Lu, H.-C. Chung, S.-M. Wang, T.-D. Tsai, and T.-F. Guo, "High-throughput nanofabrication of infra-red and chiral metamaterials using nanospherical-lens lithography.," Scientific reports **3,** 3339 (2013).

[11] S. Cataldo, J. Zhao, F. Neubrech, B. Frank, C. Zhang, P. V. Braun, and H. Giessen, "Hole-mask colloidal nanolithography for large-area low-cost metamaterials and antenna-assisted surface-enhanced infrared absorption substrates," ACS Nano **6,** 979–985 (2012).

[12] B. Frank, X. Yin, M. Schäferling, J. Zhao, S. M. Hein, P. V. Braun, and H. Giessen, "Large-area 3D chiral plasmonic structures," ACS Nano **7,** 6321–6329 (2013).

[13] R. Walter, A. Tittl, A. Berrier, F. Sterl, T. Weiss, and H. Giessen, "Large-area low-cost tunable plasmonic perfect

absorber in the near infrared by colloidal etching lithography," Advanced Optical Materials **3,** 398–403 (2015).

[14] V. Auzelyte, B. Gallinet, V. Flauraud, C. Santschi, S. Dutta-Gupta, O. J. F. Martin, and J. Brugger, "Large-area gold/parylene plasmonic nanostructures fabricated by direct nanocutting," Advanced Optical Materials **1,** 50–54 (2013).

[15] S. Aksu, A. E. Cetin, R. Adato, and H. Altug, "Plasmonically enhanced vibrational biospectroscopy using low-cost infrared antenna arrays by nanostencil lithography," Advanced Optical Materials **1,** 798–803 (2013).

[16] S. Aksu, A. A. Yanik, R. Adato, A. Artar, M. Huang, and H. Altug, "High-throughput nanofabrication of infrared plasmonic nanoantenna arrays for vibrational nanospectroscopy," Nano Letters **10,** 2511–2518 (2010).

[17] S. Bagheri, H. Giessen, and F. Neubrech, "Large-area antenna-assisted SEIRA substrates by laser interference lithography," Advanced Optical Materials **2,** 1050–1056 (2014).

[18] S. Bagheri, N. Strohfeldt, F. Sterl, A. Berrier, A. Tittl, and H. Giessen, "Large-area low-cost plasmonic perfect absorber chemical sensor fabricated by laser interference lithography," ACS Sensors **1,** 1148–1154 (2016).

[19] S. Bagheri, K. Weber, T. Gissibl, T. Weiss, F. Neubrech, and H. Giessen, "Fabrication of square-centimeter plasmonic nanoantenna arrays by femtosecond direct laser writing lithography: effects of collective excitations on SEIRA enhancement," ACS Photonics **2,** 779–786 (2015).

[20] S. Bagheri *et al.*, "Large-area fabrication of TiN nanoantenna arrays for refractory plasmonics in the mid-infrared by femtosecond direct laser writing and interference lithography," Optical Materials Express **5,** 2625 (2015).

[21] S. Enoch and N. Bonod, *Plasmonics, from basics to advanced topics* (Springer Series in Optical Sciences, 2012), pp. 1–388.

[22] A. V. Zayats and S. Maier, *Active Plasmonics and Tuneable Plasmonic Metamaterials* (Wiley, 2013), pp. 1–336.

[23] J. A. Schuller, E. S. Barnard, W. Cai, Y. C. Jun, J. S. White, and M. L. Brongersma, "Plasmonics for extreme light concentration and manipulation.," Nature materials **9,** 193–204 (2010).

[24] E. Ozbay, "Plasmonics: merging photonics and electronics at nanoscale dimensions," Science **311,** 189–193 (2006).

[25] W. Cai and V. Shalaev, *Optical metamaterials fundamentals and applications* (Springer, 2009), pp. 1–200.

[26] W. Cai, U. Chettiar, A. Kildishev, and V. Shalaev, "Optical cloaking with metamaterials," Nature photonics **1,** 224 (2007).

[27] J. Li and J. B. Pendry, "Hiding under the carpet: A new strategy for cloaking," Physical Review Letters **101,** 1–4 (2008).

[28] A. V. Kildishev, W. Cai, U. K. Chettiar, and V. M. Shalaev, "Transformation optics: approaching broadband electromagnetic cloaking," New Journal of Physics **10,** 115029 (2008).

[29] D. K. Gramotnev and S. I. Bozhevolnyi, "Plasmonics beyond the diffraction limit," Nature Photonics **4,** 83–91 (2010).

[30] G. Schider, J. R. Krenn, A. Hohenau, H. Ditlbacher, A. Leitner, F. R. Aussenegg, W. L. Schaich, I. Puscasu, B. Monacelli, and G. Boreman, "Plasmon dispersion relation of Au and Ag nanowires," Physical Review B **68,** 1–4 (2003).

[31] K. S. Lee and M. A. El-Sayed, "Gold and silver nanoparticles in sensing and imaging: sensitivity of plasmon response to size, shape, and metal composition," Journal of Physical Chemistry B **110,** 19220–19225 (2006).

[32] M. Pelton, M. Liu, S. Park, N. F. Scherer, and P. Guyot-Sionnest, "Ultrafast resonant optical scattering from single gold nanorods: Large nonlinearities and plasmon saturation," Physical Review B - Condensed Matter and Materials Physics **73,** 1–6 (2006).

[33] N. I. Zheludev, "The road ahead for metamaterials," Science **328,** 582–583 (2010).

[34] C. M. Soukoulis and M. Wegener, "Past achievements and future challenges in the development of three-dimensional photonic metamaterials," Nature Photonics **5,** 523–530 (2011).

[35] D. R. Smith, "Metamaterials and negative refractive index," Science **305,** 788–792 (2004).

[36] K. L. Tsakmakidis, A. D. Boardman, and O. Hess, "'Trapped rainbow' storage of light in metamaterials.," Nature **450,** 397–401 (2007).

[37] H. F. Ma and T. J. Cui, "Three-dimensional broadband ground-plane cloak made of metamaterials.," Nature communications **1,** 21 (2010).

[38] M. Gharghi, C. Gladden, T. Zentgraf, Y. Liu, X. Yin, J. Valentine, and X. Zhang, "A carpet cloak for visible light," Nano Letters **11,** 2825–2828 (2011).

[39] A. J. Hoffman, L. Alekseyev, E. E. Narimanov, C. Gmachl, and D. L. Sivco, "Negative refraction in mid-infrared semiconductor metamaterials," Conference on Quantum Electronics and Laser Science (QELS) - Technical Digest Series 6 (2007).

[40] X. Zhang and Z. Liu, "Superlenses to overcome the diffraction limit," Nature Materials **7,** 435–441 (2008).

[41] N. Kundtz and D. R. Smith, "Extreme-angle broadband metamaterial lens," Nature Materials **9,** 129–132 (2010).

[42] W. Dickson, P. R. Evans, G. A. Wurtz, W. Hendren, R. Atkinson, R. J. Pollard, and A. V. Zayats, "Towards nonlinear plasmonic devices based on metallic nanorods," Journal of Microscopy **229,** 415–420 (2008).

[43] Y. Lu, J. Y. Rhee, W. H. Jang, Y. P. Lee, and P. Eit, "Active manipulation of plasmonic transparency based on magnetic plasmon resonance Abstract," Optics Express **18,** 1663–1667 (2010).

[44] L. Kang, Q. Zhao, H. Zhao, and J. Zhou, "Magnetically tunable negative permeability metamaterial composed by split ring resonators and ferrite rods," Optics Express **16,** 8825–8834 (2008).

[45] Y. C. Jun, E. Gonzales, J. L. Reno, E. A. Shaner, A. Gabbay, and I. Brener, "Active tuning of mid-infrared metamaterials by electrical control of carrier densities," Optics Express **20,** 1903–1911 (2012).

[46] S. H. Lee *et al.*, "Switching terahertz waves with gate-controlled active graphene metamaterials," Nature Materials **11,** 936–941 (2012).

[47] R. Atkinson, W. R. Hendren, G. A. Wurtz, W. Dickson, A. V. Zayats, P. Evans, and R. J. Pollard, "Anisotropic optical properties of arrays of gold nanorods embedded in alumina," Physical Review B **73,** 235042 (2006).

[48] A. Ono, J. I. Kato, and S. Kawata, "Subwavelength optical imaging through a metallic nanorod array," Physical Review Letters **95,** 1–4 (2005).

[49] V. A. Podolskiy, A. K. Sarychev, E. E. Narimanov, and V. M. Shalaev, "Resonant light interaction with plasmonic nanowire systems," Journal of Optics A: Pure and Applied Optics **7,** S32–S37 (2005).

[50] a. I. Rahachou and I. V. Zozoulenko, "Light propagation in nanorod arrays," Journal of Optics A: Pure and Applied Optics **9,** 265–270 (2007).

[51] A. Rahman, "Subwavelength optical imaging with an array of silver nanorods," Journal of Nanophotonics **5,** 051601 (2011).

[52] R. J. Pollard, A. Murphy, W. R. Hendren, P. R. Evans, R. Atkinson, G. A. Wurtz, A. V. Zayats, and V. A. Podolskiy,

"Optical nonlocalities and additional waves in epsilon-near-zero metamaterials," Physical Review Letters **102,** 1–4 (2009).

[53] A. N. Poddubny, P. A. Belov, P. Ginzburg, A. V. Zayats, and Y. S. Kivshar, "Microscopic model of Purcell enhancement in hyperbolic metamaterials," Physical Review B - Condensed Matter and Materials Physics **86,** 1–8 (2012).

[54] a. V. Kabashin, P. Evans, S. Pastkovsky, W. Hendren, G. a. Wurtz, R. Atkinson, R. Pollard, V. a. Podolskiy, and a. V. Zayats, "Plasmonic nanorod metamaterials for biosensing.," Nature materials **8,** 867–71 (2009).

[55] H. X. Xu, E. J. Bjerneld, M. Käll, and L. Börjesson, "Spectroscopy of single hemoglobin molecules by surface enhanced Raman scattering," Physical Review Letters **83,** 4357–4360 (1999).

[56] P. Andrew, "Energy Transfer Across a Metal Film Mediated by Surface Plasmon Polaritons," Science **306,** 1002–1005 (2004).

[57] S. Lal, S. Link, and N. J. Halas, "Nano-optics from sensing to waveguiding," Nature Photonics **1,** 641–648 (2007).

[58] M. Aeschlimann, M. Bauer, D. Bayer, T. Brixner, F. J. G. De Abajo, W. Pfeiffer, M. Rohmer, C. Spindler, and F. Steeb, "Adaptive sub-wavelength control of nanoscopic fields," Conference on Quantum Electronics and Laser Science (QELS) - Technical Digest Series **446,** 301–304 (2007).

[59] R. Hillenbrand, F. Keilmann, P. Hanarp, D. S. Sutherland, and J. Aizpurua, "Coherent imaging of nanoscale plasmon

patterns with a carbon nanotube optical probe," Applied Physics Letters **83,** 368–370 (2003).

[60] R. H. Ritchie, "Plasma Losses by Fast Electrons in Thin Films," Physical Review **106,** 874–881 (1957).

[61] F. López-Tejeira *et al.*, "Efficient unidirectional nanoslit couplers for surface plasmons," Nature Physics **3,** 324–328 (2007).

[62] P. Bharadwaj, B. Deutsch, and L. Novotny, "Optical Antennas," Adv. Opt. Photon. **1,** 438 (2009).

[63] M. Schnell, A. García-Etxarri, A. J. Huber, K. Crozier, J. Aizpurua, and R. Hillenbrand, "Controlling the near-field oscillations of loaded plasmonic nanoantennas," Nature Photonics **3,** 287–291 (2009).

[64] T. H. Taminiau, F. D. Stefani, F. B. Segerink, and N. F. van Hulst, "Optical antennas direct single-molecule emission," Nature Photonics **2,** 234–237 (2008).

[65] L. Novotny and B. Hecht, *Principles of nano-optics*, 2 ed. (Cambridge University Press, Cambridge, 2012), pp. 1–578.

[66] S. Link and M. El-Sayed, "Spectral properties and relaxation dynamics of surface plasmon electronic oscillations in gold and silver nanodots and nanorods," Journal of Physical Chemistry B **103,** 8410–8426 (1999).

[67] C. D'Andrea *et al.*, "Optical nanoantennas for multiband surface-enhanced infrared and raman spectroscopy," ACS Nano **7,** 3522–3531 (2013).

[68] K. L. Kelly, E. Coronado, L. L. Zhao, and G. C. Schatz, "The optical properties of metal nanoparticles: the influence of size, shape, and dielectric environment," The Journal of Physical Chemistry B **107,** 668–677 (2003).

[69] S. Oldenburg, R. Averitt, S. Westcott, and N. Halas, "Nanoengineering of optical resonances," Chemical Physics Letters **288,** 243–247 (1998).

[70] L. M. Liz-Marzán, "Nanometals: formation and color," Materials Today **7,** 26–31 (2004).

[71] C. J. Murphy, T. K. Sau, A. M. Gole, C. J. Orendorff, J. Gao, L. Gou, S. E. Hunyadi, and T. Li, "Anisotropic metal nanoparticles: synthesis, assembly, and optical applications," The Journal of Physical Chemistry B **109,** 13857–13870 (2005).

[72] E. M. Purcell and C. R. Pennypacker, "Scattering and absorption of light by nonspherical dielectric grains," Astrophysical Journal **186,** 705–714 (1973).

[73] E. K. Miller, "Time-domain modeling in electromagnetics," Journal of Electromagnetic Waves and Applications **8,** 1125–1172 (1994).

[74] F. J. García de Abajo and A. Howie, "Retarded field calculation of electron energy loss in inhomogeneous dielectrics," Physical Review B **65,** 115418 (2002).

[75] E. Prodan, C. Radloff, N. J. Halas, and P. Nordlander, "A hybridization model for the plasmon response of complex nanostructures.," Science **302,** 419–422 (2003).

[76] W. Rechberger, A. Hohenau, A. Leitner, J. R. Krenn, B. Lamprecht, and F. R. Aussenegg, "Optical properties of two interacting gold nanoparticles," Optics Communications **220,** 137–141 (2003).

[77] L. Silberstein, "Molecular refractivity and atomic interaction," Philosophical Magazine **33,** 521–533 (1917).

[78] T. Atay, J. H. Song, and A. V. Nurmikko, "Strongly interacting plasmon nanoparticle pairs: From dipole-dipole interaction to conductively coupled regime," Nano Letters **4,** 1627–1631 (2004).

[79] J. B. Lassiter, J. Aizpurua, L. I. Hernandez, D. W. Brandl, I. Romero, S. Lal, J. H. Hafner, P. Nordlander, and N. R. Hales, "Close encounters between two nanoshells," Nano Letters **8,** 1212–1218 (2008).

[80] K. H. Su, Q. H. Wei, X. Zhang, J. J. Mock, D. R. Smith, and S. Schultz, "Interparticle coupling effects on plasmon resonances of nanogold particles," Nano Letters **3,** 1087–1090 (2003).

[81] P. Nordlander, C. Oubre, E. Prodan, K. Li, and M. I. Stockman, "Plasmon hybridization in nanoparticle dimers," Nano Letters **4,** 899–903 (2004).

[82] D. P. Fromm, A. Sundaramurthy, P. James Schuck, G. Kino, and W. E. Moerner, "Gap-dependent optical coupling of single "bowtie" nanoantennas resonant in the visible," Nano Letters **4,** 957–961 (2004).

[83] P. J. Schuck, D. P. Fromm, A. Sundaramurthy, G. S. Kino, and W. E. Moerner, "Improving the mismatch between

light and nanoscale objects with gold bowtie nanoantennas," Physical Review Letters **94,** 14–17 (2005).

[84] C. Huck, F. Neubrech, J. Vogt, A. Toma, D. Gerbert, J. Katzmann, T. Härtling, and A. Pucci, "Surface-enhanced infrared spectroscopy using nanometer-sized gaps," ACS Nano **8,** 4908–4914 (2014).

[85] I. Romero, J. Aizpurua, G. W. Bryant, and F. J. García De Abajo, "Plasmons in nearly touching metallic nanoparticles: singular response in the limit of touching dimers.," Optics express **14,** 9988–9999 (2006).

[86] A. Alù and N. Engheta, "Tuning the scattering response of optical nanoantennas with nanocircuit loads," Nature Photonics **2,** 307–310 (2008).

[87] O. Pérez-González, N. Zabala, A. G. Borisov, N. J. Halas, P. Nordlander, and J. Aizpurua, "Optical spectroscopy of conductive junctions in plasmonic cavities," Nano Letters **10,** 3090–3095 (2010).

[88] A. Tittl, A. K. U. Michel, M. Schäferling, X. Yin, B. Gholipour, L. Cui, M. Wuttig, T. Taubner, F. Neubrech, and H. Giessen, "A switchable mid-infrared plasmonic perfect absorber with multispectral thermal imaging capability," Advanced Materials **27,** 4597–4603 (2015).

[89] A. Tittl, *Hybrid plasmonic devices for sensing and thermal imaging* (PhD Thesis, University of Stuttgart, Germany, 2015).

[90] N. Liu, M. Mesch, T. Weiss, M. Hentschel, and H. Giessen, "Infrared perfect absorber and its application as plasmonic sensor," Nano Letters **10,** 2342–2348 (2010).

[91] R. F. Aroca and D. J. Ross, "Surface-enhanced infrared spectroscopy.," Applied Spectroscopy **58,** 324–338 (2004).

[92] M. Moskovits, "Surface-enhanced spectroscopy," Reviews of Modern Physics **57,** 783–826 (1985).

[93] S. Nie and S. R. Emory, "Probing single molecules and single nanoparticles by surface enhanced raman scattering," Science ***275,*** 1102–1106 (1997).

[94] K. Kneipp, Y. Wang, H. Kneipp, L. T. Perelman, I. Itzkan, R. R. Dasari, and M. S. Feld, "Single molecule detection using surface-enhanced Raman scattering (SERS)," Physical Review Letters **78,** 1667–1670 (1997).

[95] F. Neubrech, A. Pucci, T. W. Cornelius, S. Karim, A. García-Etxarri, and J. Aizpurua, "Resonant plasmonic and vibrational coupling in a tailored nanoantenna for infrared detection," Physical Review Letters **101,** 2–5 (2008).

[96] T. R. Jensen, M. D. Malinsky, C. L. Haynes, and R. P. V. Duyne, "Nanosphere lithography : tunable localized surface plasmon resonance spectra of silver nanoparticles," Journal of Physical Chemistry B **104,** 10549–10556 (2000).

[97] M. S. Anderson, "Enhanced infrared absorption with dielectric nanoparticles," Applied Physics Letters **83,** 2964–2966 (2003).

[98] V. Giannini, A. Berrier, S. a. Maier, J. A. Sánchez-Gil, and J. G. Rivas, "Scattering efficiency and near field enhancement of active semiconductor plasmonic antennas at terahertz frequencies.," Optics express **18,** 2797–2807 (2010).

[99] M. Brehm, T. Taubner, R. Hillenbrand, and F. Keilmann, "Infrared spectroscopic mapping of single nanoparticles and viruses at nanoscale resolution," Nano Letters **6,** 1307–1310 (2006).

[100] G. V. Naik, V. M. Shalaev, and A. Boltasseva, "Alternative plasmonic materials: beyond gold and silver," Advanced Materials **25,** 3264–3294 (2013).

[101] W. a. Challener *et al.*, "Heat-assisted magnetic recording by a near-field transducer with efficient optical energy transfer," Nature Photonics **3,** 303–303 (2009).

[102] S. Fan, "Photovoltaics: an alternative 'Sun' for solar cells.," Nature nanotechnology **9,** 92–3 (2014).

[103] D. A. Boyd, L. Greengard, M. Brongersma, M. Y. El-naggar, and D. G. Goodwin, "Plasmon-assisted chemical vapor deposition," Nano letters **6,** 2592–2597 (2006).

[104] D. Kraemer *et al.*, "High-performance flat-panel solar thermoelectric generators with high thermal concentration," Nature Materials **10,** 532–538 (2011).

[105] E. Rousseau, A. Siria, G. Jourdan, S. Volz, F. Comin, J. Chevrier, and J.-J. Greffet, "Radiative heat transfer at the nanoscale," Nature Photonics **3,** 514–517 (2009).

[106] L. R. Hirsch, R. J. Stafford, J. a. Bankson, S. R. Sershen, B. Rivera, R. E. Price, J. D. Hazle, N. J. Halas, and J. L. West, "Nanoshell-mediated near-infrared thermal therapy of tumors under magnetic resonance guidance.," Proceedings of the National Academy of Sciences of the United States of America **100,** 13549–54 (2003).

[107] C. Wu, B. Neuner III, J. John, A. Milder, B. Zollars, S. Savoy, and G. Shvets, "Metamaterial-based integrated plasmonic absorber/emitter for solar thermo-photovoltaic systems," Journal of Optics **14,** 024005 (2012).

[108] A. Lenert, D. M. Bierman, Y. Nam, W. R. Chan, I. Celanović, M. Soljačić, and E. N. Wang, "A nanophotonic solar thermophotovoltaic device (Supplementary Information)," Nature Nanotechnology **9,** 126–130 (2014).

[109] V. Rinnerbauer, Y. X. Yeng, W. R. Chan, J. J. Senkevich, J. D. Joannopoulos, M. Soljačić, and I. Celanovic, "High-temperature stability and selective thermal emission of polycrystalline tantalum photonic crystals.," Optics express **21,** 11482–91 (2013).

[110] K. A. Arpin *et al.*, "Three-dimensional self-assembled photonic crystals with high temperature stability for thermal emission modification," Nature Communications **4,** 2630 (2013).

[111] U. Guler, J. C. Ndukaife, G. V. Naik, a. G. A. Nnanna, A. Kildishev, V. M. Shalaev, and A. Boltasseva, "Local heating with titanium nitride nanoparticles," CLEO: QELS-Fundamental Science (2013).

[112] J. F. Creemer, W. Van Der Vlist, C. R. De Boer, H. W. Zandbergen, P. M. Sarro, D. Briand, and N. F. De Rooij, "MEMS hotplates with TiN as a heater material," Proceedings of IEEE Sensors pp. 330–333 (2005).

[113] W. Li, U. Guler, N. Kinsey, G. V. Naik, A. Boltasseva, J. Guan, V. M. Shalaev, and A. V. Kildishev, "Refractory plasmonics with titanium nitride: broadband metamaterial absorber," Advanced Materials **26,** 7959–7965 (2014).

[114] A. N. Broers, A. C. F. Hoole Andrew C.F, and J. M. Ryan, "Electron beam lithography - resolution limits," Microelectronic Engineering **32,** 131–142 (1996).

[115] C. Vieu, F. Carcenac, A. Pepin, Y. Chen, M. Mejias, A. Lebib, L. Manin-Ferlazzo, L. Couraud, and H. Launois, "Electron beam lithography - Resolution limits and applications," Applied Surface Science **164,** 111–117 (2000).

[116] J. M. Carter, M. Farhoud, J. Ferrera, R. C. Fleming, K. Murooka, T. A. Savas, and M. Walsh, "Interference lithography," MTL Annual Report pp. 165–166 (2003).

[117] C.-H. Chang, Y. Zhao, R. K. Heilmann, and M. L. Schattenburg, "Fabrication of 50 nm period gratings with multilevel interference lithography.," Optics letters **33,** 1572–4 (2008).

[118] A. Barbara, J. Le Perchec, S. Collin, C. Sauvan, J.-L. Pelouard, T. López-Ríos, and P. Quémerais, "Generation and control of hot spots on commensurate metallic gratings.," Optics express **16,** 19127–35 (2008).

[119] A. Tittl, P. Mai, R. Taubert, T. Weiss, and H. Giessen, "Palladium-based perfect plasmonic absorber in the visible and its application to hydrogen sensing," Nano Letter **2342,** 70569 (2011).

[120] M. S. Tame, K. R. McEnery, . K. Özdemir, J. Lee, S. A. Maier, and M. S. Kim, "Quantum plasmonics," Nature Physics **9,** 329–340 (2013).

[121] S. Berweger, J. M. Atkin, R. L. Olmon, and M. B. Raschke, "Light on the tip of a needle: Plasmonic nanofocusing for

spectroscopy on the nanoscale," Journal of Physical Chemistry Letters **3,** 945–952 (2012).

[122] K. A. Willets, R. V. Duyne, and R. P. Van Duyne, "Localized surface plasmon resonance spectroscopy and sensing," Annual Review of Physical Chemistry **58,** 267–297 (2007).

[123] K. M. Mayer and J. H. Hafner, "Localized surface plasmon resonance sensors," Chemical Reviews **111,** 3828–3857 (2011).

[124] A. Vora, J. Gwamuri, N. Pala, A. Kulkarni, J. M. Pearce, and D. Ö. Güney, "Exchanging Ohmic losses in metamaterial absorbers with useful optical absorption for photovoltaics.," Scientific reports **4,** 4901 (2014).

[125] S. Pillai and M. A. Green, "Plasmonics for photovoltaic applications," Solar Energy Materials and Solar Cells **94,** 1481–1486 (2010).

[126] A. S. Roberts, A. Pors, O. Albrektsen, and S. I. Bozhevolnyi, "Subwavelength plasmonic color printing protected for ambient use," Nano Letters **14,** 783–787 (2014).

[127] F. Cheng, J. Gao, T. S. Luk, and X. Yang, "Structural color printing based on plasmonic metasurfaces of perfect light absorption.," Scientific reports **5,** 11045 (2015).

[128] K. Chen, R. Adato, and H. Altug, "Dual-band perfect absorber for multispectral plasmon-enhanced infrared spectroscopy," ACS Nano **6,** 7998–8006 (2012).

[129] Y. Li, L. Su, C. Shou, C. Yu, J. Deng, and Y. Fang, "Surface-enhanced molecular spectroscopy (SEMS) based

on perfect-absorber metamaterials in the mid-infrared.," Scientific Reports **3,** 2865 (2013).

[130] K. Aydin, V. E. Ferry, R. M. Briggs, and H. a. Atwater, "Broadband polarization-independent resonant light absorption using ultrathin plasmonic super absorbers," Nature Communications **2,** 517 (2011).

[131] P. H. Rogers, G. Sirinakis, and M. A. Carpenter, "Direct observations of electrochemical reactions within Au-YSZ thin films via absorption shifts in the Au nanoparticle surface plasmon resonance," Journal of Physical Chemistry C **112,** 6749–6757 (2008).

[132] T. Hübert, L. Boon-Brett, G. Black, and U. Banach, "Hydrogen sensors - a review," Sensors and Actuators, B: Chemical **157,** 329–352 (2011).

[133] N. Strohfeldt, A. Tittl, and H. Giessen, "Long-term stability of capped and buffered palladium-nickel thin films and nanostructures for plasmonic hydrogen sensing applications," Optical Materials Express **3,** 194 (2013).

[134] N. Strohfeldt, A. Tittl, M. Schäferling, F. Neubrech, U. Kreibig, R. Griessen, and H. Giessen, "Yttrium hydride nanoantennas for active plasmonics," Nano Letters **14,** 1140–1147 (2014).

[135] F. Sterl, N. Strohfeldt, R. Walter, R. Griessen, A. Tittl, and H. Giessen, "Magnesium as novel material for active plasmonics in the visible wavelength range," Nano Letters **15,** 7949–7955 (2015).

[136] R. Asadi, S. Bagheri, M. Khaje, M. Malekmohammad, and M. T. Tavassoly, "Tunable Fano resonance in large scale

polymer-dielectric slab photonic crystals," Microelectronic Engineering **97,** 201–203 (2012).

[137] S.-K. Meisenheimer, S. Jüchter, O. Höhn, H. Hauser, C. Wellens, V. Kübler, E. von Hauff, and B. Bläsi, "Large area plasmonic nanoparticle arrays with well-defined size and shape," Optical Materials Express **4,** 944 (2014).

[138] M. Malekmohammad, M. Soltanolkotabi, A. Erfanian, R. Asadi, S. Bagheri, M. Zahedinejad, M. Khaje, and N. M. H., "Broadband photonic crystal antireflection," Journal of the European Optical Society - Rapid publications **7,** 12008 (2012).

[139] Q. Xie, M. H. Hong, H. L. Tan, G. X. Chen, L. P. Shi, and T. C. Chong, "Fabrication of nanostructures with laser interference lithography," Journal of Alloys and Compounds **449,** 261–264 (2008).

[140] M. Khanuja, B. R. Mehta, P. Agar, P. K. Kulriya, and D. K. Avasthi, "Hydrogen induced lattice expansion and crystallinity degradation in palladium nanoparticles: Effect of hydrogen concentration, pressure, and temperature," Journal of Applied Physics 106 (2009).

[141] T. Weiss, G. Granet, N. a. Gippius, S. G. Tikhodeev, and H. Giessen, "Matched coordinates and adaptive spatial resolution in the Fourier modal method.," Optics express **17,** 8051–8061 (2009).

[142] A. Tittl, M. G. Harats, R. Walter, X. Yin, M. Schäferling, N. Liu, R. Rapaport, and H. Giessen, "Quantitative angle-resolved small-spot reflectance measurements on plasmonic perfect absorbers: Impedance matching and disorder effects," ACS Nano **8,** 10885–10892 (2014).

[143] A. B. Dahlin, J. O. Tegenfeldt, and F. Höök, "Improving the instrumental resolution of sensors based on localized surface plasmon resonance," Analytical Chemistry **78,** 4416–4423 (2006).

[144] R. Griessen, N. Strohfeldt, and H. Giessen, "Thermodynamics of the hybrid interaction of hydrogen with palladium nanoparticles," Nature Materials **15,** 1–7 (2015).

[145] A. Baldi, T. C. Narayan, A. L. Koh, and J. A. Dionne, "In situ detection of hydrogen-induced phase transitions in individual palladium nanocrystals," Nature Materials **13,** 1143–1148 (2014).

[146] R. Bardhan, L. O. Hedges, C. L. Pint, A. Javey, S. Whitelam, and J. J. Urban, "Uncovering the intrinsic size dependence of hydriding phase transformations in nanocrystals.," Nature materials **12,** 905–12 (2013).

[147] Y. Fukai, *The metal-hydrogen system, basic bulk properties* (Springer, 2006), pp. 1–498.

[148] T. B. Flanagan and W. A. Oates, "The palladium-hydrogen system," Annual review of materials science **21,** 269–304 (1991).

[149] K. Suematsu, M. Sasaki, M. Yuasa, and K. Shimanoe, "Antimony-doped tin dioxide gas sensors exhibiting high stability in the sensitivity to humidity changes," ACS Sensors **1,** 913–920 (2016).

[150] N. Strohfeldt, J. Zhao, A. Tittl, and H. Giessen, "Sensitivity engineering in direct contact palladium-gold nanosandwich hydrogen sensors," Optical Materials Express **5,** 2525 (2015).

[151] Y. Wang, K. Lee, and J. Irudayaraj, "Silver nanosphere SERS probes for sensitive identification of pathogens," Journal of Physical Chemistry C **114,** 16122–16128 (2010).

[152] R. A. Halvorson and P. J. Vikesland, "Surface-enhanced Raman spectroscopy (SERS) for environmental analyses," Environmental Science and Technology **44,** 7749–7755 (2010).

[153] P. Muhlschlegel, H.-J. Eisler, O. J. F. Martin, B. Hecht, and D. W. Pohl, "Resonant optical antennas," Science **308,** 1607–1609 (2005).

[154] R. Adato and H. Altug, "In-situ ultra-sensitive infrared absorption spectroscopy of biomolecule interactions in real time with plasmonic nanoantennas.," Nature communications **4,** 2154 (2013).

[155] R. Adato, A. a. Yanik, J. J. Amsden, D. L. Kaplan, F. G. Omenetto, M. K. Hong, S. Erramilli, and H. Altug, "Ultra-sensitive vibrational spectroscopy of protein monolayers with plasmonic nanoantenna arrays.," Proceedings of the National Academy of Sciences of the United States of America **106,** 19227–19232 (2009).

[156] E. D. Palik, *Handbook of optical constants of solids* (Academic Press, 1985), pp. 1–999.

[157] I. M. Pryce, Y. A. Kelaita, K. Aydin, and H. A. Atwater, "Compliant metamaterials for resonantly enhanced infrared absorption spectroscopy and refractive index sensing," ACS Nano **5,** 8167–8174 (2011).

[158] E. Cubukcu, S. Zhang, Y.-S. Park, G. Bartal, and X. Zhang, "Split ring resonator sensors for infrared detection of sin-

gle molecular monolayers," Applied Physics Letters **95,** 043113 (2009).

[159] H. Aouani, M. Rahmani, H. Šípová, V. Torres, K. Hegnerová, M. Beruete, J. Homola, M. Hong, M. Navarro-Cía, and S. A. Maier, "Plasmonic nanoantennas for multispectral surface-enhanced spectroscopies," Journal of Physical Chemistry C **117,** 18620–18626 (2013).

[160] T. Wang, V. H. Nguyen, A. Buchenauer, U. Schnakenberg, and T. Taubner, "Surface enhanced infrared spectroscopy with gold strip gratings," Optics Express **21,** 9005–9010 (2013).

[161] W. Mao, I. Wathuthanthri, and C.-H. Choi, "Tunable two-mirror interference lithography system for wafer-scale nanopatterning.," Optics letters **36,** 3176–3178 (2011).

[162] R. Ji, W. Lee, R. Scholz, U. Gösele, and K. Nielsch, "Templated fabrication of nanowire and nanoring arrays based on interference lithography and electrochemical deposition," Advanced Materials **18,** 2593–2596 (2006).

[163] Y. S. Do, J. H. Park, B. Y. Hwang, S. M. Lee, B. K. Ju, and K. C. Choi, "Plasmonic color filter and its fabrication for large-area applications," Advanced Optical Materials **1,** 109–109 (2013).

[164] Y. Shen *et al.*, "Plasmonic gold mushroom arrays with refractive index sensing figures of merit approaching the theoretical limit.," Nature communications **4,** 2381 (2013).

[165] A. A. Yanik, A. E. Cetin, M. Huang, A. Artar, S. H. Mousavi, A. Khanikaev, J. Connor, G. Shvets, and H. Altug, "Ultrasensitive plasmonic fano sensor enables seeing

protein monolayers with naked eye," IEEE Photonic Society 24th Annual Meeting, PHO **108,** 425–426 (2011).

[166] D. Xia, Z. Ku, S. C. Lee, and S. R. J. Brueck, "Nanostructures and functional materials fabricated by interferometric lithography," Advanced Materials **23,** 147–179 (2011).

[167] H. C. Guo, D. Nau, A. Radke, Z. P. Zhang, J. Stodolka, X. L. Yang, S. Thikodeev, N. A. Gippius, and H. Giessen, "Large-area metallic photonic crystal fabrication with interference lithography and dry etching," Applied Physics B: Lasers and Optics **81,** 271–275 (2005).

[168] H. Matsui, W. Badalawa, A. Ikehata, and H. Tabata, "Oxide surface plasmon resonance for a new sensing platform in the near-infrared range," Advanced Optical Materials **1,** 397–403 (2013).

[169] N. Verellen, F. López-Tejeira, R. Paniagua-Domínguez, D. Vercruysse, D. Denkova, L. Lagae, P. Van Dorpe, V. V. Moshchalkov, and J. A. Sánchez-Gil, "Mode parity-controlled Fano- and Lorentz-like line shapes arising in plasmonic nanorods," Nano Letters **14,** 2322–2329 (2014).

[170] A. O. Pinchuk, "Angle dependent collective surface plasmon resonance in an array of silver nanoparticles," Journal of Physical Chemistry A **113,** 4430–4436 (2009).

[171] J. Aizpurua, G. W. Bryant, L. J. Richter, F. J. García De Abajo, B. K. Kelley, and T. Mallouk, "Optical properties of coupled metallic nanorods for field-enhanced spectroscopy," Physical Review B **71,** 235420 (2005).

[172] L. Novotny, "Effective wavelength scaling for optical antennas," Physical Review Letters **98,** 1–4 (2007).

[173] R. Schreiber, "Structure and growth of self-assembled monolayers," Progress in Surface Science **65,** 151–256 (2000).

[174] P. H. C. Eilers, "A perfect smoother," Analytical Chemistry **75,** 3631–3636 (2003).

[175] M. Abb, Y. Wang, N. Papasimakis, C. H. de Groot, and O. L. Muskens, "Surface-enhanced infrared spectroscopy using metal oxide plasmonic antenna arrays.," Nano Letters **14,** 346–352 (2013).

[176] V. Giannini, Y. Francescato, H. Amrania, C. C. Phillips, and S. A. Maier, "Fano resonances in nanoscale plasmonic systems: A parameter-free modeling approach," Nano Letters **11,** 2835–2840 (2011).

[177] E. J. Osley, C. G. Biris, P. G. Thompson, R. R. F. Jahromi, P. A. Warburton, and N. C. Panoiu, "Fano resonance resulting from a tunable interaction between molecular vibrational modes and a double continuum of a plasmonic metamolecule," Physical Review Letters **110,** 1–5 (2013).

[178] D. Dregely, F. Neubrech, H. Duan, R. Vogelgesang, and H. Giessen, "Vibrational near-field mapping of planar and buried three-dimensional plasmonic nanostructures.," Nature communications **4,** 2237 (2013).

[179] L. V. Brown, K. Zhao, N. King, H. Sobhani, P. Nordlander, and N. J. Halas, "Surface-enhanced infrared absorption using individual cross antennas tailored to chemical moieties.," Journal of the American Chemical Society **135,** 3688–3695 (2013).

[180] D. Weber, P. Albella, P. Alonso-González, F. Neubrech, H. Gui, T. Nagao, R. Hillenbrand, J. Aizpurua, and A. Pucci, "Longitudinal and transverse coupling in infrared gold nanoantenna arrays: long range versus short range interaction regimes.," Optics express **19,** 15047–61 (2011).

[181] F. Neubrech, S. Beck, T. Glaser, and M. Hentschel, "Spatial extent of plasmonic enhancement of vibrational signals in the infrared," ACS Nano pp. 6250–6258 (2014).

[182] B. C. Smith, *Fundamentals of Fourier Transform Infrared Spectroscopy, Second Edition* (CRC Press, 2011).

[183] A. Yang, M. D. Huntington, M. F. Cardinal, S. S. Masango, R. P. Van Duyne, and T. W. Odom, "Hetero-oligomer nanoparticle arrays for plasmon-enhanced hydrogen sensing.," ACS nano **8,** 7639–47 (2014).

[184] G. Kenanakis, A. Xomalis, A. Selimis, M. Vamvakaki, M. Farsari, M. Kafesaki, C. M. Soukoulis, and E. N. Economou, "Three-dimensional infrared metamaterial with asymmetric transmission," ACS Photonics **2,** 287–294 (2015).

[185] Y. Cui, Y. Phang, R. S. Hegde, Y. H. Lee, and X. Y. Ling, "Plasmonic silver nanowire structures for two-dimensional multiple-digit molecular data storage application," ACS Photonics 2014 **1,** 631–637 (2014).

[186] X. Xiong, S. C. Jiang, Y. H. Hu, R. W. Peng, and M. Wang, "Structured metal film as a perfect absorber," Advanced Materials **25,** 3994–4000 (2013).

[187] M. Deubel, G. v. Freymann, M. Wegener, S. Pereira, K. Busch, and C. M. Soukoulis, "Direct laser writing of three-

dimensional photonic-crystal templates for telecommunications," Nature Materials **3,** 444–447 (2004).

[188] M. Thiel, M. S. Rill, G. v. Freymann, and M. Wegener, "Three-dimensional bi-chiral photonic crystals," Advanced Material ***21,*** 4680–4682 (2009).

[189] M. Schumann, T. Bückmann, N. Gruhler, M. Wegener, and W. Pernice, "Hybrid 2D–3D optical devices for integrated optics by direct laser writing," Light: Science & Applications **3,** e175 (2014).

[190] A. Radke, T. Gissibl, T. Klotzb??cher, P. V. Braun, and H. Giessen, "Three-dimensional bichiral plasmonic crystals fabricated by direct laser writing and electroless silver plating," Advanced Materials **23,** 3018–3021 (2011).

[191] J. Theiss, P. Pavaskar, P. M. Echternach, R. E. Muller, and S. B. Cronin, "Plasmonic nanoparticle arrays with nanometer separation for high-performance SERS substrates," Nano Letters **10,** 2749–2754 (2010).

[192] X. Cui, K. Tawa, H. Hori, and J. Nishii, "Tailored plasmonic gratings for enhanced fluorescence detection and microscopic imaging," Advanced Functional Materials **20,** 546–553 (2010).

[193] Z. Li, S. Butun, and K. Aydin, "Touching gold nanoparticle chain based plasmonic antenna arrays and optical metamaterials," ACS Photonics **1,** 228–234 (2014).

[194] E. M. Hicks, S. Zou, G. C. Schatz, K. G. Spears, R. P. Van Duyne, L. Gunnarsson, T. Rindzevicius, B. Kasemo, and M. Käll, "Controlling plasmon line shapes through diffractive coupling in linear arrays of cylindrical nanoparticles

fabricated by electron beam lithography," Nano Letters **5,** 1065–1070 (2005).

[195] Z. Pirzadeh, T. Pakizeh, V. Miljkovic, C. Langhammer, and A. Dmitriev, "Plasmon-interband coupling in nickel nanoantennas," ACS Photonics **1,** 158–162 (2014).

[196] G. Kichin, T. Weiss, H. Gao, J. Henzie, T. W. Odom, S. G. Tikhodeev, and H. Giessen, "Metal-dielectric photonic crystal superlattice: 1D and 2D models and empty lattice approximation," Physica B: Condensed Matter **407,** 4037–4042 (2012).

[197] T. Bueckmann, N. Stenger, M. Kadic, J. Kaschke, A. Fr??lich, T. Kennerknecht, C. Eberl, M. Thiel, and M. Wegener, "Tailored 3D mechanical metamaterials made by dip-in direct-laser-writing optical lithography," Advanced Materials **24,** 2710–2714 (2012).

[198] V. Giannini, G. Vecchi, and J. G??mez Rivas, "Lighting up multipolar surface plasmon polaritons by collective resonances in arrays of nanoantennas," Physical Review Letters **105,** 1–4 (2010).

[199] P. Lovera, D. Jones, B. Corbett, and A. O'Riordan, "Polarization tunable transmission through plasmonic arrays of elliptical nanopores," Optics Express **20,** 25325 (2012).

[200] P. Alonso-González *et al.*, "Resolving the electromagnetic mechanism of surface-enhanced light scattering at single hot spots.," Nature Communications **3,** 684 (2012).

[201] R. Adato, A. A. Yanik, C.-H. Wu, G. Shvets, and H. Altug, "Radiative engineering of plasmon lifetimes in em-

bedded nanoantenna arrays.," Optics Express **18,** 4526–4537 (2010).

[202] P. Alonso-González *et al.*, "Experimental verification of the spectral shift between near- and far-field peak intensities of plasmonic infrared nanoantennas," Physical Review Letters **110,** 1–6 (2013).

[203] F. Neubrech, T. Kolb, R. Lovrincic, G. Fahsold, A. Pucci, J. Aizpurua, T. W. Cornelius, M. E. Toimil-Molares, R. Neumann, and S. Karim, "Resonances of individual metal nanowires in the infrared," Applied Physics Letters **89,** 2004–2007 (2006).

[204] N. Li, A. Tittl, S. Yue, H. Giessen, C. Song, B. Ding, and N. Liu, "DNA-assembled bimetallic plasmonic nanosensors," Light: Science & Applications **3,** e226 (2014).

[205] G. Dolling, M. Wegener, C. M. Soukoulis, and S. Linden, "Negative-index metamaterial at 780 nm wavelength.," Optics Letters **32,** 53–55 (2007).

[206] N. Liu, L. Langguth, T. Weiss, J. Kästel, M. Fleischhauer, T. Pfau, and H. Giessen, "Plasmonic analogue of electromagnetically induced transparency at the Drude damping limit," Nature Materials **8,** 758–762 (2009).

[207] C. Wu, A. B. Khanikaev, R. Adato, N. Arju, A. A. Yanik, H. Altug, and G. Shvets, "Fano-resonant asymmetric metamaterials for ultrasensitive spectroscopy and identification of molecular monolayers," Nature Materials **11,** 69–75 (2011).

[208] D. Lin, P. Fan, E. Hasman, and M. L. Brongersma, "Dielectric gradient metasurface optical elements," Science **345,** 298–302 (2014).

[209] G. V. Naik, J. Kim, and A. Boltasseva, "Oxides and nitrides as alternative plasmonic materials in the optical range [Invited]," Optical Materials Express **1,** 1090–1099 (2011).

[210] K. Appavoo, D. Y. Lei, Y. Sonnefraud, B. Wang, S. T. Pantelides, S. a. Maier, and R. F. Haglund, "Role of defects in the phase transition of VO2 nanoparticles probed by plasmon resonance spectroscopy.," Nano letters **12,** 780–6 (2012).

[211] B. Gholipour, J. Zhang, K. F. MacDonald, D. W. Hewak, and N. I. Zheludev, "An all-optical, non-volatile, bidirectional, phase-change meta-switch," Advanced Materials **25,** 3050–3054 (2013).

[212] U. Guler, a. Boltasseva, and V. M. Shalaev, "Refractory plasmonics," Science **344,** 263–264 (2014).

[213] M. Diem, T. Koschny, and C. M. Soukoulis, "Wide-angle perfect absorber/thermal emitter in the terahertz regime," Physical Review B **79,** 1–4 (2009).

[214] L. Gui, S. Bagheri, N. Strohfeldt, M. Hentschel, C. M. Zgrabik, B. Metzger, H. Linnenbank, E. L. Hu, and H. Giessen, "Nonlinear refractory plasmonics with titanium nitride nanoantennas," Nano Letters **16,** 5708–5713 (2016).

[215] C. Maus, T. Stauden, G. Ecke, K. Tonisch, and J. Pezoldt, "Smooth ceramic titanium nitride contacts on AlGaN/GaN-heterostructures," Semiconductor Science and Technology **27,** 115007 (2012).

[216] U. Guler, A. V. Kildishev, A. Boltasseva, and V. M. Shalaev, "Plasmonics on the slope of enlightenment: the role

of transition metal nitrides," Faraday Discussions **78,** 1–16 (2015).

[217] M. Malekmohammad, "Combining micro- and nano-texture to fabricate an antireflective layer," Journal of Micro/Nanolithography, MEMS, and MOEMS **11,** 013011 (2012).

[218] M. Malekmohammad, M. Soltanolkotabi, R. Asadi, M. H. Naderi, A. Erfanian, M. Zahedinejad, S. Bagheri, and M. Khaje, "Hybrid structure for efficiency enhancement of photodetectors," Applied Surface Science **264,** 1–6 (2013).

[219] M. Malekmohammad, R. Asadi, M. Zahedinejad, M. Khaje, S. Bagheri, A. Erfaniyan, M. Soltanolkotabi, M. H. Naderi, and F. Raissi, "Efficiency enhancement of PtSi detectors by photonic crystals," IEEE Sensors Journal **14,** 4055–4058 (2014).

[220] G. V. Naik, B. Saha, J. Liu, S. M. Saber, E. A. Stach, J. M. K. Irudayaraj, T. D. Sands, V. M. Shalaev, and A. Boltasseva, "Epitaxial superlattices with titanium nitride as a plasmonic component for optical hyperbolic metamaterials.," Proceedings of the National Academy of Sciences of the United States of America **111,** 7546–7551 (2014).

[221] G. V. Naik, J. L. Schroeder, X. Ni, A. V. Kildishev, T. D. Sands, and A. Boltasseva, "Oxides and nitrides as alternative plasmonic materials in the optical range [Invited]," Optical Materials Express **2,** 478–489 (2012).

[222] S. Tripura Sundari, R. Ramaseshan, F. Jose, S. Dash, and a. K. Tyagi, "Investigation of temperature dependent dielectric constant of a sputtered TiN thin film by spec-

troscopic ellipsometry," Journal of Applied Physics **115,** 033516 (2014).

ACKNOWLEDGMENTS

Writing a PhD dissertation in physics would have been impossible without the help of many people. I would like to express my special appreciation to all the people who contributed to the success of this work, scientifically or otherwise.
I would like to thank:

- Prof. Dr. Harald Giessen for hosting me in his great institute and for providing a fascinating research topic, which excited me over all the years of this thesis.
- Prof Dr. Hans Peter Büchler and Prof. Clemens Bechinger for taking the time to be on my examination committee.
- Prof. Dr. Nader Engheta and Prof. Dr. Evelyn L. Hu for kindly let me to visit their labs and gave a talk in their high level groups.
- Dr. Christine von Rekowski for all administrative affairs.
- Prof. Dr. Evelyn L. Hu, Dr. Gunther Richter and Dr. Thomas Stauden for the great collaboration on refractory plasmonics project.
- Prof. Dr. Heinz Schweizer, Dr. Richard Taubert and Dr. Liwei Fu for introducing me the nanofabrication instruments in the cleanroom.
- Dr. Andreas Tittl and Dr. Mario Hentschel for stimulating discussions.

- Dr. Andreas Tittl, Nikolai Strohfeldt and Florian Sterl for great teamwork and also sharing their knowledges on H_2 sensing.
- Dominik Floss for his great photography of my samples and setups.
- Dr. Christine M. Zgrabik for her great collaboration on refractory plasmonics project and preparation of high-quality titanium nitride films.
- Dr. Martin Schäferling and Nikolai Strohfeldt for being great officemates.
- Dr. Timo Gissibl for the great collaboration on direct laser writing project.
- Dr. Martin Mesch and Dr. Martin Schaferling for all kind supports regarding technical computer matters.
- Nikolai Strohfeldt and Florian Sterl for their support on Blender visualization.
- Dr. Frank Neubrech for discussions about surface enhanced infrared spectroscopy.
- Dr. Xinghui Yin and Dr. Bettina Frank for their kind support and help during the dissertation writing process.
- Dr. Lili Gui for great teamwork on nonlinear properties of titanium nitride.
- Ksenia Weber for the great collaboration in direct laser writing project.
- Monika Ubl, Ramon Walter and Michael Kube for all technical stuff in the cleanroom.

- Dr. Stefano De Zuani and Dr. Audrey Berrier for the measurement of ellipsometric data.
- Ralf Kamella for being very helpful in all kind of mechanical construction issues.
- Finally the entire 4^{th} Physics Institute for a great working atmosphere.
- Finally, my heart-felt thanks go to my beloved wife Sepideh and also my parents. Words cannot express how grateful I am to them which were always my support in the moments when there was no one to answer my queries.

CURRICULUM VITAE

Personal data

Name:	Shahin Bagheri
Date of birth:	21.03.1981
Place of birth:	Shiraz, Iran
Citizenship:	Iranian
Address:	Walther-knoll Str. 3, 71083 Herrenberg.
Mail:	bbshahin@gmail.com

2000 - 2005: BSc. in Physics, Major in Solid State Physics, University of Razi, Kermanshah, Iran.

2005 - 2008: MSc. in Photonics, Laser and Plasma Research Institute, Shahid Beheshti University, Tehran, Iran.

2007 - 2008: Thesis: Fabrication and Characterization of OLED Devices with ITO/PVK:PBD:C_6/Al Structure and Investigation on the Effect of Adding PEDOT:PSS as a Charge Injecting Layer.
Supervisor: Prof. Dr. Ezeddin Mohajerani.

2012 - 2017: PhD student in Physics, 4^{th} Physics Institute, University of Stuttgart, Germany.
Thesis: Large-Area Plasmonics and Sensors.
Supervisor: Prof. Dr. Harald Giessen.